3D modelling of ship resistance in restricted waterways and application to an inland eco-driving prototype

Florian Linde

Par **Florian LINDE**

3D modelling of ship resistance in restricted waterways and application to an inland eco-driving prototype

Thèse présentée
pour l'obtention du grade
de Docteur de l'UTC

Soutenue le 19 octobre 2017
Spécialité : Mécanique Avancée : Unité de recherche en Mécanique - Laboratoire Roberval (UMR-7337)
D2389

3D modelling of ship resistance in restricted waterways and application to an inland eco-driving prototype

Modélisation 3D de la résistance à l'avancement en milieu confiné et application à un éco-pilote fluvial

Florian Linde

Spécialité : Mécanique Avancée

Thèse soutenue le 19/10/2017 devant le jury composé de :

Rapporteurs:

Jacques-André ASTOLFI	*Michel VISONNEAU*
Maître de conférences	Directeur de Recherche
Ecole Navale de Brest	Ecole Centrale de Nantes

Examinateurs:

Damien CALLUAUD	*Katrien ELOOT*	*Adnan IBRAHIMBEGOVIĆ*
Maître de Conférence	Professeur des Universités	Professeur des Universités
Univ. de Poitiers	Univ. de Gand	Univ. de Technologie de Compiègne

Directeurs de Thèse:

Abdellatif OUAHSINE	*Philippe SERGENT*
Professeur des Universités	Directeur de Recherche
Univ. de Technologie de Compiègne	CEREMA

Co-encadrant de Thèse:

Nicolas HUYBRECTHS
Chargé de Recherche
CEREMA

Université de Technologie de Compiègne

Laboratoire Roberval UMR CNRS 7337

Abstract

An eco-driving prototype, named EcoNav, is developed with the aim of optimizing a vessel speed in order to reduce fuel consumption for a given itinerary. EcoNav is organized in several modules:

- a 2D hydraulic model simulating the flow conditions (current speed and water depth) along the itinerary;
- a ship resistance model calculating the thrust necessary to counteract the hydrodynamic forces;
- a fuel consumption model calculating the fuel consumption corresponding to the thrust input;
- a non linear optimization algorithm calculating the optimal speed profile.

In order to evaluate the fuel consumption of an inland vessel, a ship resistance numerical model is developed in the first part of this PhD. This 3D numerical model simulates the flow around an inland self-propelled vessel and evaluates the hydrodynamic forces acting on the hull. A RANS solver is coupled with a quasi-Newton approach to find the equilibrium position and calculate ship sinkage. This method is validated by comparing the results of numerical simulations to towing tank tests. The numerical results with and without sinkage are also compared to study the influence of sinkage on ship resistance and on the accuracy of the method. Additionally, some empirical models are investigated and compared with the accuracy of the numerical method. Finally, the numerical model is used to determine if channel width and water depth restriction contribute to the same amount of ship resistance increase for the same level of restriction. The results of that investigation give insight to whether channel restriction can be characterized by a unique parameter (for instance the blockage ratio) or two parameters to distinguish water depth and channel width effects.

In the second part of this PhD, the numerical methods used in the speed optimization model are described and validated. The speed optimization model is then used to simulate a real case: the itinerary of the self-propelled ship Oural on river Seine, between Chatou and Poses (153 km). The optimized fuel consumption is compared with the non-optimized fuel consumption, based on AIS speed profile retrieved on this itinerary. The effects of the ship trajectory and travel duration on fuel consumption are also investigated. The results of those investigations showed that optimizing the ship speed lead to an average fuel saving of 8 % and that using an optimal track and including real time information such as lock availability and river traffic can lead to additional fuel savings.

Résumé

Les travaux de cette thèse ont pour but de développer un prototype d'éco-pilote, nommé EcoNav, permettant d'optimiser la vitesse d'un bateau afin de réduire sa consommation de carburant. EcoNav est composé de plusieurs modules dont:

- un modèle hydraulique 2D simulant l'écoulement hydrodynamique (vitesse du courant et hauteur deau) le long du trajet du bateau;
- un modèle de résistance à l'avancement servant à alimenter un modèle de prédiction de la consommation de carburant;
- un algorithme d'optimisation permettant de trouver le profil optimal de vitesse.

Afin de pouvoir estimer la consommation de carburant, un modèle numérique de la résistance à l'avancement en milieu confiné a été développé durant la première partie de cette thèse. Ce modèle numérique 3D simule l'écoulement du fluide autour du bateau et permet de calculer les forces agissant sur sa coque. La résolution des équations RANS est couplée avec un algorithme de quasi-Newton afin de trouver la position d'équilibre du bateau et calculer son enfoncement. Cette méthode est validée en comparant les résultats numériques avec des résultats expérimentaux issus d'essais en bassin de traction. L'influence de l'enfoncement sur la résistance à l'avancement et la précision de la méthode est étudiée en comparant les résultats numériques obtenus avec et sans enfoncement. La précision des modèles empiriques de prédiction de la résistance à l'avancement est également comparée à celle du modèle numérique. Enfin, le modèle numérique est utilisé afin de déterminer si le confinement en largeur ou en profondeur ont une influence identique sur l'augmentation de résistance à l'avancement. Les résultats de cette étude permettent d'établir si le confinement de la voie d'eau peut être caractérisé à l'aide d'un paramètre unique (coefficient de blocage par exemple) ou bien deux paramètres permettant de distinguer le confinement latéral et vertical.

Dans la seconde partie de cette thèse, les méthodes numériques utilisées pour le modèle d'éco-pilote sont décrites et comparées afin de sélectionner celles qui sont le plus adaptées à chaque module. EcoNav est ensuite utilisé afin de modéliser un cas réel: celui du bateau automoteur Oural navigant sur la Seine entre Chatou et Poses (153 km). La consommation optimisée est comparée à la consommation non optimisée, calculée à partir des vitesses AIS observées sur le tronçon étudié. L'influence de la trajectoire du bateau et de son temps de parcours sur sa consommation sont également étudiés. Les résultats de ces investigations ont montré qu'optimiser la vitesse du bateau permet d'obtenir une réduction de la consommation de carburant de l'ordre de 8 % et qu'optimiser la trajectoire du bateau ainsi que prendre en compte des informations en temps réel (disponibilité des écluses, trafic sur le fleuve) peuvent permettre de réaliser des économies de carburant supplémentaires.

Acknowledgements

I would like to express my deepest gratitude to my PhD supervisors Prof. Abdellatif Ouahsine, Dr. Philippe Sergent and Dr. Nicolas Huybrechts for their guidance and continued support of my doctoral research. Thank you for your careful attention, professional skills and challenging remarks.

I am very grateful to my laboratory members for their precious help and guidance, especially Delphine Brancherie, Pierre Feissel, Emmanuel Lefrançois and Catherine KNOPF-LENOIR-VAYSSADE.

My sincere thanks go to my colleagues at LHN research group, namely Shang-Gui Cai, Peng Du, Shengcheng Ji, Sami Kaidi and Hassan Smaoui.

I would like to thank Smaïl HIDOUCHE and Marc-Henri GUITTENY for their contribution with the ship consumption model, Voie Navigable de France for the access to their bathymetric data base and Compagnie Fluvial de Transport & VNF for granting us access to AIS data for the Bosphore. Many thanks also go to André Hage, Mathieu Lapy, Mathieu Vandescuren and Adrian Constantinescu (ANAST, University of Liege, Belgium) for their contribution with the experimental campaign and their continuous support. Appreciation also goes to Damien Calluaud and Clément Caplier for the nice collaboration we had in GIS HED^2 project.

I would like to express my many thanks towards many fellow doctoral or post-doctoral students that I met at UTC and with whom we shared more than just work related discussion especially Benjamin, Chiarra, Eduard, Ivan, Pablo and Tea. Special thanks go to Shang-Gui, my fellow PhD student, with whom I shared many late

night discussions and happy moments throughout this PhD. PhD would not have been the same without them.

I would also like to thank my colleagues at Cerema for their welcome and kindness, especially Alain, Christophe, Damien, Fatiha, Guillaume, Jean-Matthieu, Julien, Laurent and Milena.

My gratitude goes to all my friend who have always been supportive and encouraging, especially Alexandre, Clément, Eric, Etienne, Fred, Laurent and Pierre-Adrien. I'm sorry we didn't get to meet as often as I would have liked to, but I hope we can catch up!

Finally and most importantly, my deepest gratitude goes to my family, Maria and my always smiling son Lukas for their support, encouragement, patience and their understanding during this period and even more.

à ma famille, Maria et Lukas

Table of Contents

List of Figures

List of Tables

Nomenclature

List of symbols

A_C	Wetter canal cross sectional area	$[m^2]$
A_S	Wetted midship sectional area	$[m^2]$
B	Ship breadth	$[m]$
Cb	Ship block coefficient	$[-]$
C_F	Coefficient of frictionnal resistance	$[-]$
C_R	Coefficient of residuary resistance	$[-]$
C_T	Coefficient of total resistance	$[-]$
C_V	Coefficient of viscous resistance	$[-]$
C_W	Coefficient of wave resistance	$[-]$
FCR	Fuel consumption reduction	$[-]$
FC_T	Total fuel consumption	$[L]$
Fn	Froude number	$[-]$
Fnh	Depth Froude number	$[-]$
F_Z	Vertical forces	$[N]$
G	Ship centre of gravity	
g	Gravitational acceleration	$[m.s^{-2}]$
H	Water depth	$[m]$
H/T	Water depth restriction coefficient	$[-]$
M_Gy	Trim moment	$[Nm]$
P_B	Engine break power	$[kW]$
P_D	Power delivered to propeller	$[kW]$
P_E	Effective power	$[kW]$
P_T	Thrust power	$[kW]$

Q	Flow discharge	$[m^3/s]$
Re	Reynolds number	$[-]$
C_F	Frictionnal resistance	$[N]$
R_R	Residuary resistance	$[N]$
R_T	Total ship resistance	$[N]$
R_V	Viscous resistance	$[N]$
R_W	Wave resistance	$[N]$
SFC	Specific fuel consumption	$[g/kW/h]$
T_{max}	Maximum travel duration	$[h]$
$\boldsymbol{u}$	Fluid velocity vector	$[m/s]$
V	Ship speed	$[m/s]$
V_L	Schijf limiting speed (subcritical speed)	$[m/s]$
W/B	Canal width restriction coefficient	$[-]$
$(1+k)$	Form factor	$[-]$
ΔZ	Ship sinkage	$[mm]$
η_B	Propeller efficiency	$[-]$
η_G	Global propulsion efficiency	$[-]$
η_H	Hull efficiency	$[-]$
η_S	Shaft efficiency	$[-]$
λ	Wave length	$[m]$
μ	Dynamic viscosity	$[kg/(s.m)]$
ν	Kinematic viscosity	$[m^2/s]$
ρ	Fluid density	$[kg/m^3]$
θ	Trim angle	$[^\circ]$
y^+	Non dimensional wall distance	$[-]$

List of abbreviations

CFD	Computional fluid dynamic
DOF	Degree of freedom
ETA	Expected time arrival
FDM	Feasible direction method
GPM	Gaussian projection method
IWT	Inland waterway transport
MLS	Moving Least Square
MSE	Mean square error
PM	Penalty method
PR	Polynomial regression
RANS	Reynolds averaged Navier-Stokes
RBF	Radial basis function
RSM	Response surface method
SLSQP	Sequential least square quadratic programming
SVR	Support vector regression
TEU	Ton equivalent unit
VOF	Volume of fluid

Introduction

This chapter introduces the subject of this PhD. The context of this work is first described, then a brief overview of the topics covered in this PhD is presented followed by a literature survey on the two main research fields explored. Finally the objectives of this PhD and its content are summarized.

Context

Inland waterway transport (IWT) is an alternative mode of goods transport also complementary to road and railway transport. It offers many advantages compared to those two other modes of transport:

- safety record : the accident probability for this mode of transport is very low and when they happen, their cost in economic and human term is significantly reduced compared to the other means of goods transport;
- environmental cost : many studies have shown that IWT is the most environmentally friendly mode of transport (Rohács and Simongati, 2007; Federal German Water and Shipping Administration, 2007; Agence de l'Environnement et de la Maitrise de l'Energie, 2006);
- time reliability : there is little or no congestion on inland waterways and therefore delay in goods delivery is reduced compared to other modes of transport;
- carrying capacity : a pushed barge with a load of 2 000 tons carries the equivalent of 50 railway cars at 40 tons each or 80 trucks at 25 tons each and therefore the carrying capacity per transport unit is very high.

The beginning of the construction of Seine-Nord Europe Canal in 2017 whose completion is expected by 2023-24 is an encouraging signal of France dedication to

promote this mode of transport. This canal will replace the existing Canal du Nord of limited capacity (barges of 250 to 650 tonnes) to form a major high capacity transport corridor for barges and push-tows up to 4400 tonnes, from Le Havre to Dunkirk, Benelux and the Rhine. This project will considerably expand inland trade flows while connecting to northern European countries such as Belgium, Germany and the Netherlands. This project is also expected to significantly boost French inland waterway transport sector.

However, to ensure inland transport development, significant research efforts must be made in order to improve inland vessel fuel efficiency. Indeed, inland navigation faces many challenges such as over-aging fleet, increasing fuel prices, climate change, and stronger environmental regulations regarding air emissions. Moreover, the French waterway system is the longest in European Union with approximately 8800 km of navigable rivers and canals. However, a 2011 report from French National Assembly (Assemblée Nationale, 2011) pointed out that French inland waterway transport sector is lagging behind its European neighbours. For instance, IWT share in France represents only 6% of all goods transport against 12% for Germany, 16% for Belgium and 33% for the Netherlands. Moreover, French inland fleet is smaller and older than the fleet of those three countries. Making inland waterway transport more efficient and more sustainable is also one of the goals promoted by the European Commission through the NAIADES II package "Towards quality inland waterway transport".

Improving inland waterway transport efficiency requires a better understanding of physical phenomenon occurring in restricted waterways and technical solutions to improve inland waterway transport fuel efficiency.

Ship resistance

When a ship moves through water and air, it experiences a force opposing the motion. This force is the water's resistance to the motion and is referred as "Total hull resistance" or "Total resistance" (R_T). Ship resistance is also defined as the force required to tow a ship at a constant speed in calm water. This resistance depends on many parameters such as ship speed, hull form, water temperature, water depth and breadth, wind,... A good knowledge of ship resistance is of foremost impor-

tance for naval architects in order to estimate the ship propulsive power and thus design the ship adequately. The relation between ship resistance and the power necessary to overcome this resistance is given by:

$$P_E = R_T V \tag{0.1}$$

where P_E is the effective power, R_T the total ship resistance and V the ship's speed.

Decomposition of ship resistance

Two features of a ship moving through the water are (see Figure 0.1):

- the generated wave system;
- the region of turbulent flow.

These two phenomenons are generated by dissipation of energy from the hull and participate to ship resistance. This resistance is applied on the hull through pressure distribution and shear force.

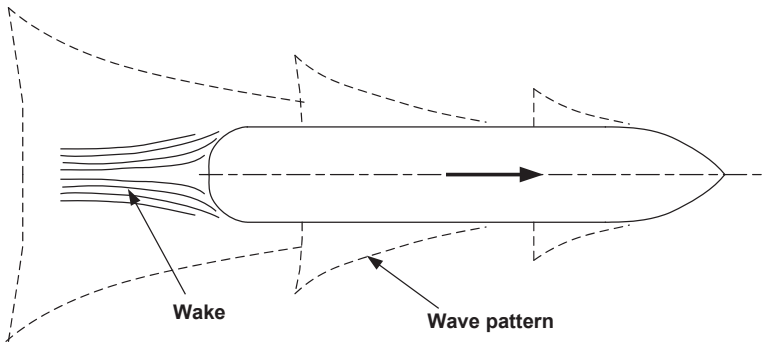

Figure 0.1.: *Ship generated waves and wake.*
Source: *Molland et al. (2011)*

Looking either at the forces applying on the ship's hull and opposing its motion or the way energy applied to move the ship is dissipated entails two ways of breaking down ship resistance.

The forces acting on the ship's hull can be divided into:

- Frictional Resistance: it is the sum of the tangential shear forces τ acting on each element of the hull surface. This resistance is generated because of the water viscosity.
- Pressure resistance: it is the sum of the pressure forces P acting on each

element of the hull surface. This resistance is partly due to viscous effects, but also to hull wavemaking.

The energy dissipated by the ship's hull is decomposed into:

- Total viscous resistance: it is the resistance associated with the energy dissipated by the vortices, the vorticity and turbulence in the turbulent flow. This resistance include the skin frictional resistance and a part of the pressure resistance force as the flow in the turbulent zone is impacted by the pressure distribution and skin friction.
- Total wave resistance: it is the resistance associated with the energy required to sustain the wave pattern created by the hull.

Figure 0.2 summarises these two possible breakdown of the total ship resistance.

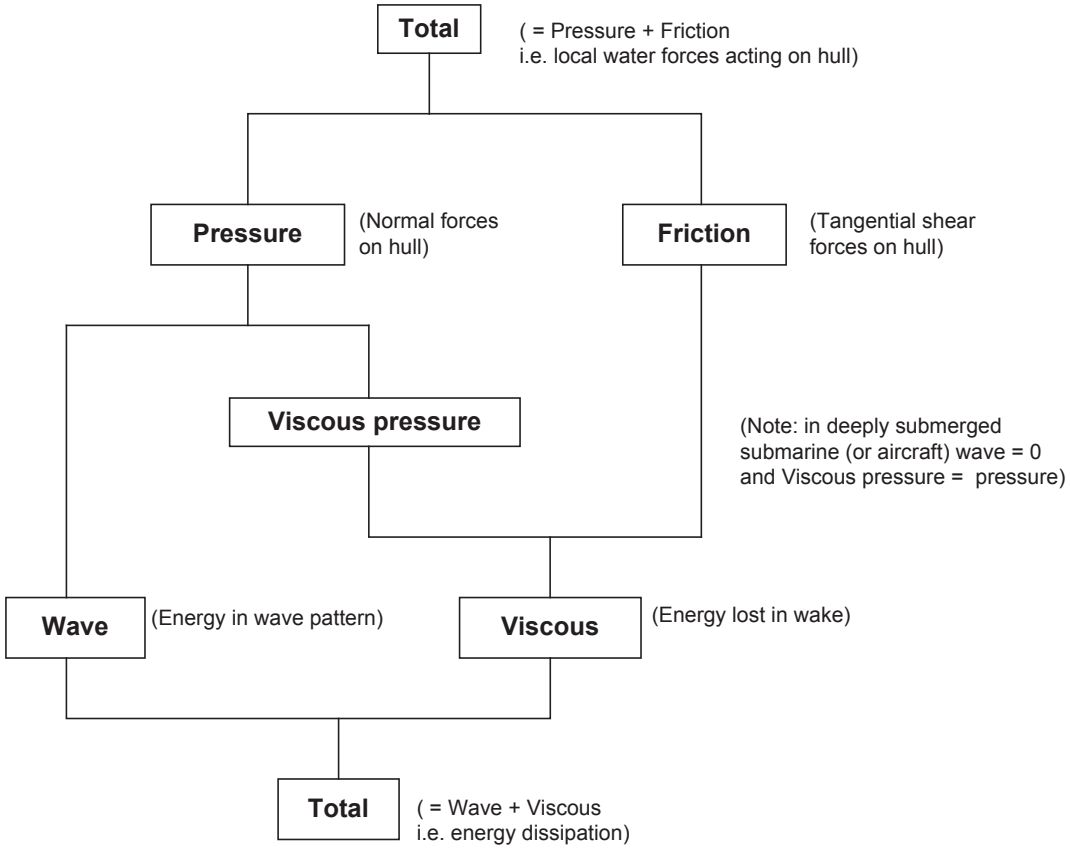

Figure 0.2.: *Basic resistance components.*
Source: *Molland et al. (2011)*

Figure 0.3 shows the total resistance of four different ships with the percentage

of each component entering in the resistance decomposition.

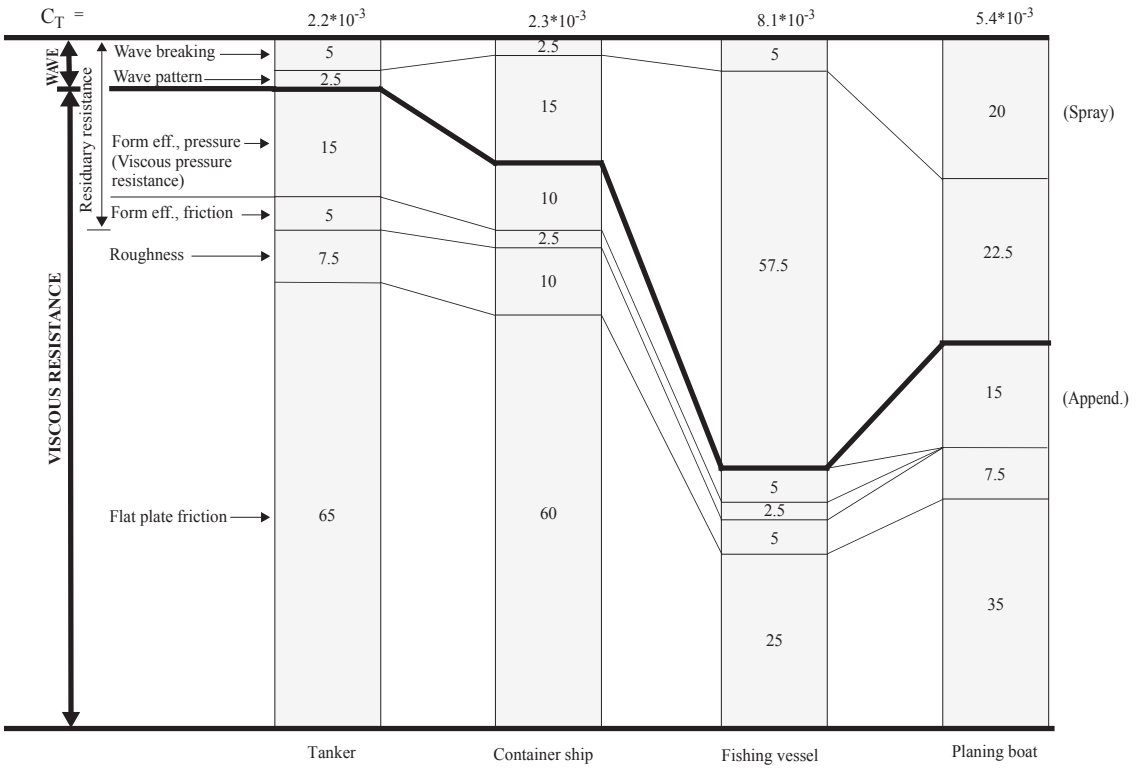

Figure 0.3.: *Resistance components for four vessels.*
Source: *Larsson and Raven (2010)*

Figure 0.3 shows how resistance components can vary depending on the type of vessel. For slowest ships (tanker and container ship), the wave resistance is very small and the viscous resistance is predominant. On the opposite, at high speeds (fishing vessel and planing boat), the wave resistance becomes more important. This is due to the fact that at higher speeds, the wave pattern is stronger and has an increased effect on the hull.

Other resistance components

Under certain conditions, factors generally neglected in the total hull resistance can become considerable.

Appendage resistance

The main appendages consist into rudders, stabilisers, bossings, shaft brackets, bilge keels and water inlet scoops. Table 0.1 shows some typical values of appendage resistance as a percentage of hull naked resistance in calm-water.

Table 0.1.: *Resistance of appendages as a percentage of hull naked resistance, data taken from Molland et al. (2011)*

Item	% of naked resistance
Bilge keels	23
Rudder	up to about 5 (e.g. about 2 for a cargo vessel)
Stabiliser fins	3
Shafting, brackets or bossings	67
Condenser scoops	1

Air resistance

When a ship moves, it experience air resistance on the part of the hull above water and its superstructure. The magnitude of this resistance will depend on the size and shape of the hull and its superstructure and on the ship speed. Generally, the air resistance is very small compared to the total hull resistance. Typical values of air resistance for various ship types are given in Table 0.2.

Table 0.2.: *Typical values of air resistance as a percentage of calm-water hull resistance, data taken from Molland et al. (2011)*

Type	**LBP** (m)	**Dw** (tonnes)	**Service speed** (knots)	**Fr**	**Air drag** (%)
Tanker	330	250,000	15	0.136	2.0
Tanker	174	41,000	14.5	0.181	3.0
Bulk carrier	290	170,000	15	0.145	2.5
Bulk carrier	180	45,000	14	0.171	3.0
Container	334	100,000 10,000 TEU	26	0.234	4.5
Container	232	37,000 3500 TEU	23.5	0.253	4.0
Catamaran ferry	80	650 pass 150 cars	36	0.661	4.0
Passenger ship	265	2000 pass	22	0.222	6.0

Weather impact on ship resistance

Under bad weather conditions, the total hull resistance can increase severely. Indeed, wind blowing on the hull creates addition resistance and also raises waves which can cause a further increase in resistance.

Roughness and fouling

The roughness of the ship's hull can increase the frictional resistance. Usually, the effect of roughness on frictional resistance appears for increased speeds, as shown in Figure 0.4.

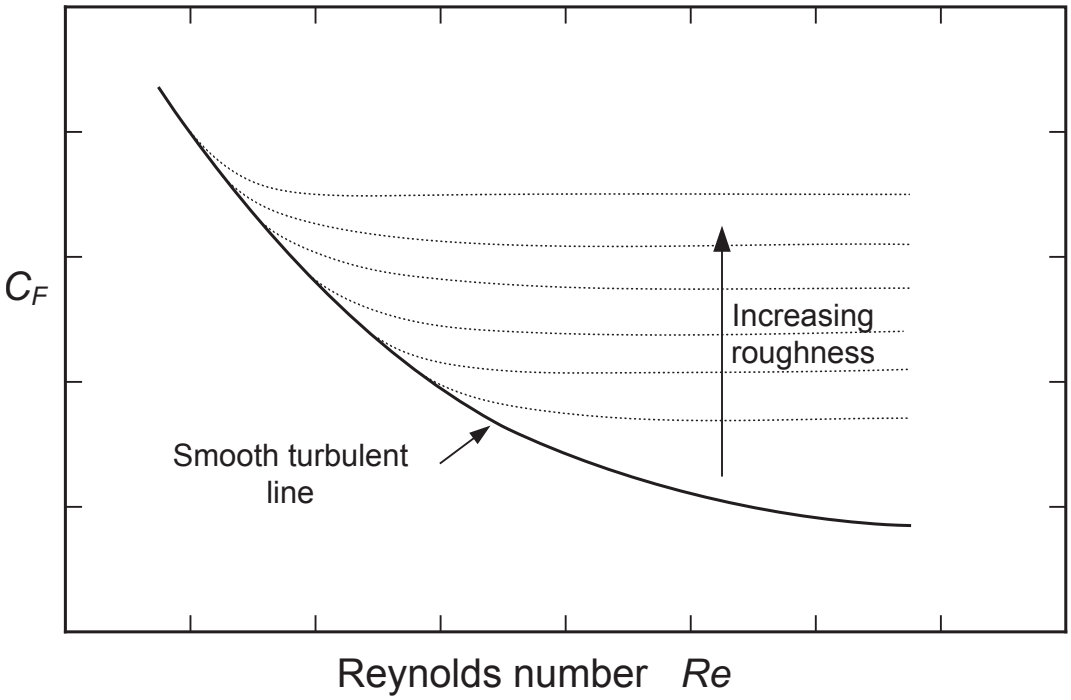

Figure 0.4.: *Effect of roughness on skin friction.*
Source: *Molland et al. (2011)*

Additional resistance increase can be caused by fouling, such as the growth of weeds or barnacles which increase the "roughness" of the hull. It has been reported that increase in roughness (fouling included) can represent an increase of 10-30% of the total resistance each year Molland et al. (2011).

Important parameters

Similarity parameters

The Froude and Reynolds number are two dimensionless numbers characterizing the behaviour of fluid flow. These two parameters are also very important for dynamic similarity in model testing.

The Froude number is a dimensionless number characterising the ratio between the inertial effects and gravity effects. It is defined by the following equation:

$$Fr = \frac{V}{\sqrt{gL}} \tag{0.2}$$

where V is the ship's speed and L the ship's length.

Sometimes, when water depth is small, it is useful to discuss speed ranges in term of depth Froude number Fr_h, defined by the following relation:

$$Fr_h = \frac{V}{\sqrt{gh}} \tag{0.3}$$

where h is the water depth.

The Reynolds number is a dimensionless number defined by the ratio of inertial forces to viscous forces which therefore quantify the relative importance of these two types of forces for given flow conditions. It is given by the following equation:

$$Re = \frac{LV}{\nu} \tag{0.4}$$

where ν is the kinematic viscosity ($\nu = \frac{\mu}{\rho}$) i.e the ratio between the dynamic viscosity ρ and the fluid density ρ.

Resistance coefficients

Usually, ship resistance is quantified through the use of dimensionless coefficients which are:

- the coefficient of total resistance C_T

$$C_T = \frac{R_T}{1/2\rho S V^2} \tag{0.5}$$

  where S is the wetted surface area of the ship's hull.

- the coefficient of frictional resistance C_F

$$C_F = \frac{R_F}{1/2\rho S V^2} \tag{0.6}$$

- the coefficient of wave resistance C_W

$$C_W = \frac{R_W}{1/2\rho S V^2} \tag{0.7}$$

- the coefficient of viscous resistance C_V

$$C_V = \frac{R_V}{1/2\rho S V^2} \tag{0.8}$$

- the coefficient of residuary resistance C_R

$$C_R = \frac{R_R}{1/2\rho S V^2} \tag{0.9}$$

Knowing the breakdown of the total ship resistance mentioned in ?? , the resistance coefficients are linked by the following equations:

$$C_T = C_F + C_R = C_W + C_V \tag{0.10}$$

Ship resistance in confined waters

Hydrodynamic effects of confined waters

Confined waters (restricted waters) are characterised by limited water depth and breadth. When a ship enters confined waters, changes in the hydrodynamic happen. The main phenomenons associated with these changes in the flow are surge waves, return flow, squat, draw-down, sediment re-suspension and bank scouring.

When a ship moves in restricted waterways, the pressure distribution is modified: the water in front of its bow is pushed creating an increase in pressure and a decrease of pressure behind the stern. As a result, water flows from all direction to fill the void. Moreover, water behind the keel is sucked by the propeller and rejected in a direction opposite to the ship movement. Due to the reduction of the section where the water can flow, the flow around the ship is also accelerated, causing an increase in kinetic energy and a decrease in potential energy. This decrease in potential energy and pressure causes a lowering of the water level named **drawdown**. The increase in the water speed under the ship causes a decrease in pressure and as result, a vertical force is applied on the ship and the ship drops vertically down in the water. The uneven pressure distribution along the ship's hull creates a moment along the transverse axis which lead the ship to trim by the bow or the stern. This combination of **vertical sinkage** and **trim** is called ship **squat**. In some cases, when the keel clearance is very small, the ship might even strike the bottom of the chan-

nel. The accelerated flow around the ship's hull is called **return flow** or **backflow**. The speed of this return flow depends on several factors among which the channel geometry, the ship speed and the blockage factor. Figure 0.5 illustrates ship squat and return flow in a restricted waterway.

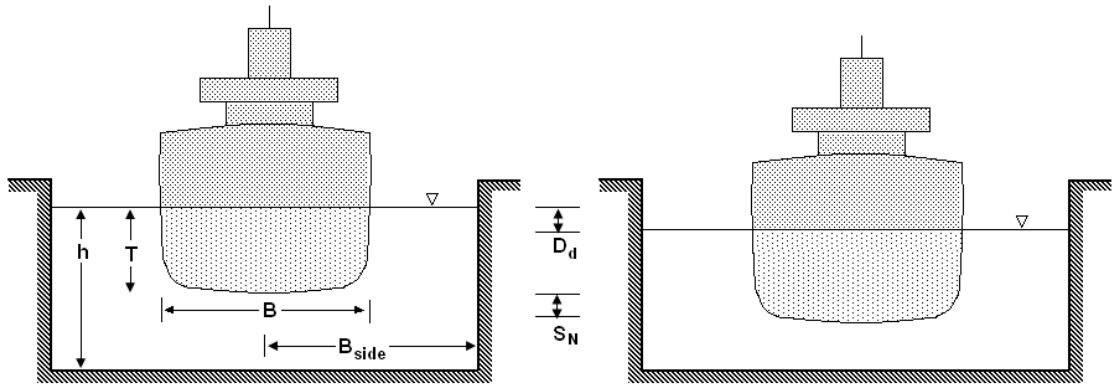

(a) *Drawdown and squat for moving vessel*

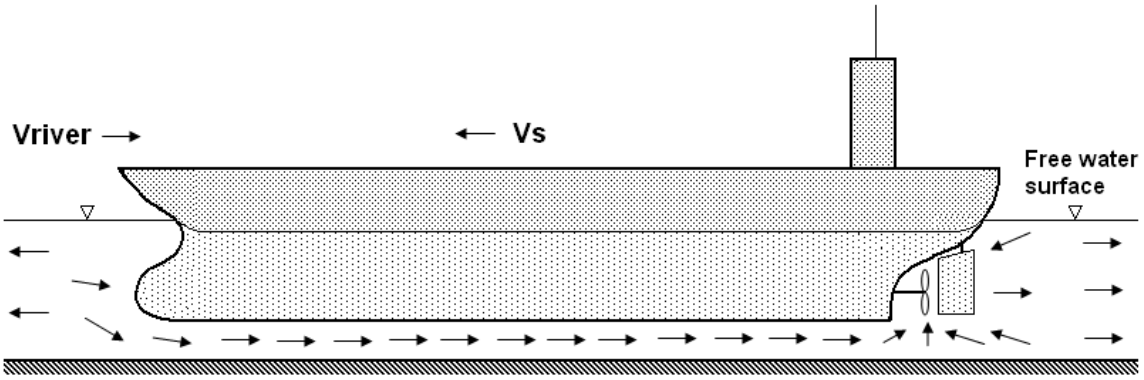

(b) *Flow past under keel*

Figure 0.5.: *Schematic diagram of ship squat and return flow in restricted waterways*
Source: *Das et al. (2012)*

Effect on resistance

The previously described hydrodynamic phenomenons have consequences on ship resistance:

- the increased speed of the flow around the hull creates an increase of the viscous resistance on the hull,
- as the ship is squatting, there is an increase in the ship wetted surface area,

increasing the frictional resistance,

- in shallow water, waves tend to be to be larger than waves produced in deep water at the same speed.

Characterization of channel restriction

To estimate the nature and level of restriction of the waterway, the following parameters are commonly used: water depth to draft ratio H/T, canal width to ship breadth (B) ratio W/B and canal section (A_C) to midship section (A_S) ratio A_C/A_S (blockage ratio). Figure 0.6 shows a schematic representation of the waterway geometric parameters.

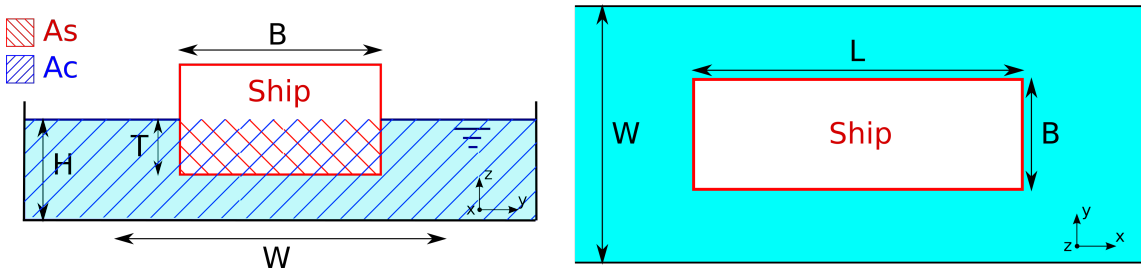

Figure 0.6.: *Schematic representation of the waterway geometric parameters*

The ITTC87 report (ITTC, 1987) states that there is an influence of the bottom or the banks when $H/T < 4$ or $W/B < 4$; and that a general restriction of the waterway starts when $A_C/A_S < 15$. Moreover, when the Froude depth number $F_{nh} = V/\sqrt{(gH)}$ is greater than 0.7, there is an influence of the bottom on wave shape and resistance. Usually inland vessels do not navigate at speeds corresponding to Froude depth number values above 0.7.

Flow regime in restricted waterways

When sailing in confined waters, a dship may move in one of three speed range: subcritical, critical and super-critical. Those speed range are delimited by the lower critical speed (or subcritical speed) and upper critical speed (or super-critical speed):

- In subcritical speed range, the flow is steady and the vessel moves forward by displacing water from the bow to the stern. As described previously, the conversion of pressure into kinetic energy causes the ship to squat.

- At velocities greater than the lower critical speed, the ship enters the critical speed range where the flow becomes unsteady. Some of the displaced water is unable to flow toward the stern and dams up forward of the bow. An hydraulic jump is observed behind the ship due to quick change in flow velocity.
- If the ship moves with further speed, it will go above the upper critical speed and reach the super-critical range where the flow is steady again. In the super-critical range, the ship "sails" on the bow wave and therefore a decrease in ship resistance is observed.

Figure 0.7 shows a schematic representation of typical resistance curves in open water (green), shallow water (blue) and confined water (red).

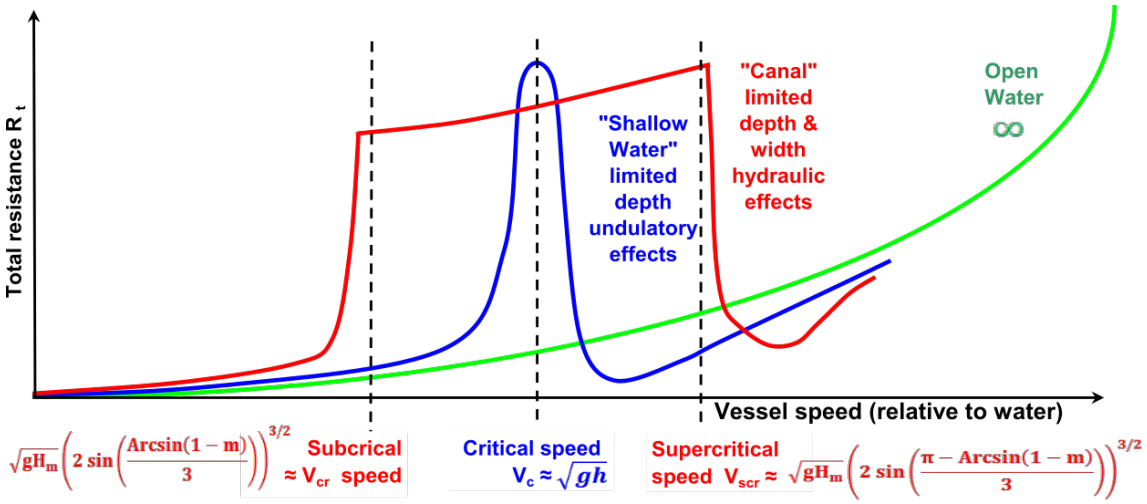

Figure 0.7.: *Schematic representation of typical resistance curves in open water (green), shallow water (blue) and confined water (red).*
Source: *Pompée (2015)*

As illustrated in Figure 0.7, in shallow water (no lateral restriction), only the water depth and its effect on the ship generated waves affects the ship's behaviour and the curve of resistance shows a peak around the critical speed. In restricted waters, the ship's behaviour is influenced by the effect of the bottom and the banks, which causes the hydraulic effect described above, and the curve of resistance shows a "M" shape around the two critical velocities. It is worth mentioning that inland vessels used for waterway transport sail at subcritical range (below the lower critical speed) as their engine power is not sufficient to overcome the resistance barrier.

Prediction of ship resistance in restricted waterways

Several authors (Schofield, 1974; Constantine, 1960; Schijf, 1949; Kreitner, 1934) studied the hydrodynamic aspects of inland navigation. Those studies showed the existence of a limiting speed that a self-propelled vessel sailing in restricted waterways cannot exceed, caused by a steep ship resistance rise. This limiting speed is called Schijf limiting speed and corresponds to the lower critical speed occurring between subcritical and critical regimes, which is named subcritical speed. Jansen and Schijf (1953) and later McNown (1976) showed that the added resistance in canal appeared to be proportional to ship sinkage. Empirical models based on towing tank results (Schlichting, 1934; Geerts et al., 2010; Karpov, 1946; Artjuskov, 1968; Landweber, 1939) have been developed to predict ship resistance in restricted waterways. Pompée (2015) reviewed many empirical models available for shallow and confined water resistance prediction. These models often apply open water resistance formula (Holtrop, 1984) with corrected speed. However, the validity of some of these models has been questioned (Raven, 2012) because of their weak empirical and theoretical basis. Most of these methods are derived from experimental results obtained with sea-going ships whose characteristics strongly differ from inland vessels. Hence, the parameters used for those formulas and the experimental results used for the regression are not always relevant in the case of inland ships (Rotteveel et al., 2014). Another drawback of these methods is that inland ships often fall out of their range of application. Attempts to predict ship resistance through the use of mathematical models based on theoretical approach have also been made (Jovanović, 2004). However, these methods often lack validation and make strong hypothesis to simplify the problem. Empirical models for the prediction of ship squat (combination of ship sinkage and trim) in canals also exist. Briggs et al. (2009) reviewed the squat empirical formulas recommended by the World Association for Waterborne Transport Infrastructure (PIANC).

Ship resistance and squat in shallow and confined waters have also been studied with numerical methods. Ship squat numerical studies are often based on boundary element method (Härting et al., 2009), Tuck's theory (Gourlay, 2008), computational fluid dynamics (CFD) with potential flow theory (Debaillon, 2010) and mathematical models (Lataire et al., 2012). Tezdogan et al. (2015) conducted a literature survey of the numerical methods used to predict squat and indicated that most use linear theory and slender-body assumption for calculating the flow around

the ship, which might not apply for ships with higher block coefficient, such as inland vessels. Moreover, potential flow-based methods cannot be used to calculate the total ship resistance because they solve non-viscous fluid equations. Over the past few years, with the increase in computing power and development of new numerical methods, there has been a growing interest in CFD techniques applied to ship hydrodynamic. Stern et al. (2013) reviewed the progress made over the last ten years in CFD applied to ship hydrodynamics. The Gothenburg 2010 Workshop on Numerical Hydrodynamics (Larsson et al., 2013) gathered the results of 33 groups on 18 cases and concluded that the mean error for all computed open water resistance cases was practically zero. Few numerical studies of ship resistance in shallow water and even less in restricted waters have been conducted. Senthil Prakash and Chandra (2013) used the commercial CFD software Fluent to study the shallow water resistance of a river ship. They compared their numerical results at subcritical speed with Schlichting empirical method and concluded that a fairly good agreement was achieved. However, it is not specified in their paper if ship squat was taken into account in their calculations and no comparison with experimental data was performed. Raven (2012) also studied shallow water effects on ship resistance with the Reynolds-averaged Navier-Stokes (RANS) solver PARNASSOS and compared his results with empirical models. He reported that the methods of Schlichting and Lackenby performed poorly for the investigated cases. In that study, the effect of ship squat on resistance results were not taken into account. Tezdogan et al. (2015) performed squat and resistance calculations in restricted waters with commercial CFD software STAR-CCM+ and compared their results with the squat empirical data from the PreSquat workshop (Mucha et al., 2014). That workshop used the Duisburg Test Case (Moctar et al., 2012), a 14 000 TEU (twenty-foot equivalent unit) container carrier whose geometry is typical of a post-panamax container ship (sea vessel), for their model ship. That workshop concluded that there is a need for further validation of numerical predictions in shallow and restricted waters. Tezdogan et al. (2015) reported that their squat results are underpredicted within 10 % of the experimental data and that ship resistance was very sensitive to ship sinkage. However, no experimental data was available to validate their ship resistance results. In general, ship resistance and ship sinkage are studied separately. On one hand, numerical models predicting ship sinkage solve non-viscous fluid equations (Euler) and thus cannot evaluate ship resistance. On the other hand, numerical ship resistance models do not simulate ship sinkage, and,

therefore, do not include its effect on ship resistance in their calculations. Moreover, the model ships used in most of the numerical studies mentioned are sea vessels whose characteristics strongly differ from those of an inland vessel.

Solutions for inland ship fuel consumption reduction

The average age of inland ships in Europe is above 40 years and a significant proportion of the current fleet is over-aged. Replacing the older ships with new units will take decades and therefore improving the economic and environmental performance of existing ships (retrofitting) is also necessary.

Overview of existing fuel consumption reduction techniques

The European FP7 project MoVe IT! (MoVe IT! FP7 European project, 2012) and the Danube Carpathian Programme (Radojčić, 2009) reviewed the existing solutions for improving the economic and environmental performance of existing or new inland vessels. These solutions can mainly be categorized into four main groups:

- improvement in hull resistance;
- improvement in propulsion and transmission efficiency;
- improvement in propulsion plant;
- improvement of ship utilisation (navigation).

Those four categories are outlined in Figure 0.8 with solution examples.

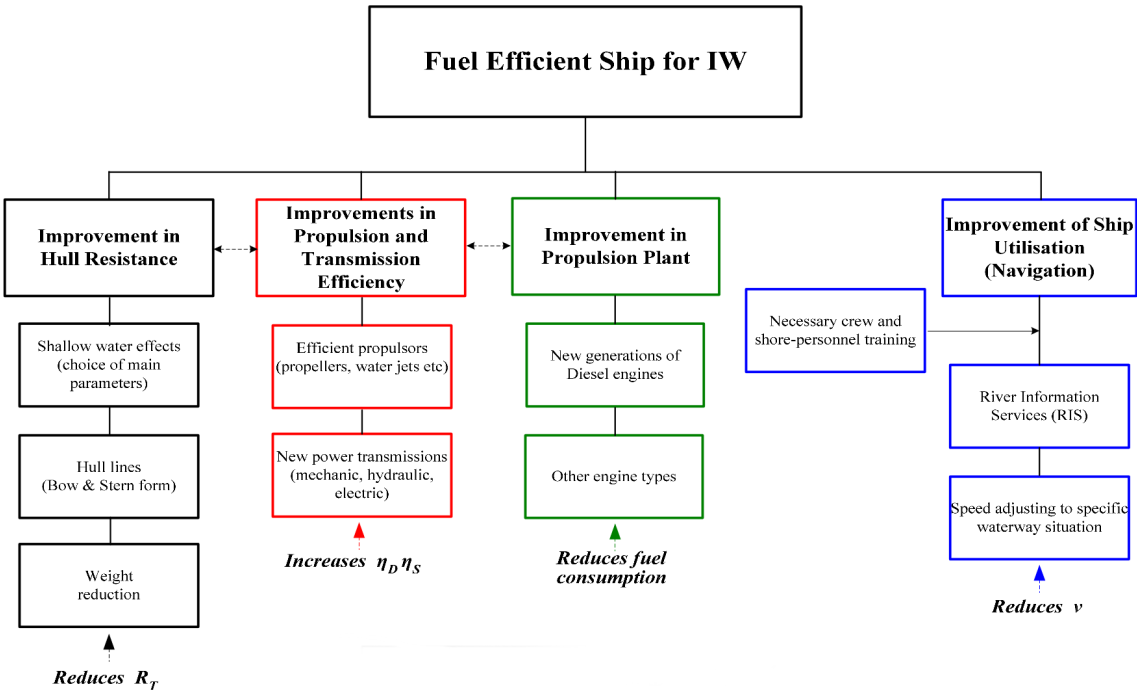

Figure 0.8.: *Main categories of retrofitting solutions*
Source: *Radojčić (2009)*

Improvement in hull resistance

Decreasing hull resistance allows to reduce the forces opposing the movement of the ship and therefore leads to fuel consumption savings. Hull resistance can be decreased by adapting the hull shape to minimize resistance in shallow water. Hull shape optimization has mainly be focused on the design of efficient bow and stern regions (Rotteveel et al., 2014) which mostly contribute to wave and viscous pressure resistance. Zoelner (2003) showed that contemporary ships with improved designs have up to 50 % lower resistance than inland ships from a few decades ago.

Another way to reduce hull resistance is to make the ship hull lighter. The materials used for inland ship construction is almost exclusively steel because of its durability. However, the use of lightweight materials and structural arrangements (such as reinforced composites materials or sandwich structure) for shipbuilding (Noury et al., 2002) could lead to significant fuel consumption reduction. For instance, Jastrzebski et al. (2003) reported a structural weight saving of 40 % if steel sandwich

panels would be used for the construction of a small barge of 32.5 m.

Solutions intending to decrease the frictional resistance of the hull have also been studied. For instance, the frictional drag can be reduced by using air as a lubricant with techniques such as injecting air bubbles in the boundary layer, using air films along the bottom plating or air cavities in the ship's bottom (Foeth, 2008). It is also possible to reduce the ship resistance by applying special coatings with anti-fouling properties allowing to reduce water friction (Stenzel et al., 2011).

Improvement in propulsion and transmission efficiency

Many existing inland ships are built with conventional propellers whose efficiency often reach 70 % in maritime navigation but can be as low as 20-40 % when used in restricted waterways (Georgakaki and Sorenson, 2004). Replacing those conventional propellers with one more suited to inland navigation could lead to significant fuel consumption reduction. For example, Geerts et al. (2010) reported that the three blade propeller of the Campine-Barge 'Prima' was replaced with a five-blade propeller which led to a speed gain of 1 km/h for the same fuel consumption. Many examples of innovative propellers more suited to inland navigation exist (MoVe IT! FP7 European project, 2012):

- ducted propeller with a non-rotating nozzle which deliver greater thrust;
- adjustable tunnel preventing the income of air at low draft;
- pre swirl stator redirecting the flow before it enters the propeller disc;
- skew or contra-rotating propellers.

Improvement in propulsion plant

Currently, diesel engines are the most common types of engines used for inland ships. However, those engines are often marinized general application diesel engines or truck engines. However, those engines are usually much older than those used for road transport and belong to previous technological generation (inland ship engine have a lifetime of 20 years against 5 years for truck engines). Therefore, inland ships emit non negligible quantities of carbon dioxide (CO2), sulphur-oxides (Sox), nitrogen-oxides (NOx) and particulate matter (PM). With increased environmental legislation on transport emissions, inland shipping will need to reduce its

greenhouse gas emissions and can benefit from the use of alternative fuels or improved diesel engines. Possible solutions for improvement in propulsions plants include (MoVe IT! FP7 European project, 2012):

- diesel electric propulsion where diesel powered generators provide electrical power used to propel the ship;
- hybrid propulsion using more than one power source to propel the ship (diesel generator with batteries for instance);
- natural gas engines using liquefied natural gas (LNG) instead of ordinary fuel;
- multi (truck) diesel electric using several truck diesel engines as generators in a diesel electric propulsion;
- fuel cell converting the chemical energy of a fuel (hydrogen or natural gas for instance) into direct current power.

Improvement of ship utilisation (navigation)

Improvement in ship operations, aiming to reduce and/or adjust the ship speed during a travel can also lead to fuel consumption reduction. For instance, a traffic control system indicating the availability of locks and quays to ship operators could help them adjust their speed during the travel in order to minimize fuel consumption while ensuring to respect their ETA. River information services (RIS) offering possibilities for voyage planning, tracking and tracing through rapid electronic data transfer (in real-time) can contribute to a safe and efficient transport process and lead to a reduction of fuel consumption. Replacing the smaller fleet units or increasing the ship main dimensions can help to lower the emissions per tonnekm. Prediction of the water depth on the ship route can help to adjust the ship speed in the shallow water zones. Applying slow steaming, which consist in sailing at a reduced speed, can also lead to consumption reduction.

Slow steaming and speed optimization

A ship sailing at a reduced speed will emit less greenhouse gas and consume less fuel. This practice, also known as slow steaming, is already used in many maritime commercial ship sectors such as tankers, bulk carriers and containerships, but rarely applied for inland navigation. A basic application of slow steaming consists

in sailing at a speed lower than the vessel's design speed. More evolved slow steaming practices involve speed optimization algorithm taking account of several factors (weather forecast, current, trim, draft and water depth) (Psaraftis and Kontovas, 2014). Some industrial products such as Eniram speed[1] already exist and are frequently used for maritime navigation. However, to the knowledge of the author, no such products exist or are used for inland navigation. A prototype version of the EconomyPlanner is currently developed and tested within the framework of the FP7 Eu project MoVeIT! (Bons et al., 2014). The aim of the EconomyPlanner is to generate a real time local water depth map through cooperative depth measurements and determine the optimal track and vessel speed respecting ETA (expected time of arrival) conditions for a given itinerary in order to reduce fuel consumption. The optimization of the fuel consumption is carried out by a module named Virtual Ship and developed by MARIN (Maritime Research Institute Netherlands). The power and resistance calculations are based on formulas derived from regression analysis on model experiments carried out at MARIN and sea trials. Corrections of shallow water effect are made based on Schlichting (1934) and Landweber (1939) methods.

PhD objectives

The main objective of this PhD is to develop an economy planner model with the aim of optimizing a vessel speed and reduce fuel consumption for a given itinerary. In order to fulfil this goal, it is necessary to be able to evaluate the fuel consumption of a ship sailing in a channel which in turn requires to predict ship resistance in restricted waters. Therefore, two main tasks have been undertaken during this PhD: the development of a ship resistance model and the economy planner model. Throughout the rest of this manuscript, the economy planner model will be referred to as EcoNav or speed optimization model. The numerical investigations carried in this PhD were focused on one type of inland vessel: a 135 m long self-propelled vessel. Self-propelled vessel is predominant for goods transport on European waterways. In 2014, more than half of European Union inland transport of goods were carried by such ships (Eurostat, 2015).

During the first part of this PhD, a 3D numerical model has been developed to simu-

[1] www.eniram.fi/product/eniram-speed

late the flow around an inland self-propelled vessel and evaluate the hydrodynamic forces acting on the hull. A RANS solver is coupled with a quasi-Newton approach to find the equilibrium position and calculate ship sinkage. This method is validated by comparing the results of numerical simulations to towing tank tests. The numerical results with and without sinkage are also compared to study the influence of sinkage on ship resistance and on the accuracy of the method. Additionally, some empirical models are investigated and compared with the accuracy of the numerical method. Finally, the numerical model is used to determine if channel width and water depth restriction contribute to the same amount of ship resistance increase for the same level of restriction. The results of that investigation give insight to whether channel restriction can be characterized by a unique parameter (for instance the blockage ratio) or two parameters to distinguish water depth and channel width effects.

The second part of the PhD has been dedicated to the development of EcoNav. EcoNav combines a 2D hydraulic model, a ship resistance model (developped in the first part of this PhD), a fuel consumption model and a nonlinear optimization algorithm to find optimal speed profile. The economy planner is used to simulate a real case: the itinerary of the self-propelled ship Oural on river Seine, between Chatou and Poses (153 km). The optimized fuel consumption is compared with the non-optimized fuel consumption, based on AIS speed profile retrieved on this itinerary. The effects of the ship trajectory and travel duration on fuel consumption are also investigated.

PhD outline

This thesis is organized as follows:

- Chapter 2 describes the ship resistance numerical model developed in this PhD. First the fluid solver is presented by detailing the hydrodynamic equations, the turbulence and free surface models, the boundary conditions used and the numerical solver parameters. Then the method used to model ship squat is explained and the coupling between the 3D hydrodynamic model and the ship movement model is described.
- Chapter 3 focuses on the validation of the ship resistance model. In this

chapter, the towing tank tests carried at ANAST are first introduced, then the mesh generation process used for the numerical model is described and finally, the results from the numerical investigations carried out with this model are presented and discussed.

- Chapter 4 deals with the validation of the hydrodynamic flow simulated with the ship resistance model at super-critical regime. This chapter gives a description of the experiments carried out in Pprime institute towing tank and presents the project results. The comparison between experimental and numerical results allows to evaluate the ability of the numerical model to reproduce the flow and waves generated by a ship navigating in shallow water for speeds greater than subcritical speed.
- Chapter 5 introduces the speed optimization model developed in this PhD. An overview of EcoNav modules is first given, then the methods used for each of its modules are described.
- Chapter 6 focuses on the validation of EcoNav modules and its application to a real case study. In this chapter, the surrogate model techniques and optimization methods presented in chapter 4 are compared and analysed to determine which ones are the most suited for EcoNav. Once these methods have been selected, the speed optimization model is used to simulate a real case: the itinerary of the self-propelled ship Oural on river Seine, between the locks of Chatou and Poses. The effect of the ship trajectory and travel duration on fuel consumption is also investigated.
- Chapter 7 gives the conclusion of this work and some suggestions for future work.

The results presented in this manuscript were presented and published in 3 international conferences (Linde et al., 2015b,c,d), 2 national conferences (Linde et al., 2014, 2015a) and a journal paper (Linde et al., 2016).

Part I.

Hydrodynamic model for ship resistance

CHAPTER 1

Model equations and numerical resolution

This chapter describes the ship resistance numerical model developed in this PhD. First the fluid solver is presented by detailing the hydrodynamic equations, the turbulence and free surface models, the boundary conditions used and the numerical solver parameters. Then the method used to model ship squat is explained and the coupling between the 3D hydrodynamic model and the ship movement model is described.

1.1. Hydrodynamic equations

The hydrodynamic model developed in this PhD is based on the resolution of the Reynolds Averaged Navier-Stokes (RANS) equations with Ansys Fluent 13 solver. The following assumptions are made for the resolution process:

- the fluid is assumed to be isotropic, incompressible, homogeneous and Newtonian;
- the flow is steady and three dimensional;
- surface tension at the interface air-water is neglected.

1.1.1. Mass equation

The continuity equation states that the increase rate of mass in an infinitesimally small control volume is equal to the net rate of mass flux through its bounding surface. The equation for conservation of mass, also called continuity equation, is as follows:

$$\frac{\partial \rho}{\partial t} + \nabla \cdot (\rho \mathbf{u}) = 0 \tag{1.1}$$

where ρ is the fluid density, $\mathbf{u} = (u, v, w)$ is the velocity vector and ∇ is the differential operator $(\partial/\partial x, \partial/\partial y, \partial/\partial z)$. In the case of an incompressible fluid, the density ρ is constant and eq. (1.1) can be rewritten as follows:

$$\nabla \cdot (\rho \mathbf{u}) = 0 \tag{1.2}$$

In Cartesian coordinates, with Einstein summation convention, eq. (1.2) is written:

$$\frac{\partial u_i}{\partial x_i} = 0 \tag{1.3}$$

where the index i indicates the i^{th} component of the vector.

1.1.2. Momentum equation

The momentum equation states that the rate of change for a small control volume is equal to the net flow rate of momentum through the surface of the control volume plus the sum of the forces acting on the volume:

$$\frac{\partial \rho \mathbf{u}}{\partial t} + \nabla \cdot (\rho \mathbf{u}\mathbf{u}) = \mathbf{F} + \nabla \cdot \boldsymbol{\sigma} \tag{1.4}$$

where $\mathbf{F}$ accounts for body forces, $\boldsymbol{\sigma} = -p\mathbf{I} + \boldsymbol{\tau}$ is the Cauchy stress tensor, sum of the deviatoric stress tensor (or viscous stress tensor) $\boldsymbol{\tau}$ and the normal stress tensor $-p\mathbf{I}$, with $\mathbf{I}$ the 3×3 identity matrix. By expanding the terms on the left side of eq. (1.4) and using the continuity equation eq. (1.1), the momentum equation can be simplified:

$$\rho(\frac{\partial \mathbf{u}}{\partial t} + \mathbf{u} \cdot \nabla \mathbf{u}) = \mathbf{F} + \nabla \cdot \boldsymbol{\sigma} \tag{1.5}$$

In the case of a Newtonian fluid, Cauchy stress tensor can be written as follows:

$$\boldsymbol{\sigma} = -(p + \frac{2}{3}\mu\nabla \cdot \mathbf{u})\mathbf{I} + \mu(\nabla\mathbf{u} + (\nabla\mathbf{u})^T) \tag{1.6}$$

where μ is the dynamic viscosity. Inserting eq. (1.6) into eq. (1.4) gives the Navier-Stokes equation describing a compressible Newtonian fluid:

$$\rho(\frac{\partial\mathbf{u}}{\partial t} + \mathbf{u}\cdot\nabla\mathbf{u}) = -\nabla p + \nabla\cdot\mu(\nabla\mathbf{u} + (\nabla\mathbf{u})^T) - \nabla(\frac{2}{3}\mu\nabla\cdot\mathbf{u}) + \mathbf{F} \tag{1.7}$$

In the case of an incompressible fluid, eq. (1.7) simplifies as follows:

$$\rho(\frac{\partial\mathbf{u}}{\partial t} + \mathbf{u}\cdot\nabla\mathbf{u}) = -\nabla p + \mu\nabla^2\mathbf{u} + \mathbf{F} \tag{1.8}$$

In Cartesian coordinates, with Einstein summation convention, eq. (1.8) is written:

$$\frac{\partial u_i}{\partial t} + u_j\frac{\partial u_i}{\partial x_j} = -\frac{1}{\rho}\frac{\partial p}{\partial x_i} + \nu\frac{\partial}{\partial x_j}(\frac{\partial u_i}{\partial x_j}) + \frac{1}{\rho}F_i \quad i,j = 1,2,3 \tag{1.9}$$

where the index i indicates the i^{th} component of the vector and $\nu = \frac{\mu}{\rho}$ is the kinematic viscosity. Using eq. (1.3), the second term of eq. (1.9) can be expressed as follows:

$$u_j\frac{\partial u_i}{\partial x_j} = \frac{\partial u_j u_i}{\partial x_j} - u_i\frac{\partial u_i}{\partial x_j} = \frac{\partial u_j u_i}{\partial x_j} \tag{1.10}$$

The last term on the right hand side of eq. (1.9) can also be written:

$$\nu\frac{\partial^2 u_i}{\partial x_j x_j} = \frac{1}{\rho}\frac{\partial\tau_{ij}}{\partial x_j} \tag{1.11}$$

where $\tau_{ij} = \mu S_{ij} = \mu(\frac{\partial u_i}{\partial x_j} + \frac{\partial u_j}{\partial x_i})$. The momentum equation can then be expressed as follows:

$$\frac{\partial u_i}{\partial t} + \frac{\partial(u_j u_i)}{\partial x_j} = -\frac{1}{\rho}\frac{\partial p}{\partial x_i} + \frac{1}{\rho}\frac{\partial\tau_{ij}}{\partial x_j} + \frac{1}{\rho}F_i \quad i,j = 1,2,3 \tag{1.12}$$

The Navier-Stokes equations cannot be practically solved for turbulent flow cases. Indeed, running a direct numerical simulation (DNS) in which the Navier-Stokes equations are solved without a turbulence model requires to resolve the whole range of spatial and temporal scales of the turbulence. Therefore, a compututational mesh fine enough to resolve the smallest eddies in the flow is needed and the

power necessary to run such simulations is usually beyond that of today's computers and supercomputers. In most engineering applications, the Reynolds Averaged Navier-Stokes (RANS) equations are used instead.

1.1.3. Reynolds Averaged Navier-Stokes equations

In order to derive the RANS equations, the Reynolds decomposition is used. This decomposition separates the flow variables into a mean component (time-averaged) and a fluctuating component. The mean values of velocity, pressure and stress are respectively noted U_i, P and T_{ij} whereas the fluctuating component are denoted u'_i, p' and τ'_{ij}. Therefore:

$$u_i = U_i + u'_i \quad ; \quad p = P + p' \quad ; \quad \tau_{ij} = T_{ij} + \tau'_{ij} \tag{1.13}$$

One of the proprieties of the Reynolds decomposition is that the mean of the fluctuating component is equal to zero:

$$\overline{u'_i} = \overline{p'} = \overline{\tau'_{ij}} = 0 \tag{1.14}$$

With this decomposition, the continuity equation eq. (1.1) becomes:

$$\frac{\partial(U_i + u'_i)}{\partial x_i} = 0 \tag{1.15}$$

Averaging eq. (1.15) gives:

$$\frac{\partial U_i}{\partial x_i} = 0 \quad ; \quad \frac{\partial u'_i}{\partial x_i} = 0 \tag{1.16}$$

Introducing the Reynolds decomposition in the momentum equation for incompressible fluid (eq. (1.12)) gives:

$$\frac{\partial(U_i + u'_i)}{\partial t} + (U_j + u'_j)\frac{\partial(U_i + u'_i)}{\partial x_j} = -\frac{1}{\rho}\frac{\partial(P + p')}{\partial x_i} + \frac{1}{\rho}\frac{\partial(T_{ij} + \tau'_{ij})}{\partial x_j} + \frac{1}{\rho}F_i \tag{1.17}$$

Time-averaging eq. (1.17) yields:

$$\frac{\partial U_i}{\partial t} + \frac{\partial(U_j U_i)}{\partial x_j} = -\frac{1}{\rho}\frac{\partial P}{\partial x_i} + \frac{1}{\rho}\frac{\partial}{\partial x_j}(T_{ij} + R_{ij}) + \frac{1}{\rho}(F_i) \tag{1.18}$$

where $R_{ij} = R_{ji} = -\rho\overline{u_i' u_j'}$ is the Reynold Stress. This quantity is a correlation between two fluctuating velocity components and can be interpreted as an additional stress. Moreover, this quantity is unknown and therefore, the equation system eqs. (1.16) and (1.18) is not closed. In order to compute the term R_{ij}, a turbulence model is required.

1.2. Turbulence modelling

In order to solve the RANS equations, it is necessary to model the Reynolds stress term R_{ij} as a function of the mean flow, therefore linking the fluctuating part of the velocity to its mean part. This process is called turbulence modelling. Almost every engineering applications requiring CFD simulations are turbulent flows and need a turbulence model. A lot of effort has been put in the past 40 years to develop turbulence models and an overview of existing turbulence model can be found in (Wilcox et al., 1998). However, all turbulence models require empirical constants and no turbulence model working for all possible conditions currently exists. The existing RANS turbulent models can mainly be sorted in the following categories:

- linear eddy viscosity models;
- non linear eddy viscosity models;
- Reynolds stress models.

Among the linear eddy viscosity models, the following categories can be distinguished:

- zero-equation models with no transport (differential) equations used for turbulent quantities;
- one-equation models based on one transport equation for turbulence;
- two-equation models with two transport equations.

Two-equations linear eddy viscosity models have been widely used in ship hydrodynamic simulations. All linear eddy viscosity models are based on the Boussinesq assumption (Boussinesq, 1877).

1.2.1. The Boussinesq assumption

The Boussinesq approximation assumes that the turbulent eddies can be modelled with an eddy viscosity μ_T and the Reynolds stresses R_{ij} can be calculated from the rate of stress tensor S_{ij} in the same way as viscous stresses:

$$R_{ij} = \mu_T S_{ij} - \frac{2}{3}\rho k \delta_{ij} \tag{1.19}$$

where $k = \frac{1}{2}\overline{u_i' u_i'}$ is the turbulent kinetic energy per unit of mass and δ_{ij} is the Kronecker delta:

$$\delta_{ij} = \begin{cases} 1 & \text{for } i = j \\ 0 & \text{for } i \neq j \end{cases} \tag{1.20}$$

Dimensional analysis from eq. (1.19) yields that the turbulent viscosity μ_T shall have the dimension $[kg/(m \cdot s)]$ which can be expressed as a product of a turbulent velocity scale ϑ and a length scale l:

$$\mu_T = const \cdot \rho \vartheta l \tag{1.21}$$

To numerically compute those two quantities, the most commonly used two-equations turbulence model are:

- $k - \varepsilon$ model;
- $k - \omega$ model;
- $k - \omega$ SST model.

The standard $k - \varepsilon$ model is used to solve the RANS equations.

1.2.2. $k - \varepsilon$ turbulence models

The standard $k-\varepsilon$ model (Launder and Spalding, 1974) is the most common model used in CFD to simulate turbulent flows. This model is based on transport equations for the turbulence kinetic energy k and its dissipation rate ε. The turbulent kinetic energy quantifies the mean kinetic energy per unit mass associated with eddies and it is expressed in $[m^2/s^2]$. The turbulent dissipation rate determines the rate of dissipation of the turbulent kinetic energy and its dimensions are $[m^2/s^3]$. Those two quantities can be linked to the turbulent velocity and length scale with the

following equations:

$$\vartheta = k^{1/2} \quad ; \quad l = \frac{k^{3/2}}{\varepsilon} \tag{1.22}$$

The transport equations for the standard $k-\varepsilon$ model are:

$$\frac{\partial}{\partial t}(\rho k) + \frac{\partial}{\partial x_i}(\rho k U_i) = \frac{\partial}{\partial x_j}\left[\left(\mu + \frac{\mu_t}{\sigma_k}\right)\frac{\partial k}{\partial x_j}\right] + P_k - \rho\varepsilon \tag{1.23}$$

$$\frac{\partial}{\partial t}(\rho \varepsilon) + \frac{\partial}{\partial x_i}(\rho \varepsilon U_i) = \frac{\partial}{\partial x_j}\left[\left(\mu + \frac{\mu_t}{\sigma_\varepsilon}\right)\frac{\partial \varepsilon}{\partial x_j}\right] + C_{1\varepsilon}\frac{\varepsilon}{k}P_k - C_{2\varepsilon}\rho\frac{\varepsilon^2}{k} \tag{1.24}$$

where P_k represents the generation of turbulent kinetic energy due to the mean velocity gradients, $C_{1\varepsilon}$ and $C_{2\varepsilon}$ are constants of the model, and σ_k and σ_ε are the turbulent Prandtl numbers for k and ε. P_k and μ_t are calculated as follows:

$$\mu_t = \rho C_\mu \frac{k^2}{\varepsilon} \tag{1.25}$$

$$P_k = -\rho\overline{u_i' u_j'}\frac{\partial U_j}{\partial x_i} = 2\mu_T S_{ij} S_{ij} \tag{1.26}$$

For the standard $k-\varepsilon$ model, the constants have the following default values: $C_{1\varepsilon} = 1.44$, $C_{2\varepsilon} = 1.92$, $C_\mu = 0.09$, $\sigma_k = 1.0$ and $\sigma_\varepsilon = 1.3$.
The standard $k-\varepsilon$ model is the most validated turbulent model used in applications ranging from industrial to environmental flows. However, it has been shown to perform poorly in various configurations (Bradshaw, 1987) such as flows with large adverse pressure gradients, unconfined flows, curved boundary layers, rotating flows and non circular ducts. Several attempts have been made to improve this model and the most successful improvements are the Re-Normalisation Group (RNG) $k-\varepsilon$ model (Yakhot et al., 1992) and the Realizable $k-\varepsilon$ model (Shih et al., 1995). These models provide new formulations for the two transport equations.

1.3. Free surface modelling

In order to correctly model the flow around the ship's hull, it is important to determine the location of the free surface. The main approaches commonly used to model the free surface can be sorted in the following categories:

- interface-tracking methods, which use a boundary fitted-grid and the free

surface is tracked by moving a boundary located at the interface between two fluids;

- interface-capturing methods, which compute the flow of both fluids on a fixed grid and determine where the boundary between the two fluids is located;
- hybrid methods where elements from both interface-tracking and surface-capturing methods are used.

In numerical ship hydrodynamic simulations, two interface-capturing methods are mainly used: the Volume of Fluid (VOF) method, firstly published by Hirt and Nichols (1981) and the Level Set method proposed by Osher and Sethian (1988). The VOF method uses a transport equation for the volume fraction α_k of each fluid (k denotes the k^{th} fluid used in the model) in the computational cell. In our case, only two fluids are used: water and air. The water volume fraction α in a cell is defined such that $\alpha = 1$ means that the cell is completely filled with water, and $\alpha = 0$ means that it is filled with air. The free surface is located within a zone where $0 < \alpha < 1$. Usually, $\alpha = 0.5$ is used to define the location of the free surface. Figure 1.1 illustrates the concept of volume fraction to capture the free surface.

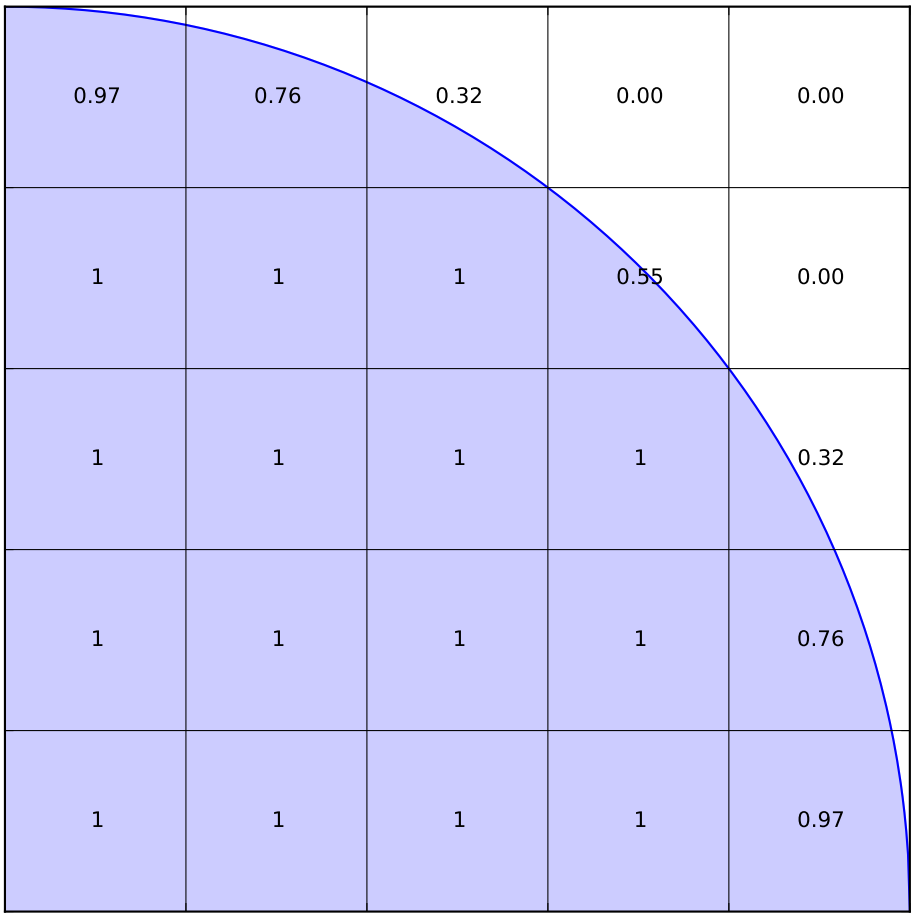

Figure 1.1.: *Free surface capture: water volume fraction in control volume*

The transport equation for α in the case of an incompressible fluid is given by:

$$\frac{\partial \alpha}{\partial t} + \frac{\partial}{\partial x_j}(\alpha u_j) = 0 \tag{1.27}$$

The interpolation at the interface between water and air is done with the modified HRIC scheme (Muzaferija, 1988)

1.4. Boundary conditions

In this study, only the case of a ship sailing at the centre of the waterway is considered. Therefore, the channel presents a symmetric flow configuration and only half of the domain is modeled. In this section, the boundary conditions used for the numerical model are described. Figure 1.2 below shows a general view of the

computational domain and the notations used for the boundaries.

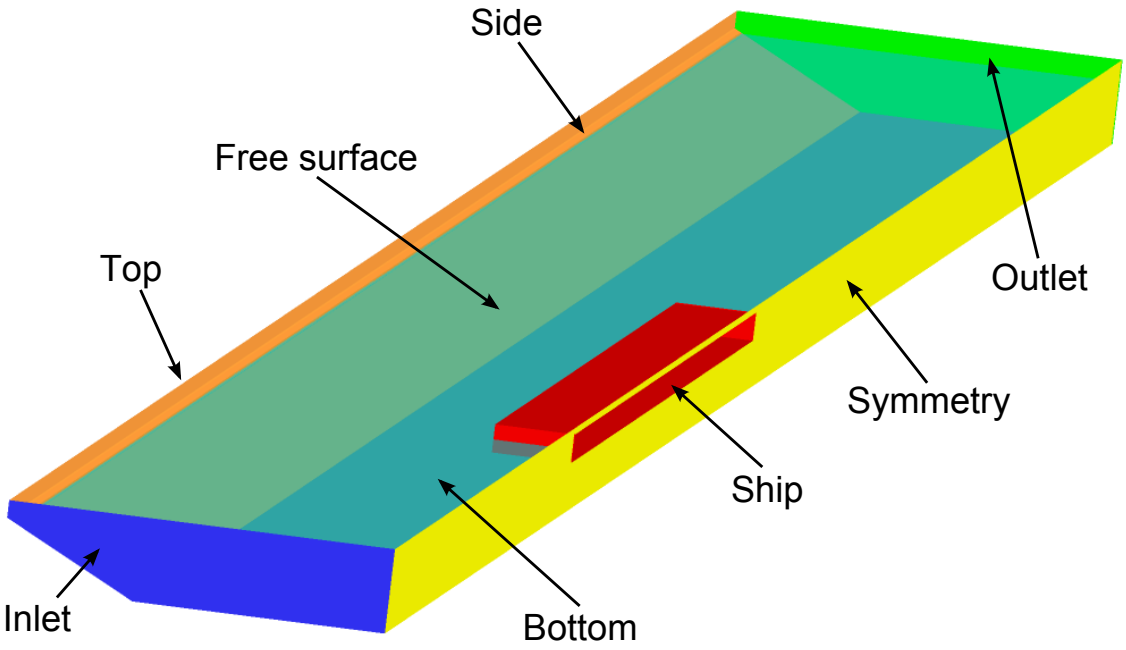

Figure 1.2.: *General view of the computational domain and the notations used for the boundaries*

1.4.1. Inlet condition

Ansys Fluent 13.0 User Guide recommends using pressure conditions at the inlet and the outlet when steady and non oscillating drag is the main objective (Ansys, 2010b). Therefore, at the inlet, the total pressure P_{in}, which is the sum of the dynamic and static pressure, is computed by using the following relationship:

$$P_{in} = \frac{1}{2}\rho V^2 + (\rho - \rho_0)(\mathbf{k}(\mathbf{b} - \mathbf{a})) \tag{1.28}$$

where $\mathbf{a}$ and $\mathbf{b}$ are respectively the position vectors of any point on the free surface and of the face centroid where the pressure is calculated, $\mathbf{k}$ is the unit vector of gravity, ρ is the density of the mixture in the cell and ρ_0 is the reference density set as the air density. The boundary conditions for the kinetic energy k, the turbulent dissipation rate ε and the specific turbulent dissipation rate ω can be calculated

from the following formulas:

$$k = \frac{3}{2}(UI)^2 \tag{1.29}$$

$$\varepsilon = C_\mu \frac{k^{3/2}}{l} \tag{1.30}$$

$$\omega = C_\mu^{-1/4} \frac{\sqrt{k}}{l} \tag{1.31}$$

where U is the mean flow velocity at the inlet, I is the turbulence intensity specified at the inlet, C_μ is the model constant defined in eq. (1.25) and l is usually evaluated by the following expression (Ansys, 2010b):

$$l = 0.07L \tag{1.32}$$

where L is a characteristic dimension usually taken as the hydraulic diameter for open-channel flow.

1.4.2. Outlet condition

At the outlet, the static pressure P_{out} is specified and calculated as follows:

$$P_{out} = (\rho - \rho_0)(\mathbf{k}(\mathbf{b} - \mathbf{a})) \tag{1.33}$$

In Ansys Fluent, the outlet pressure can be specified either by prescribing the local height, the constant pressure or the neighbouring cell pressure. The volume fraction at the outlet α_{out} is set to 0.5 at the free surface level, 1 below the free surface level and 0 above.

1.4.3. Wall boundary conditions

Moving walls at vessel speed V with no slip condition were specified for the bottom and the side of the domain. The moving wall condition is applied to take into account the effect of the river bed and side bank on hydrodynamic forces and therefore the relative velocity between the ship and the bank's walls. For the ship' hull, stationary wall with no slip condition is applied.

1.4.4. Near-wall treatment

Turbulent flows are significantly affected by the presence of walls. The kinematic boundary condition reduces the normal velocity component thus the entrainment rate and the no-slip boundary condition demands that the tangential flow velocity be identical to the wall's tangential speed which has an impact on the mean velocity field. The walls being the main source of mean turbulence and vorticity, accurately modelling the flow in the near-wall region is very important for the fidelity of the numerical solutions. The near-wall region can be divided into three layers:

- the viscous sublayer, where the flow is almost laminar, the turbulent stress negligible and the viscous stress large;
- the buffer layer, where the effect of molecular and turbulent viscosity is equally important;
- the fully turbulent region, also called log-law region, where the turbulent stress is larger than the viscous stress.

Figure 1.3 illustrates the subdivisions of the near-wall region, plotted in semi-log coordinates.

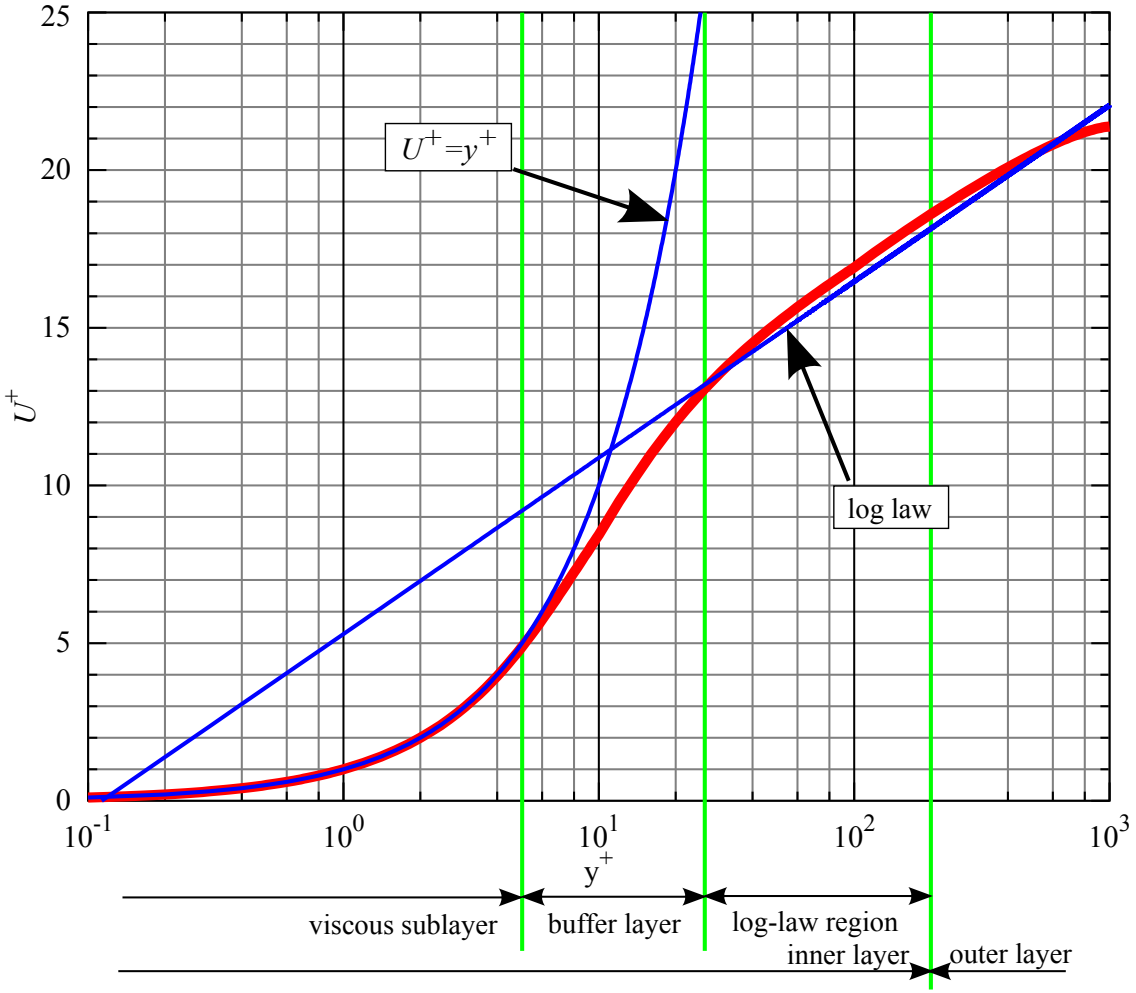

Figure 1.3.: *Subdivisions of the near-wall region*
Source: *Aoko Moriuta - CC-BY-SA)*

In this figure, y^+ is the non-dimensional wall distance for a wall-bounded flow and u^+ is the dimensionless velocity parallel to the wall. These quantities are calculated with the following formula:

$$y^+ = \frac{yu_\tau}{\nu} \tag{1.34}$$

$$u^+ = \frac{u}{u_\tau} \tag{1.35}$$

where y is the normal distance from the wall, u_τ is the friction velocity, defined as $\sqrt{\frac{\tau_w}{\rho}}$ and u is the velocity parallel to the wall.
Two strategies can be used to solve the near-wall region flow:

- not solving the flow in the viscous sublayer and the buffer layer (regions affected by viscosity) and instead use semi-empirical formulas called "wall functions" to model the flow in that inner region;
- modifying the turbulence models to resolve the viscosity affected region with a refined mesh in that zone. This method is called "near-wall modelling".

These two approaches are illustrated in Figure 1.4.

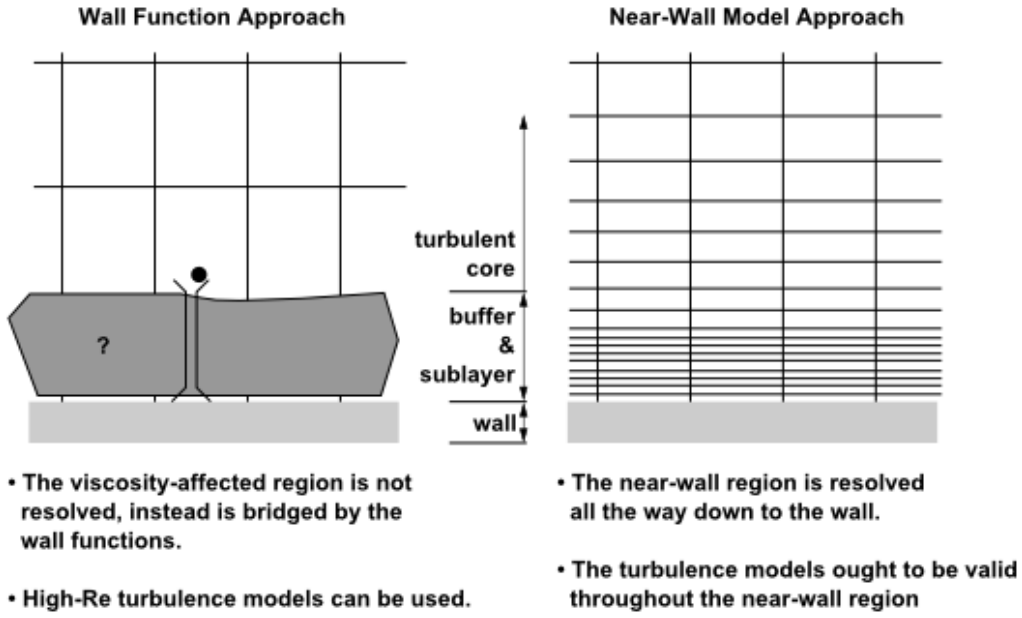

Figure 1.4.: *Near-wall region modelling approaches*
Source: *Ansys Fluent 13.0 Theory Guide (Ansys, 2010a)*

Standard wall function for $k-\varepsilon$ turbulence model

Standard wall functions are used with the $k-\varepsilon$ turbulence model. They are based on the work of Launder and Spalding (1974) and are widely used in industrial flows. The law-of-the-wall for the mean velocity gives:

$$U^* = \frac{1}{\kappa} ln(Ey^*) \tag{1.36}$$

where

$$U^* = \frac{\rho U_P C_\mu^{1/4} k_P^{1/2}}{\tau_w} \tag{1.37}$$

is the dimensionless near-wall velocity,

$$y^* = \frac{\rho C_\mu^{1/4} k_P^{1/2} y_P}{\mu} \tag{1.38}$$

is the dimensionless distance from the wall, $\kappa = 0.4187$ is the von Kármán constant, $E = 9.793$ is an empirical constant, U_P the mean velocity of the fluid at the near-wall node P, k_P is the turbulent kinetic energy at the near-wall node P and y_P is the distance from point P to the wall.
The standard wall function also allows to calculate the turbulent quantities in the near-wall region. The k eq. (1.23) is solved on the whole domain including the wall-adjacent cells and the boundary condition imposed for k at the wall is:

$$\frac{\partial k}{\partial n} = 0 \tag{1.39}$$

where n is the local coordinate normal to the wall. In the near-wall region, it is assumed that the production of k (P_k) and its dissipation rate ε are equal. Moreover, the production of kinetic energy is based on the log-law and therefore:

$$P_k = \tau_w \frac{\partial U}{\partial y} = \tau_w \frac{\tau_w}{\rho \kappa k_P^{1/2} y_P} \tag{1.40}$$

and ε is calculated as follows:

$$\varepsilon_P = \frac{C_\mu^{3/4} k_P^{3/2}}{\kappa y_P} \tag{1.41}$$

1.4.5. Symmetry condition

For the symmetry plane and the top, the normal velocity component is set to zero:

$$\mathbf{U_s} \cdot \mathbf{n} = 0 \tag{1.42}$$

and the gradients of all flow variables are also set to zero:

$$\begin{aligned} \frac{\partial \mathbf{U_s}}{\partial \mathbf{n}} = 0; \quad \frac{\partial k_s}{\partial \mathbf{n}} = 0; \quad \frac{\partial \varepsilon_s}{\partial \mathbf{n}} = 0 \\ \frac{\partial \alpha_s}{\partial \mathbf{n}} = 0; \quad \frac{\partial \omega_s}{\partial \mathbf{n}} = 0; \quad \frac{\partial P_s}{\partial \mathbf{n}} = 0 \end{aligned} \tag{1.43}$$

where $\mathbf{U_s}$, k_s, ε_s, α_s, ω_s and P_s are the flow variables values at the symmetry and top plane.

1.5. Numerical solver

1.5.1. Finite volume method

ANSYS Fluent 13.0 solves the RANS equations Equations (1.16) and (1.18) with a control-volume-based technique consisting of:

- Decomposition of the domain into control volumes (CV) based on the computational grid.
- Integration of the governing equation for each CV.
- Approximation of integrals by linearisation.
- Approximation of function values and derivatives by interpolation with nodal values.
- Assembling and solution of the resultant linear equation system to obtain updated values of the problem variables.

General transport equation

The RANS and turbulence equations can be written in a common format which is the general transport equation for a scalar ϕ:

$$\underbrace{\frac{\partial \rho\phi}{\partial t}}_{\text{transient term}} + \underbrace{\nabla\cdot(\rho\mathbf{V}\phi)}_{\text{convective term}} = \underbrace{\nabla\cdot(\Gamma_\phi\nabla\phi)}_{\text{diffusion term}} + \underbrace{S_\phi}_{\text{source term}} \tag{1.44}$$

where Γ_ϕ is the diffusion coefficient for ϕ and S_ϕ is the source of ϕ per unit volume. This equation can be written in integral form for an arbitrary control volume V_C in which the volume integrals of the convection and diffusion terms are replaced by surface integrals through the use of the divergence theorem:

$$\int_{V_C}\frac{\partial \rho\phi}{\partial t}dV_C + \oint_{\partial V_C}(\rho\mathbf{V}\phi)\cdot d\mathbf{S} = \oint_{\partial V_C}(\Gamma_\phi\nabla\phi)\cdot d\mathbf{S} + \int_{V_C}S_\phi dV_C \tag{1.45}$$

where $\oint_{\partial V_C}$ represents the surface integral over the control volume V_C.
The discretization of Equation (1.45) on a general control volume yields:

$$\frac{\partial \rho\phi}{\partial t}V_C + \sum_{f}^{N_{faces}} (\rho_f \mathbf{V_f}\phi_f) \cdot \mathbf{A_f} = \sum_{f}^{N_{faces}} (\Gamma_\phi \nabla\phi_f) \cdot \mathbf{A_f} + S_\phi V_C \tag{1.46}$$

where N_{faces} is the number of faces enclosing cell, ϕ_f the value of ϕ convected through face f, $(\rho_f \mathbf{V_f}\phi_f) \cdot \mathbf{A_f}$ the mass flux through the face, $\mathbf{A_f}$ the area of face f and $\nabla\phi_f$ the gradient of ϕ at face f.

Discretization of the convection terms

The face values ϕ_f for the convection terms in Equation (1.46) are evaluated with a 1st order upwind scheme for the turbulent equations and a 2nd order upwind scheme for the momentum equation. In the 1st order upwind scheme, the face value ϕ_f is set equal to the cell-center value of ϕ in the upstream cell. For the 2nd order upwind scheme, the face value ϕ_f is computed with the following expression:

$$\phi_f = \phi + \nabla\phi \cdot \mathbf{r} \tag{1.47}$$

where ϕ and $\nabla\phi$ are the cell-centered value and its gradient in the upstream cell; and $\mathbf{r}$ is the displacement vector from the upstream cell centroid to the face centroid.

Discretization of the diffusion terms

A 2nd order-accurate central differencing scheme is used for the discretization of the diffusion terms:

$$\phi_f = \frac{1}{2}(\phi_0 + \phi_1) + \frac{1}{2}(\nabla\phi_0 \cdot \mathbf{r_0} + \nabla\phi_1) \cdot \mathbf{r_1} \tag{1.48}$$

where the indices 0 and 1 refer to the cells sharing face f; and $\nabla\phi_0$ and $\nabla\phi_1$ are the reconstructed gradients at cells 0 and 1.

Temporal discretization

A first order implicit time integration is used for the temporal integration. Equation (1.46) can be formulated as follows:

$$\frac{\partial \phi}{\partial t} = F(\phi) \tag{1.49}$$

where F is a function incorporating every spatial discretization terms. The first order implicit time integration scheme is then given by:

$$\frac{\phi^{n+1} - \phi^n}{\Delta t} = F(\phi^{n+1}) \tag{1.50}$$

where Δt is the time step, n indicates the variable value at time t and $n+1$ the value at time $t + \Delta t$. The advantage of such a scheme is that it is unconditionally stable with respect to time step size.

Evaluation of gradients

The gradient $\nabla\phi$ of a scalar ϕ is used to discretize the convection and diffusion terms in Equation (1.46). The Least Squares Cell-Based method is used for the gradient computation. In this method the gradient $\nabla\phi$ is assumed to vary linearly and the change in centroid values between C_i and C_0 can be computed as:

$$(\phi_{C_i} - \phi_{C_0}) = (\nabla\phi)_{C_0} \cdot (\mathbf{r_i} - \mathbf{r_0}) \tag{1.51}$$

By writing the same equation for the surrounding cells, the following system is obtained:

$$\mathbf{J}(\nabla\phi)_{C_0} = \mathbf{\Delta}_{\boldsymbol{\phi}} \tag{1.52}$$

where $\mathbf{J}$ is a matrix with the coefficients of the system which are function of the geometry and $\mathbf{\Delta}_{\boldsymbol{\phi}}$ is a column vector with $(\Delta_\phi)_i = \phi_i - \phi_0$. This system is usually over-determined because cell C_0 has more neighbours than the gradient vector has components. Therefore it is solved by minimizing the error with the least-square method.

1.5.2. Pressure-correction method

The governing equations for the RANS model are the continuity equation (eq. (1.16)), the momentum equation (eq. (1.18)) and the turbulence model equations (see Section 1.2). The main issue in solving those equations is that there is no explicit equation for computing the pressure field appearing in the momentum equation. The pressure gradient in Equation (1.18) drives the velocity which has to satisfy the continuity equation. As a result, there is an indirect coupling between the pressure distribution and the continuity equation. The steady-state continuity and momentum equations are given in integral form to illustrate the pressure-correction method:

$$\oint \rho \mathbf{V} \cdot d\mathbf{S} = 0 \tag{1.53}$$

$$\oint (\rho \mathbf{V}\mathbf{V}) \cdot d\mathbf{S} = -\oint p\mathbf{I} \cdot d\mathbf{S} + \oint \boldsymbol{\tau} \cdot d\mathbf{S} + \int \mathbf{F} dV_C \tag{1.54}$$

Discretization of the momentum equation

The discretization scheme used for the discretization of the general transport equation Equation (1.44) is applied to discretize the momentum equation. By replacing ϕ with u, the momentum equation projected along the x axis gives:

$$a_P u = \sum_{nb} a_{nb} u_{nb} + \sum p_f \mathbf{S} \cdot \mathbf{i} S \tag{1.55}$$

If the pressure field is known, this equation can be solved to obtain a solution for the velocity field. However, the pressure face values are not known and must be obtained as part of the solution. In ANSYS Fluent, pressure and velocity values are stored at cell centres and therefore the face values of pressure have to be computed with an interpolation scheme. The scheme used in this model is the Body Force Weighted which assumes that the normal gradient of the difference between pressure and body force is constant. The use of this scheme is recommended when large body forces are involved such as buoyancy.

Discretization of the continuity equation

The continuity equation Equation (1.53) is discretized as follow:

$$\sum_{f}^{Nfaces} J_f A_f = 0 \tag{1.56}$$

where $J_f = \rho \mathbf{V_n}$ is the mass flux through face f and V_n is the normal velocity.
In order to prevent unphysical checkerboarding of pressure caused by linear interpolation of cell-centered velocities to the face, ANSYS Fluent uses a similar procedure to that developed by Rhie and Chow (1983). The face value velocity is averaged by using weighting factor based on the a_p coefficients from Equation (1.55) and the face flux J_f is given by:

$$\begin{aligned} J_f &= \rho_f \frac{a_{p,c_0} v_{n,c_0} + a_{p,c_1} v_{n,c_1}}{a_{p,c_0} + a_{p,c_1}} + d_f \left(\left(p_{c_0} + (\nabla p)_{c_0} \cdot \mathbf{r_0} \right) - \left(p_{c_1} + (\nabla p)_{c_1} \cdot \mathbf{r_1} \right) \right) \\ &= \hat{J}_f + d_f (p_{c_0} - p_{c_1}) \end{aligned} \tag{1.57}$$

where p, c_0, p, c_1 and v_{n,c_0},v_{n,c_1} are the pressures and normal velocities of the two cells sharing face f; $\hat{J}_f$ contains the influence of velocities in these cells and d_f is a function of $\overline{a_p}$, the average of the momentum equation coefficients a_p for the cells on each side of face f.

Simple algorithm

The algorithm used to solve the discretized continuity and momentum equation (eqs. (1.56) and (1.57)) is the semi-implicit method for pressure-linked equations (SIMPLE) developed by Patankar and Spalding (1972). In the SIMPLE method, a guessed pressure $p*$ is used to solve the momentum equation (eq. (1.56)) and obtain the velocity field and thus the face flux J_f*. However, this face flux does not satisfy the continuity equation (eq. (1.57)) and a face flux correction J'_f is added to obtain the corrected face flux J_f:

$$J_f = J_f * + J'_f \tag{1.58}$$

The face flux correction is written in the following form:

$$J'_f = d_f(p'_{c_0} - p'_{c_1}) \tag{1.59}$$

where p' is the cell pressure correction.
By introducing Equation (1.58) and Equation (1.59) into Equation (1.57), a discrete equation for the pressure correction p' can be obtained:

$$a_p p' = \sum_{nb} a_{nb} p'_{nb} + b \tag{1.60}$$

where $b = \sum_f^{Nfaces} J_f * A_f$ is the net flow rate in the cell.
The solution to the pressure correction equation (eq. (1.60)) is then used to calculate the corrected pressure:

$$p = p* + \alpha_p p' \tag{1.61}$$

where α_p is the under-relaxation factor for pressure.
The algorithm can be summarized as follows:

1. Start with a guessed pressure field $p*$.
2. Solve the momentum equation to obtain J_f*.
3. Compute the pressure correction p' with Equation (1.60).
4. Calculate p from Equation (1.61) and J_f from Equation (1.58).
5. Solve the transport equation (eq. (1.44)) for turbulence quantities using the new velocity field.
6. Return to step 1 and repeat the process with the new calculated pressure field until convergence.

1.6. Ship squat modelling and resistance calulation

The ship's hull is modelled as a rigid body. The movement of the ship is governed by the rigid body equations of motion for the ship's center of mass G:

$$m\mathbf{a_G} = \mathbf{F} \tag{1.62}$$

$$\frac{d}{dt}(I_G \cdot \boldsymbol{\omega}_\mathbf{G}) = \mathbf{M_G} \tag{1.63}$$

where m is the mass of the body, G is the ship's centre of gravity, $\mathbf{a_G}$ is the acceleration, $\mathbf{F}$ is the sum of the external forces, I_G is the moment of inertia tensor, $\omega_\mathbf{G}$ is the angular velocity and $\mathbf{M_G}$ is the sum of the applied torques. To find the ship equilibrium position, the rigid body motion equations (eqs. (1.62) and (1.63)) are usually solved with a six degrees of freedom (6-DOF) solver, until the body reaches dynamic equilibrium. This method requires to model the transient state and ship oscillations. However, this study considers the equilibrium position and steady state; therefore, the equilibrium position is defined as follows:

$$F_z = (\mathbf{P} + \mathbf{F_f}) \cdot \mathbf{e_z} = (m\mathbf{g} + \iint_S \boldsymbol{\sigma} \cdot \mathbf{n} dS) \cdot \mathbf{e_z} = 0 \tag{1.64}$$

$$M_{Gy} = (\iint_S \mathbf{r} \wedge (\boldsymbol{\sigma} \cdot \mathbf{n})) \cdot \mathbf{e_y} = 0 \tag{1.65}$$

where F_z is the projection of forces on $\mathbf{e_z}$ axis; $\mathbf{P}$ is the weight; m is the mass of the ship; $\mathbf{g}$ is the gravitational acceleration; $\mathbf{F_f}$ is the force from the fluid acting on the hull of the ship which can be decomposed in viscous and pressure forces; $\boldsymbol{\sigma} = \boldsymbol{\tau} - p\mathbf{I}$ is the stress tensor, $\boldsymbol{\tau}$ is the shear stress, p is the pressure, $\mathbf{I}$ is the identity matrix; $\mathbf{n}$ is the normal vector to the hull; S is the wetted surface of the hull; M_{Gy} is the moment projection on $\mathbf{e_y}$ axis and $\mathbf{r} = \mathbf{GM}$ is the position vector.
Newton's method is used to solve this non-linear equation system (eqs. (1.64) and (1.65)). Let $X^N = \begin{pmatrix} z^N \\ \theta^N \end{pmatrix}$ be the vertical position and angle of the gravity centre in a fixed coordinate system and $G(X^N) = \begin{pmatrix} F_z(X^N) \\ M_{Gy}(X^N) \end{pmatrix}$ a function whose components are the sum of the vertical forces F_z and the sum of trim moments M_{Gy} at ship position X^N. The equilibrium position is reached when $G(X^N) = 0$. Newton algorithm iteration is:

$$X^{N+1} = X^N - J^{-1}(X^N)G(X^N) \tag{1.66}$$

where J^{-1} is the inverse of the Jacobian matrix:

$$J = \begin{pmatrix} \frac{\partial F_z}{\partial z} & \frac{\partial F_z}{\partial \theta} \\ \frac{\partial M_{Gy}}{\partial z} & \frac{\partial M_{Gy}}{\partial \theta} \end{pmatrix} \tag{1.67}$$

As the expression of forces and moments acting on the hull cannot be analytically determined, the Jacobian is evaluated with finite differences:

$$J(X^N) = \begin{pmatrix} \frac{F_z(z^N+dz_0,\theta^N)-F_z(z^N,\theta^N)}{dz_0} & \frac{F_z(z^N,\theta^N+d\theta_0)-F_z(z^N,\theta^N)}{d\theta_0} \\ \frac{M_{Gy}(z^N+dz_0,\theta^N)M_{Gy}(z^N,\theta^N)}{dz_0} & \frac{M_{Gy}(z^N,\theta^N+d\theta_0)-M_{Gy}(z^N,\theta^N)}{d\theta_0} \end{pmatrix} \tag{1.68}$$

where dz_0 and $d\theta_0$ are small increments in vertical position and trim angle.
Figure 1.5 illustrates schematically the coupling between fluid and solid models. The forces acting on the hull are computed by solving the RANS fluid equations (eqs. (1.16) and (1.18)). Those forces are then used as input to iterate Newton's method and calculate the displacement of the ship. The ship position is then updated and the fluid equations are solved again.

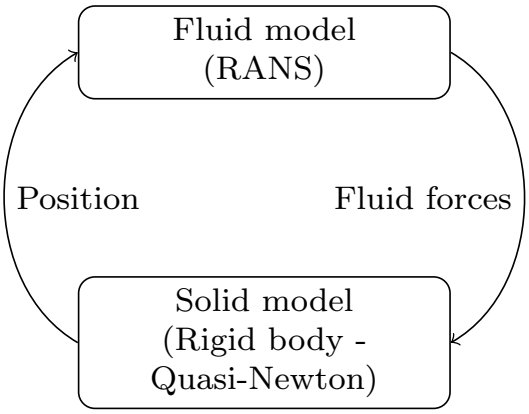

Figure 1.5.: *Fluid-structure interaction*

After each actualization of the position, the solution of the fluid equations is disturbed and n iterative resolutions of the fluid equations are required to reach a new stable solution before changing the ship's position again. Because the Jacobian is evaluated with finite differences, forces tensor $\mathbf{G}$ has to be evaluated at three different positions: $\begin{pmatrix} z^N \\ \theta^N \end{pmatrix}$, $\begin{pmatrix} z^N+dz_0 \\ \theta^N \end{pmatrix}$ et $\begin{pmatrix} z^N \\ \theta^N+d\theta_0 \end{pmatrix}$. As a result, computing the Jacobian can be time consuming. Therefore, a quasi-Newton method is used where the derivative is only calculated once and remains constant throughout the iterative process. This method is implemented in Fluent through the use of user-defined function (UDF). Figure 1.6 shows the quasi-Newton algorithm flowchart.

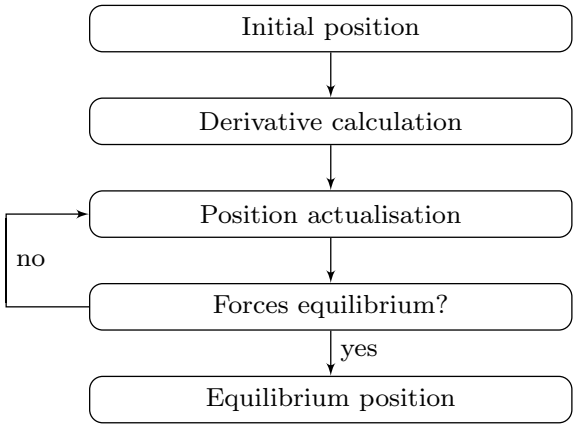

Figure 1.6.: *Numerical resolution process*

The iteration process is stopped when $|F_Z| < 0.1\ N$ and $|M_{Gy}| < 0.1\ N.m$. Once the equilibrium position is reached, the ship resistance is evaluated by calculating pressure and friction force in the longitudinal direction.

1.7. Summary

The fluid equations are solved with the CFD software ANSYS Fluent 13. The finite volume method is used to discretize the domain into a finite set of control volumes where the general conservation (transport) equations are solved. The semi-implicit method for pressure-linked Equations (SIMPLE) is applied to solve the pressure-velocity coupling and the convective terms discretization is performed with the second-order upwind scheme. The k-ε turbulence model (Launder and Spalding, 1974) with standard wall functions is used to model the Reynolds stress term. Free surface and ship waves are tracked with the volume of fluid scheme (Hirt and Nichols, 1981).

The boundary conditions used in this model are similar to those used by Ji et al. (2012). Pressure boundary conditions are used at the inlet and the outlet. For the symmetry and top plane, the normal velocity component and the normal gradient of all flow variables are equal to zero. No-slip boundary conditions with a tangential velocity component equal to the ship speed are specified for the bottom and the side of the domain. The moving wall condition is applied to take into account the effect of the river bed and side bank on hydrodynamic forces and therefore the relative velocity between the ship and the bank. Finally, stationary wall with no slip

condition is applied on the ship's hull.

A Newtonian method is used to find the equilibrium position and avoid modelling the transient oscillations of the ship. The coupling between the 3D hydrodynamic model and the ship movement model is solved iteratively. The forces acting on the hull are computed by solving fluid equations. Those forces are then used as input to iterate Newton's method and calculate the displacement of the ship. The ship position is then updated and the fluid equations are solved again.

CHAPTER 2

Model validation and numerical investigations

The ship resistance model described in chapter 2 is validated with towing tank test conducted by Architecture Navale et Systèmes de Transports (ANAST) researchers at the University of Liege, Belgium (Vandescuren et al., 2013). In this chapter, the towing tank tests carried at ANAST are first introduced, then the mesh generation process used for the numerical model is described. The numerical results with and without sinkage are also compared to study the influence of sinkage on ship resistance and on the accuracy of the method. Additionally, some empirical models are investigated and compared with the accuracy of the numerical method. Finally, the numerical model is used to determine if channel width and water depth restriction contribute to the same amount of ship resistance increase for the same level of restriction. The results of that investigation give insight to whether channel restriction can be characterized by a unique parameter (for instance the blockage ratio) or two parameters to distinguish water depth and channel width effects.

2.1. Liege towing tank experiments

ANAST towing tank is 100 m long, 6 m wide and 4 m deep (Figure 2.1). A platform leaning on rails allows to tow the model ship at speed up to 5 m/s. A fake aluminium bottom and movable PVC banks (Figure 2.2) were used to model restricted water depth and channel breadth.

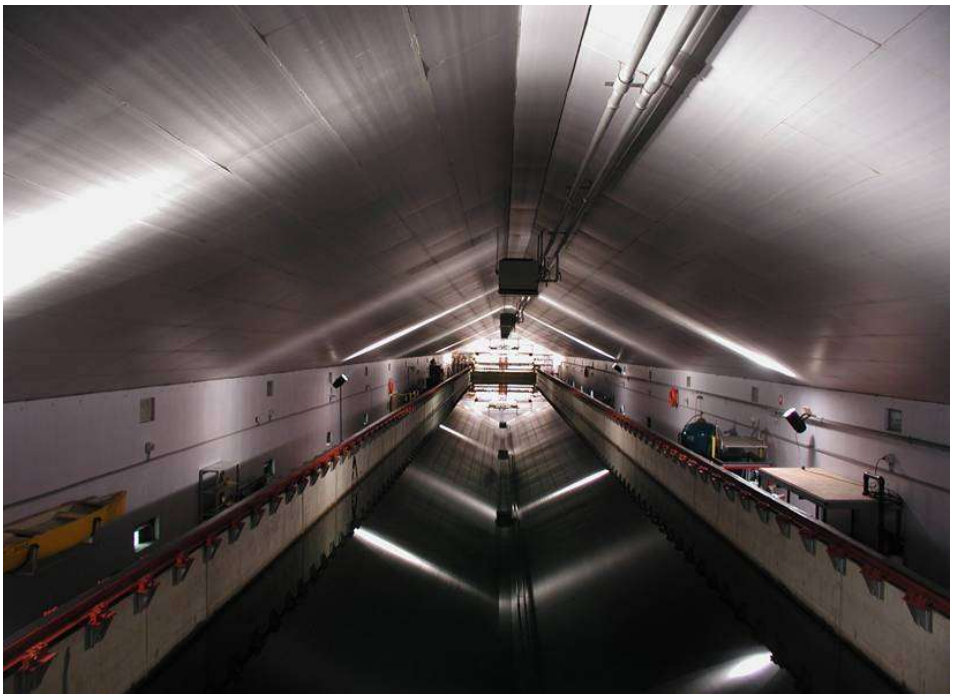

Figure 2.1.: *Liege University towing tank*

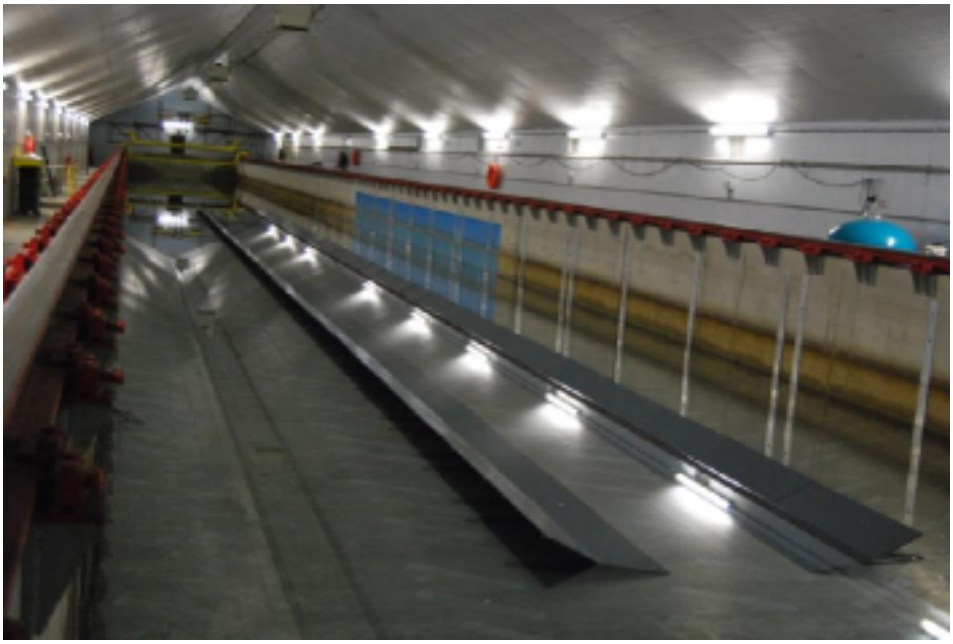

Figure 2.2.: *Towing tank with aluminium fake bottom and moveable PVC banks*

A 1-component dynamometer balance (Figure 2.3) allows to measure trim and sinkage of the ship and a 6-components dynamometer balance (Figure 2.4) measures the forces and momentum acting on the vessel along the 3 axes.

Figure 2.3.: *1-component dynamometer balance*

Figure 2.4.: *6-components dynamometer balance*

In those experiments an inland vessel model (135×11.4 m) without rudder or propeller is used at 1/25 scale. This model ship corresponds to a real self propelled inland vessel such as Bosphore or its sister ship Oural (vessels owned by Compagnie Fluviale de Transport). Self-propelled vessel is predominant for goods transport on European waterways. In 2014, more than half of European Union inland transport of goods were carried by such ships (Eurostat, 2015). Table 2.1 shows the full-scale and model-scale properties of the hull, Figure 2.5 illustrates the hull sections of the ship and Figure 2.6 shows a three-dimensional view of the vessel.

Table 2.1.: *Full scale and model scale properties of the tested inland vessel*

Properties	**Ship**	**Model (1/25)**
Length L $[m]$	135	5.4
Beam B $[m]$	11.4	0.456
Block coefficient C_B $[-]$	0.899	0.899
Wetted surface S $[m^2]$	2104.8	3.367
Cross area of ship $[m^2]$	34.114	0.0545

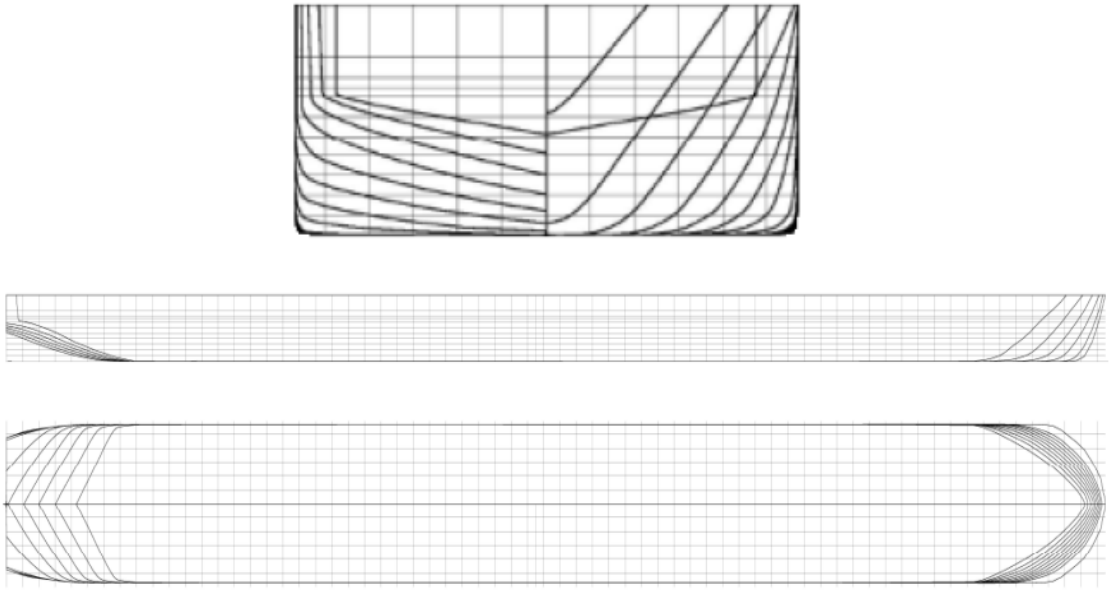

Figure 2.5.: *Hull sections of the inland model ship*

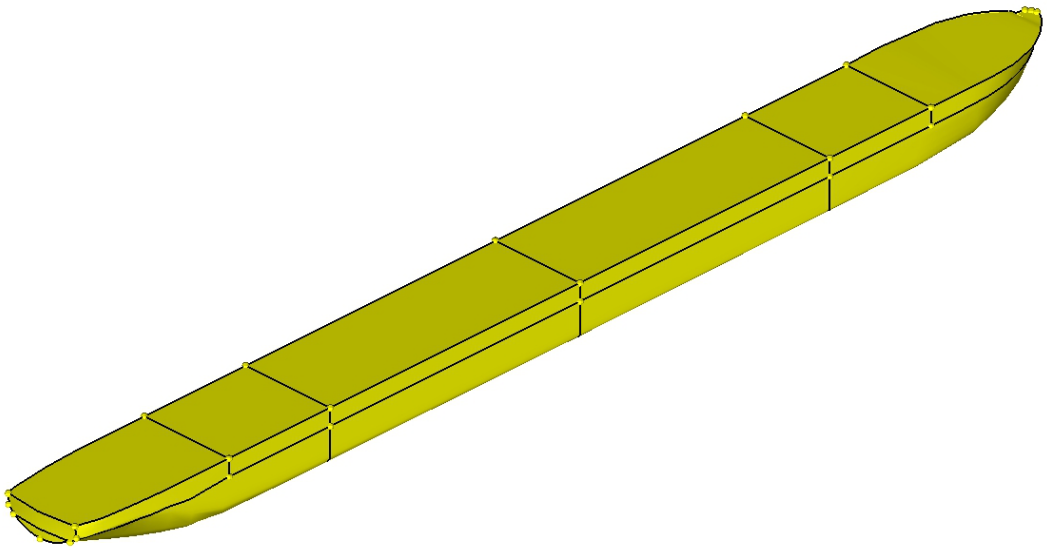

Figure 2.6.: *Three dimensional view of the inland model ship*

A wide range of parameters are tested such as channel width (W), channel depth (H) and ship draft (T). The canal section is trapezoidal with a 2:1 slope. Figure 2.7 illustrates the various configurations tested during those experiments.

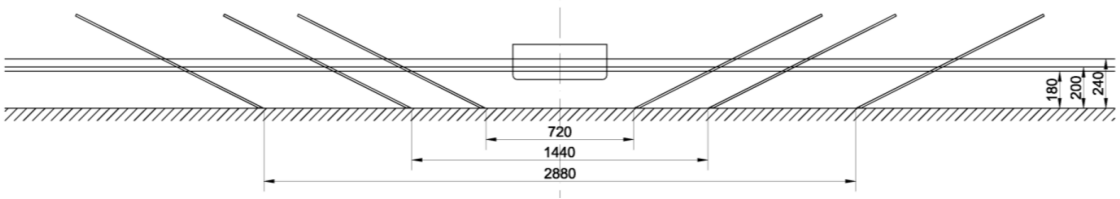

Figure 2.7.: *Numerical resolution process*

Forces and moments acting on the ship, sinkage and trim are recorded during the experiment. The reported uncertainty of the experiment is 5-8 % for the resistance and 1-2% for sinkage. It is worth mentionning that no roughness bands were used at low velocities to trigger the transition to turbulent regime. The different configurations for which the experimental data were compared with numerical results and their associated values for the waterway restriction parameters are listed in Table 2.2.

Table 2.2.: *Modelled configurations and corresponding parameters*

Conf.	$\mathbf{H}$ [m]	$\mathbf{T}$ [m]	$\mathbf{W}$ [m]	$\frac{\mathbf{H}}{\mathbf{T}}$ [-]	$\frac{\mathbf{W}}{\mathbf{B}}$ [-]	$\frac{\mathbf{A_C}}{\mathbf{A_S}}$ [-]	$\mathbf{V}$ [m/s]	$\mathbf{V_L}$ [m/s]	$\mathbf{F_{nh}}$
C1	0.18	0.10	0.72	1.80	1.58	4.26	0.11-0.51	0.58	0.08-0.38
C2	0.18	0.10	1.44	1.80	3.16	7.11	0.22-0.56	0.74	0.17-0.42
C3	0.18	0.10	2.88	1.80	6.32	12.79	0.33-0.67	0.88	0.25-0.50
C4	0.24	0.10	2.88	2.40	6.32	17.68	0.44-0.89	1.10	0.29-0.58
C5	0.18	0.04	2.88	4.50	6.32	31.97	0.44-0.89	1.04	0.33-0.67

V_L=Schijf limiting speed (Schijf, 1949)

Table 2.2 shows that all configurations except configuration 5 present a water depth restriction ($H/T = 1.8 < 4$). From configuration 3 to configuration 1, channel width restriction changes from unrestricted ($W/B = 6.32 > 4$) to highly restricted ($W/B = 1.58 < 4$). From configuration 5 to configuration 3, water-depth restriction changes from unrestricted ($H/T = 5 > 4$) to highly restricted ($H/T = 1.80 < 4$). Finally, all the tested speeds V remain within the subcritical regime, which upper limit is identified by Schijf limiting speed V_L (indicated in Table 2.2).

2.2. Verification studies

2.2.1. Grid generation

The mesh is generated with ANSYS Meshing software and consisted of a 1.3 million-cell structured-unstructured hybrid mesh. Structured elements are used in the computational domain, except around the hull, where an unstructured mesh is generated to remesh the domain during the actualization of the ship position. Estimation of the ship generated wave length λ is used to determine the cell size in x direction. Ji et al. (2012) recommended the use of 10 points per length of the transverse waves. The transverse wave length λ is defined as Sorensen (1997):

$$V^2 = \frac{g\lambda}{2\pi} tanh(\frac{2\pi H}{\lambda}) \tag{2.1}$$

where V is the wave celerity equal to the ship's speed and H is the water depth. For the generated mesh, an average of 10 points per transversal wave length is used in the x and y direction. Additionally, 10 grid points in the vertical direction z are used where the free surface was expected. Around the ship a boundary layer mesh composed of prism layers inflated from the triangular surface mesh of the ship's hull is used. That type of mesh creates high quality geometry elements capable of resolving the boundary layer growth. For turbulent models used with standard wall functions, ITTC guidelines (ITTC, 2011) recommend to place the first grid point at a distance from the ship's wall such that $30 < y^+ < 300$. The non-dimensional wall distance for a wall-bounded flow y^+ is calculated as Larsson and Raven (2010):

$$y^+ = \frac{y u_\tau}{\nu} \tag{2.2}$$

$$u_\tau = V\sqrt{\frac{C_f}{2}} \tag{2.3}$$

$$C_f = \frac{0.058}{{Re_L}^{5/2}} \tag{2.4}$$

where y is the normal distance of the first node from the wall, u_τ is the friction velocity, ν is the fluid kinematic viscosity, C_f is the local skin friction and Re_L is the Reynolds number based on the ship length. The first cell height is chosen to obtain y^+ values above 30.

Figure 2.8 below shows the generated mesh with a focus on the unstructured and boundary layer mesh.

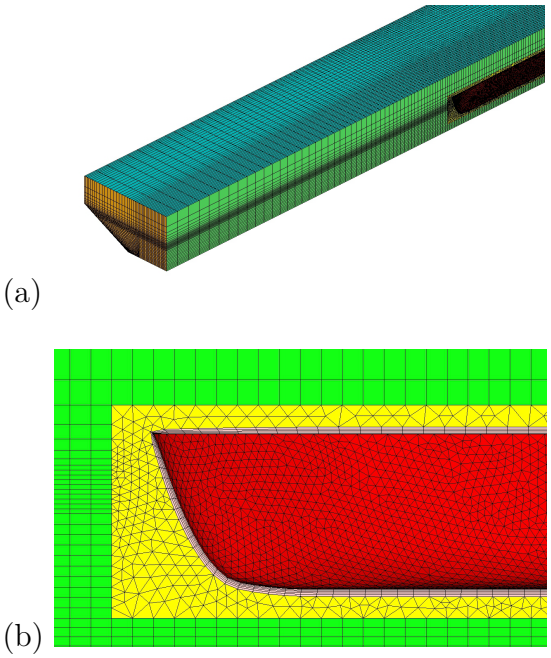

Figure 2.8.: *Generated mesh: (a) meshed domain with higher density on free surface and around ship hull, (b) box with unstructured and boundary layer mesh*

2.2.2. Mesh and time-step converence study

The discretization errors caused by grid-size and time-step resolution are evaluated by performing a verification study for the highest speed (0.67 m/s) of configuration 3. Error usually increases with Froude number (Larsson et al., 2013); therefore, it is expected that for cases with lower Froude number, the numerical uncertainties are lower. The method used in this verification study is the grid convergence index (GCI) developed by Roache (1998) and described in Celik et al. (2008). This method is currently used and recommended by the American Society of Mechanical Engineers (ASME, Celik et al. (2008)) and the American Institute of Aeronautics and Astronautics (AIAA, Cosner et al. (2006)) . Xing and Stern (2010) discussed the deficiencies of the different GCI methods and proposed the factor of safety method to correct it. GCI estimates the numerical error caused by grid-spacing and time-step convergence by expanding the error in a power series with integer powers of grid-spacing or time step as a finite sum. By assuming that the solution lies in the

asymptotic range, only the first term of the series is retained. For both time step and mesh size convergence studies, three solutions are used with refined mesh and time steps. A constant refinement ratio $r_k = \sqrt{2}$ is used in both cases. The mesh convergence analysis is carried out with the medium time step and the time step convergence study is executed with the medium grid. To characterize the type of convergence, the convergence ratio R_k is defined:

$$R_k = \frac{\varepsilon_{k21}}{\varepsilon_{k32}} \tag{2.5}$$

where $\varepsilon_{k21} = \varphi_{k2} - \varphi_{k1}$ and $\varepsilon_{k32} = \varphi_{k3} - \varphi_{k2}$ are the solution changes for medium-fine and coarse-medium solutions, and φ_{k1}, φ_{k2} and φ_{k3} correspond to the solutions for the fine, medium and coarse k^{th} input parameters (time step or grid size). Depending on the value of R_k, four convergence conditions can be found: monotonic convergence ($0 < R_k < 1$), oscillatory convergence ($-1 < R_k < 0$), monotonic divergence ($1 < R_k$) and oscillatory divergence ($R_k < -1$). In case of convergence, the Richardson extrapolation is used to define the order of accuracy p_k for the k^{th} input parameter, the extrapolated values ϕ_{ext}^{21}, the approximate relative relative error e_a^{21}, the extrapolated relative error e_{ext}^{21} and the grid convergence index GCI_{fine}^{21}:

$$p_k = \frac{ln(|\varepsilon_{k32}/\varepsilon_{k21}|)}{ln(r_k)} \tag{2.6}$$

$$\varphi_{ext}^{21} = \frac{r_k^{p_k}\varphi_1 - \varphi_2}{r_k^{p_k} - 1} \tag{2.7}$$

$$e_a^{21} = \left|\frac{\varphi_1 - \varphi_2}{\varphi_1}\right| \tag{2.8}$$

$$e_{ext}^{21} = \left|\frac{\varphi_{ext}^{21} - \varphi_1}{\varphi_{ext}^{21}}\right| \tag{2.9}$$

$$GCI_{fine}^{21} = \frac{1.25e_a^{21}}{r_k^{p_k} - 1} \tag{2.10}$$

Table 2.3 shows the number of mesh cells and the time steps used for the grid and time-step convergence study. The values of the verification parameters obtained with the ship sinkage and total resistance for grid-spacing and time-step convergence studies are indicated in Table 2.4 and Table 2.5.

Tables 2.4 and 2.5 show that small levels of uncertainty are achieved with the con-

Table 2.3.: *Values used for the fine, medium and coarse solutions in the grid and time-step convergence study*

Solution	**Grid number**	**Timestep** [s]
Fine	2 226 266	0.035
Medium	845 619	0.05
Coarse	338 212	0.07

Table 2.4.: *Grid convergence study for total resistance R_T (in newtons) and sinkage Δ_Z (in millimeters)*

Parameter	**Total resistance $\mathbf{R_T}$**	**Sinkage $\mathbf{\Delta_Z}$**
r	$\sqrt{2}$	$\sqrt{2}$
φ_1	4.698	8.415
φ_2	4.740	8.419
φ_3	5.058	8.804
R	0.130	0.010
p	5.89	13.18
φ_{ext}^{21}	4.692	8.419
e_a^{21} [%]	0.88	0.05
e_{ext}^{21} [%]	0.13	0.05
GCI_{fine}^{21} [%]	0.16	0.00

Table 2.5.: *Time step convergence study for total resistance R_T (in newtons) and sinkage Δ_Z (in millimeters)*

Parameter	**Total resistance $\mathbf{R_T}$**	**Sinkage $\mathbf{\Delta_Z}$**
r	$\sqrt{2}$	$\sqrt{2}$
φ_1	4.746	8.483
φ_2	4.740	8.419
φ_3	4.726	7.001
R	0.405	0.045
p	2.61	8.94
φ_{ext}^{21}	4.750	8.419
e_a^{21} [%]	0.12	0.75
e_{ext}^{21} [%]	0.08	0.76
GCI_{fine}^{21} [%]	0.10	0.04

trolled parameters. The predicted numerical uncertainty for resistance and sinkage are 0.16 % and 0.00 % for the finest grid solution. For the smallest time step, these values are 0.10 % and 0.04 %. The unrealistically high values obtained for the or-

der of accuracy p may indicate the the grids are not in the asymptotic range, likely because they are not systematically refined.
An intermediate grid between the medium and fine grid is chosen to maintain an affordable computational cost. That is achieved by increasing the mesh density of the medium grid inside the ship box which resulted in 1.3 M elements mesh. This grid might be too coarse to get very accurate free surface results (local quantity); however, it is fine enough to accurately calculate ship resistance, as it is a macroscopic quantity. The medium time step is used for the calculations because of the reasonably low change in resistance ($e_a^{21} = 0.12\%$) between the medium and fine solution.

2.2.3. Quasi-Newton method convergence and influence of ship sinkage

Figure 2.9 illustrates the convergence of the quasi-Newton algorithm for configuration 4 at speed $V = 0.57$ m/s and 1 DOF (ship sinkage).

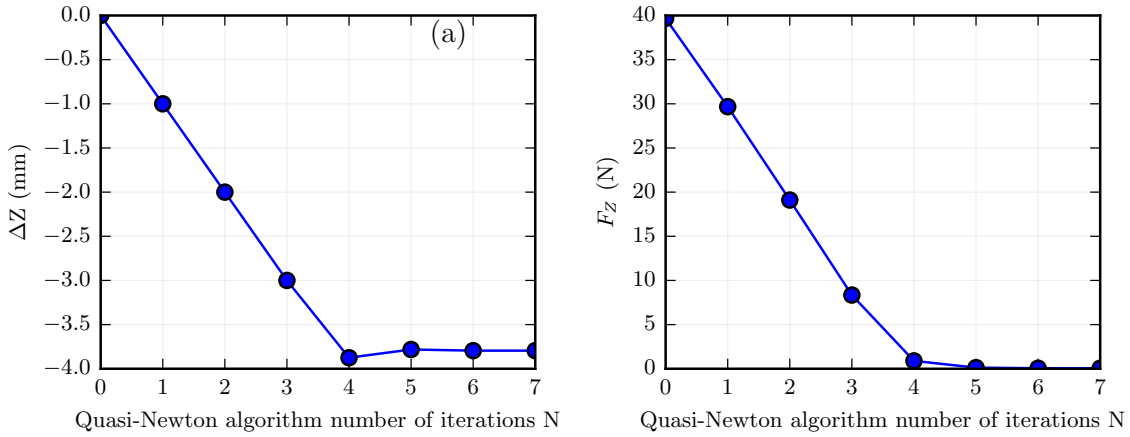

Figure 2.9.: *Quasi-Newton algorithm convergence for configuration 4 at speed $V = 0.57$ m/s : change in (a) ship sinkage ΔZ and (b) vertical forces F_Z*

In this case, the equilibrium position is reached after 5 iterations of the algorithm. The stopping criteria is set for $|F_Z| < 0.1\ N$ and in order to prevent any remeshing error (negative volume) the maximum displacement is set to 1 mm.

Figure 2.10 illustrates the convergence of the quasi-Newton algorithm for configuration 4 at speed $V = 0.57$ m/s and 2 DOF (ship sinkage and ship trim).

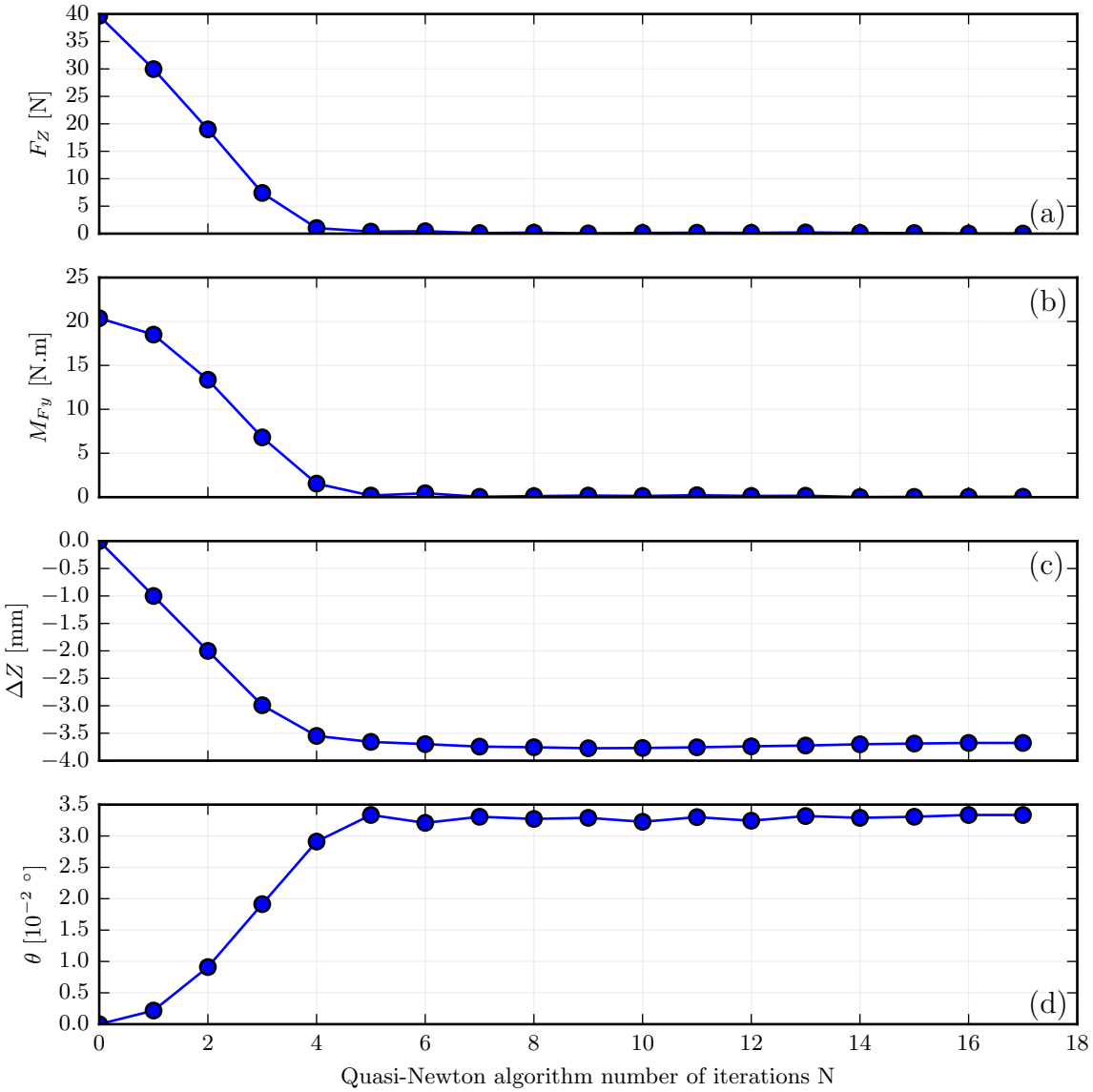

Figure 2.10.: *Quasi-Newton algorithm convergence for configuration 4 at speed* $V = 0.57$ *m/s : change in (a) vertical forces* F_Z*, (b) trim moment* M_{Fy}*, (c) ship sinkage* ΔZ *and (d) trim angle* θ

With 2 DOF, the equilibrium position is reached after 15 iterations of the algorithm. The stopping criteria is set for $|F_Z| < 0.1\ N$ and $|M_{Fy}| < 0.1\ N.m$. It can be seen that after 7 iterations, convergence is almost achieved but there are oscillations around the equilibrium position which last until the 15^{th} iteration.

Figure 2.11 shows the comparison between numerical results with 1 DOF (ship sinkage - dashed line with empty markers) and 2 DOF (ship sinkage and trim - dotted line with empty markers) for ship resistance R_T and ship sinkage Δ_Z. It also shows

the trim angle obtained with 2 DOF. Theses results are presented for configurations 3 to 5.

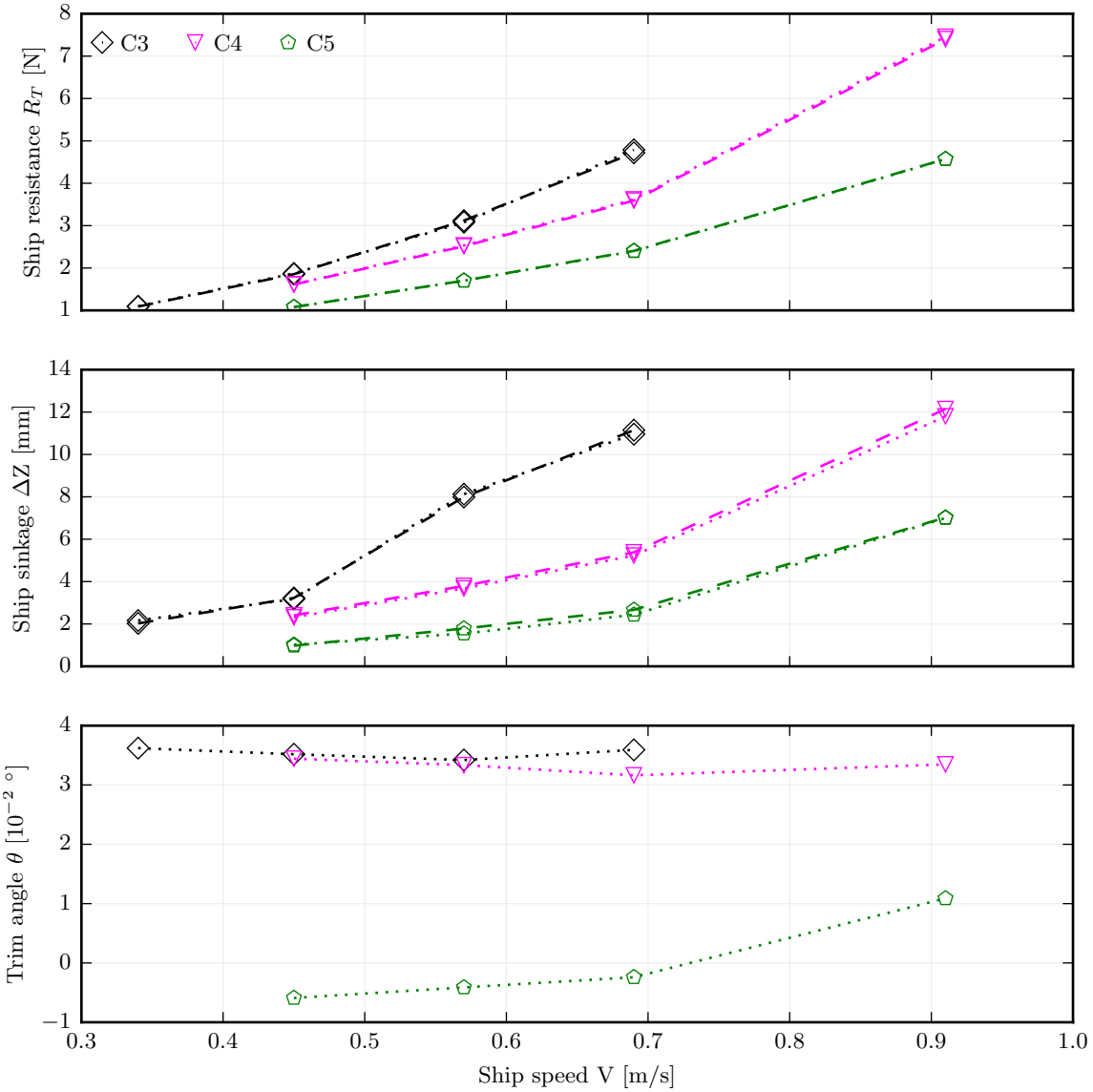

Figure 2.11.: *Comparison between numerical results with 1 DOF (ship sinkage - dashed line with empty markers) and 2 DOF (ship sinkage and trim - dotted line with empty markers) for (a) ship resistance R_T and (b) ship sinkage Δ_Z. Subplot (c) shows the trim angle θ obtained with 2 DOF.*

Figure 2.11 shows that the predicted resistance and sinkage are almost identical with 1 DOF and 2 DOF. It also shows that trim angle remains small. The low trim angles observed are explained by the fact that the speed remained at subcritical regime. At supercritical regime, trim is more significant and its impact on ship resistance cannot be neglected. Therefore, for the configurations studied in this

chapter, trim has almost no impact on ship resistance and ship sinkage is the predominant factor. Moreover, as seen with Figures 2.9 and 2.10, the Quasi-Newton method converges faster with 1 DOF. As a result, only ship sinkage is modelled for the configurations presented in Table 2.2.

2.3. Validation and numerical investigation

2.3.1. Restricted-water effect and comparison with experimental data

Figure 2.12 (a) shows the predicted resistance with sinkage as well as the experimental data for configuration 1 to 5 (as detailed in Table 2.2). Figure 2.12 (b) shows the comparison between the predicted sinkage and the experimental results for those 5 configurations.

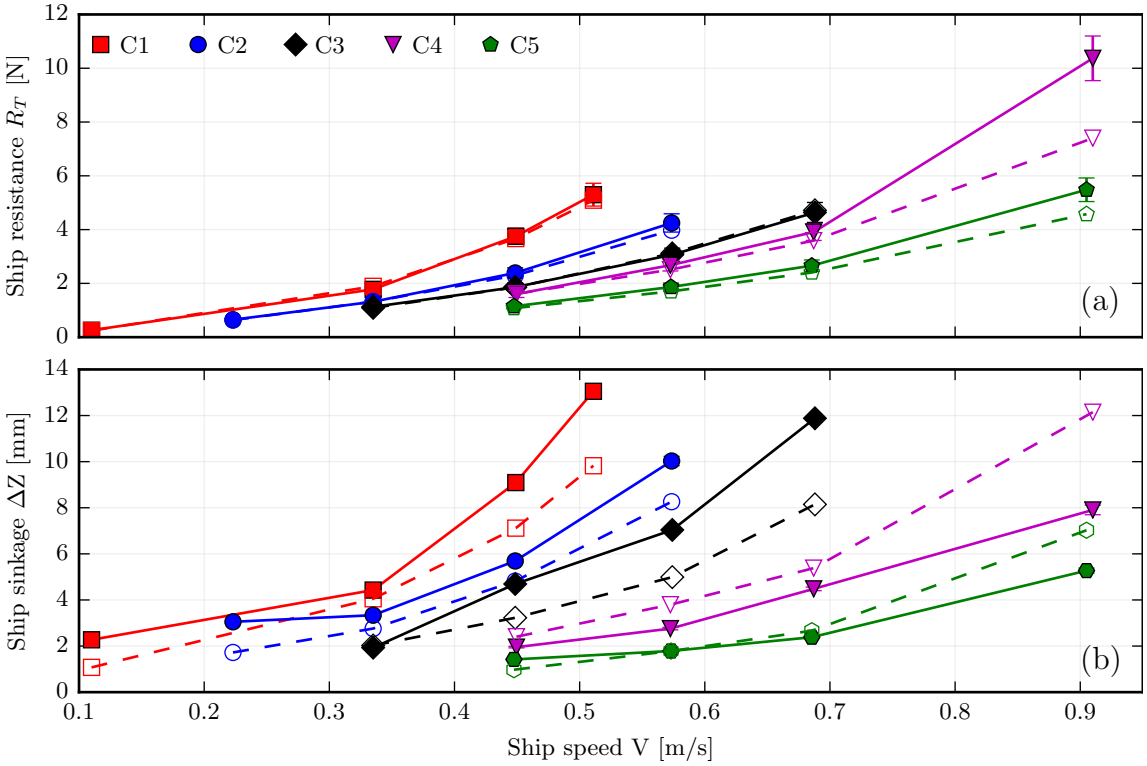

Figure 2.12.: *Restricted-water effect: comparison between numerical (dashed line with empty markers) and experimental (full line with filled markers) results for configurations 1 to 5. Change in (a) ship resistance R_T and (b) ship sinkage ΔZ against ship speed V.*

From fig. 2.12, it can be seen that as restriction increases (i.e $\frac{A_C}{A_B}$ ratio decreases - C5 to C1) ship resistance and sinkage increase. For instance, for $V = 0.44\ m/s$, ship resistance and sinkage in configuration 1 are respectively 1.9 and 4.7 times higher than in configuration 4. The comparison between numerical and experimental results shows that for ship speed up to 0.7 m/s the predicted resistance is in a good agreement with the experimental data. For ship sinkage, the numerical results show the same trend as the experiment however, there seems to be an offset. This could be explained by the potential error made when measuring the initial draft during the experiment as the uncertainty on the measure is $\pm$ 1 mm. For the ship speed of 0.9 m/s (16.2 km/h at real scale) the numerical model overestimates the sinkage and underestimate the resistance. It is possible that for this speed the model is not able to reproduce correctly the pressure field around the ship hull therefore underestimating vertical and horizontal pressure forces.

2.3.2. Influence of ship sinkage on resistance prediction error

Figure 2.13 (a) shows the predicted resistance with and without sinkage (the ship is fixed and the initial draft is kept constant) as well as the experimental data for configuration 1, 2 and 3 (as detailed in Table 2.2). Figure 2.13 (b) shows the comparison between the predicted sinkage and the experimental results for those 3 configurations. Figure 2.13 (a) shows that up to a speed of 0.33 m/s, the predicted resistance with or without sinkage does not differ much. However, above that speed, there is a gap between the measured data and predicted resistance without sinkage; while the plot of the resistance with sinkage remains very close to the experimental data (within the error bar range). This observation is sustained by the calculated prediction error: the error with sinkage is almost always smaller than that without sinkage. Additionally, for those three configurations, the maximum error is 6.3 % with sinkage whereas it reaches 18.4 % without sinkage. It can also be seen that the prediction error without sinkage increases with the speed and the restriction of the waterway, which is not the case for the predicted resistance with sinkage. Finally, the increase in ship resistance due to ship sinkage can be very significant: it reaches a maximum value of 18% for configuration 1 at 0.51 m/s. Those facts highlight the importance of taking ship sinkage into account in order to accurately predict ship resistance in restricted waterways.

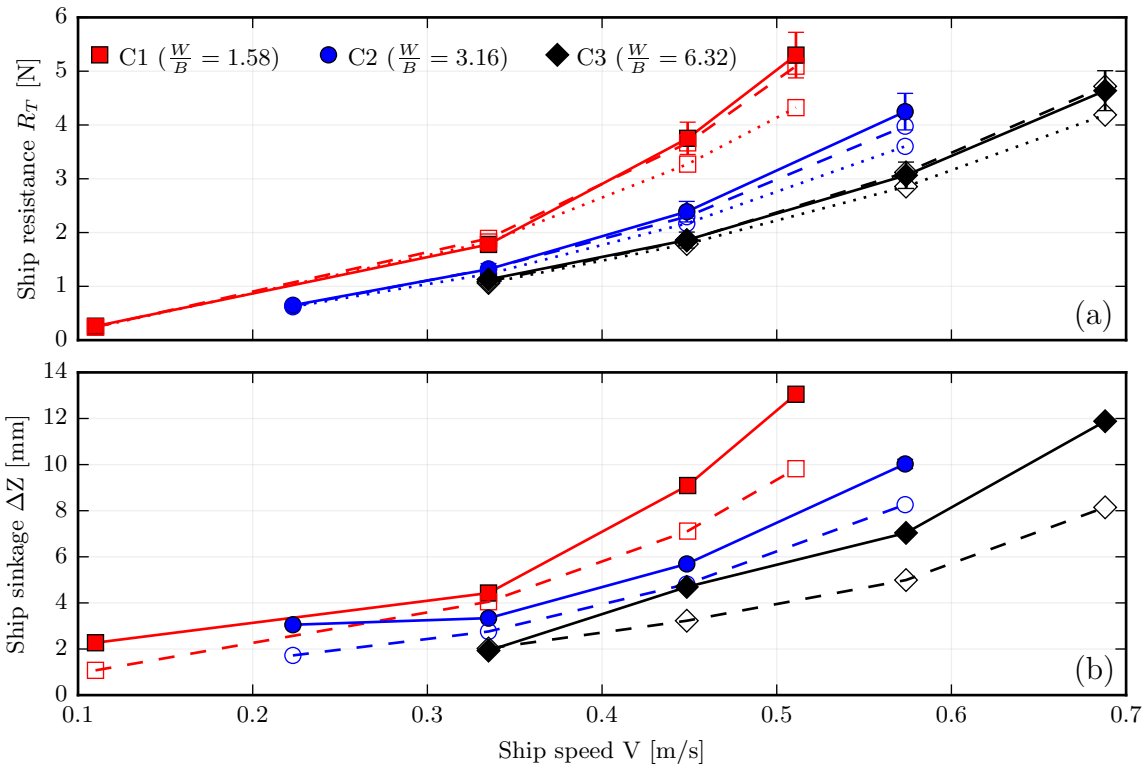

Figure 2.13.: *Comparison between the numerical results with sinkage (dashed line, empty markers) and without sinkage (dotted line, empty markers) and the experimental data (full line, filled markers) for (a) ship resistance R_T and (b) ship sinkage ΔZ for configuration 1, 2 and 3. The results are presented at model scale.*

2.3.3. Influence of restriction parameters on ship resistance

In order to study if the depth restriction (H/T) or the width restriction (W/B) has more effect on resistance, two sets of simulations were carried out. Starting from a reference configuration with a rectangular channel, in one case the water depth was decreased while the channel width remained constant, and the opposite was done in the other case. The increase in ship resistance is then compared with the reference resistance R_{Tref} calculated for the initial configuration. The use of a rectangular section ensures the similarity of the two parameters and the reference configuration was chosen so that both ratio have the same value ($H/T = W/B = 5$, equal restriction). In those simulations, the ship described in the third section was used, the draft remained constant and two speeds were tested (0.4 m/s and 0.6 m/s). The two set-ups are described in Section 2.3.3 and illustrated in Figure 2.14. For a rectangular channel, the blockage ratio can be approximated by $A_C/A_S \approx H/T \times W/B$. Therefore, in the two sets of simulation, the evolution of the blockage

ratio is the same.

Table 2.6.: *Modelled set-ups used to study the influence of restriction parameters*

Setup	**H** [m]	**W** [m]	$\frac{\mathbf{H}}{\mathbf{T}}$ [-]	$\frac{\mathbf{W}}{\mathbf{B}}$ [-]	$\frac{\mathbf{A_C}}{\mathbf{A_B}}$ [-]
Ref	0.5	2.28	5	5	25
Set-up 1	0.15-0.4	2.28	1.5-4	5	7.5-20
Set-up 2	0.5	0.68-1.82	5	1.5-4	7.5-20

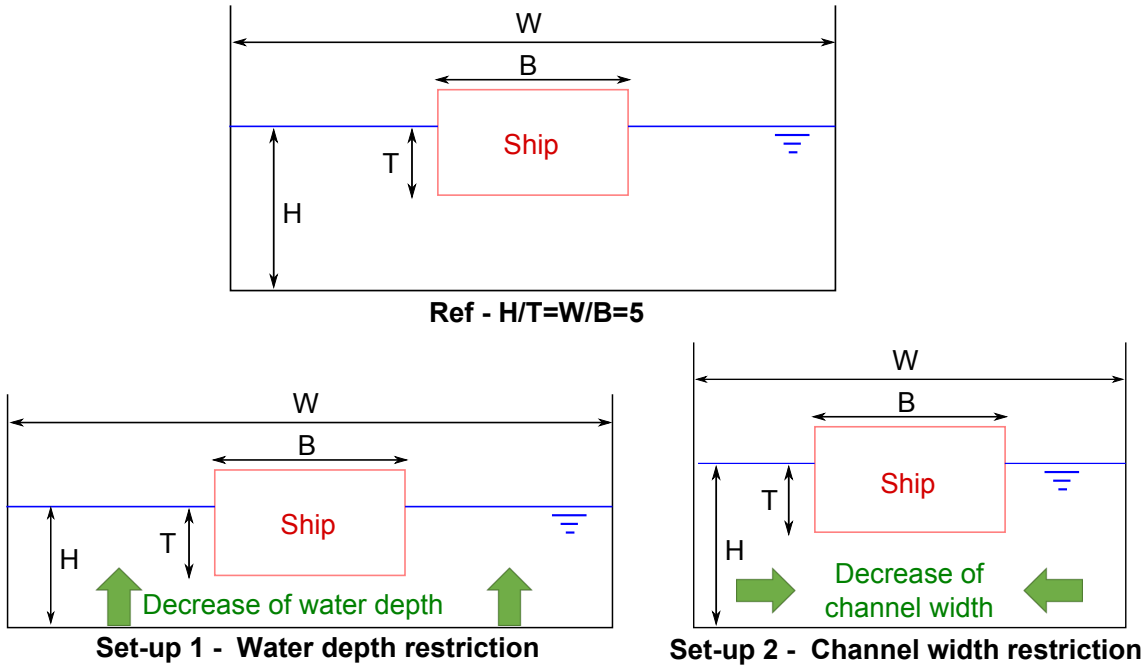

Figure 2.14.: *Illustration of the reference configuration and the two tested set-ups.*

Figure 2.15 shows the evolution of ship resistance R_T (Figure 2.15 (a)) and ship sinkage ΔZ (Figure 2.15 (b)) as well as ship resistance increase $\Delta R_T = (R_T(X) - R_{Tref})/R_{Tref}$ (Figure 2.15 (c)) due to depth restriction in set-up 1 and channel width restriction in set-up 2. Figure 2.15 (a) and (b) show that for a given speed, the resistance and sinkage start to increase for values of the restriction parameter below 4, which is in agreement with the findings of the ITTC (1987). Additionally, significant differences in ship resistance and sinkage begin to appear between the case of water depth and channel width restriction when the restriction parameter is below 3. Figure 2.15 (c) shows that water depth restriction has more influence on ship resistance increase than channel width restriction. At a speed of 0.6 m/s, the ship resistance increase is 84 % for $H/T = 1.5$ and 39 % for $W/B = 1.5$. This can

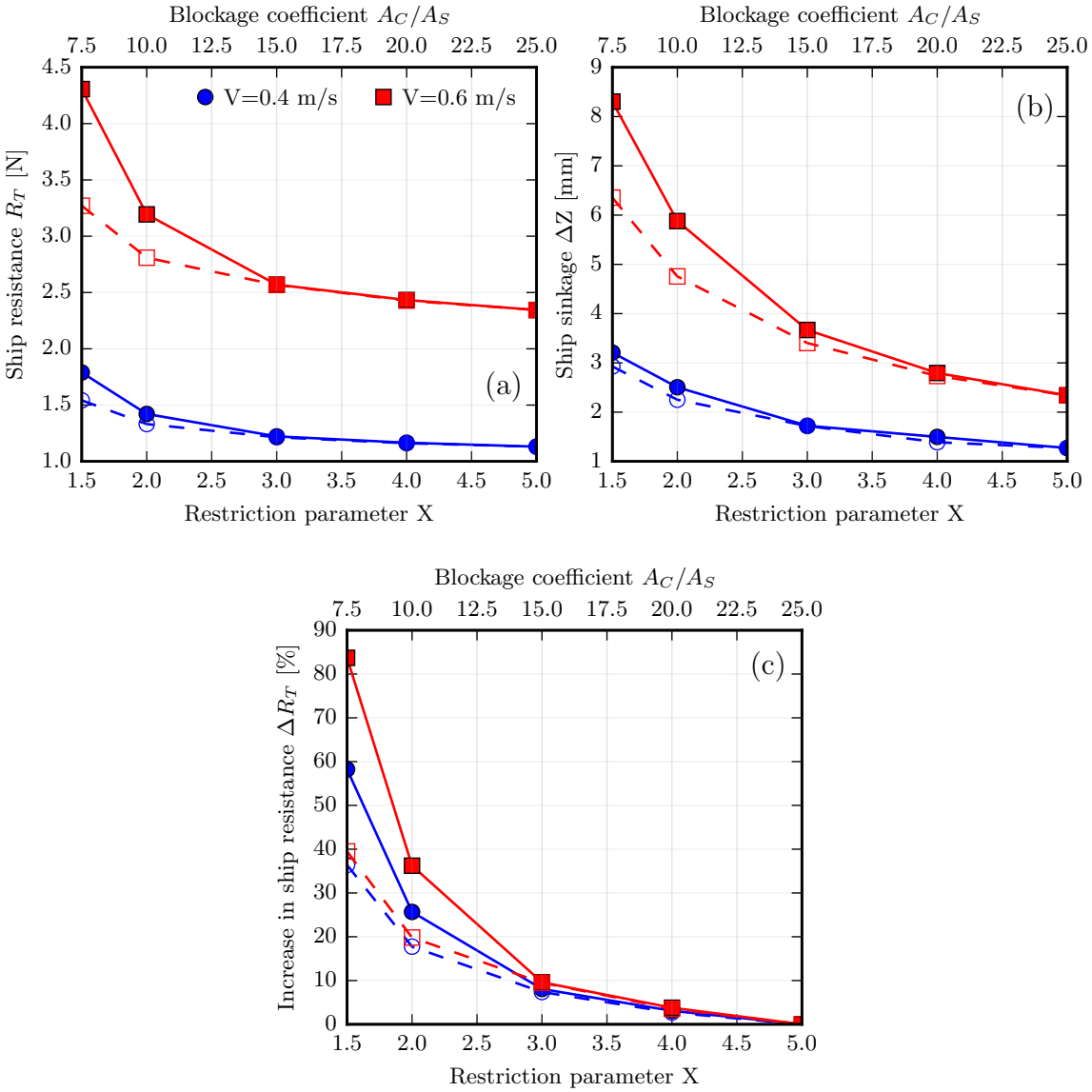

Figure 2.15.: *Evolution of (a) ship resistance R_T, (b) ship sinkage ΔZ and (c) ship resistance increase ΔR_T versus restriction parameter X and blockage coefficient A_C/A_S. $X = H/T$ for set-up 1 (full line, filled markers) and $X = W/B$ for set-up 2 (dashed line, empty markers)*

be explained by the fact that ship sinkage is less sensitive to vertical restriction than horizontal restriction. Under the hull, the flow velocity increase and the pressure drop under will be less impacted by a channel width decrease than a water depth decrease. Those results show that to characterize the effect of channel restriction on ship resistance, the contributions of channel width and water depth restriction must be separated. Therefore, a single parameter such as the blockage coefficient A_C/A_S, often used to quantify channel restriction in empirical models, is not suitable and

lacks details. Figure 2.15 (a) shows that for any value of $A_C/A_S < 15$, two distinct values of resistance are obtained depending on the nature of the restriction.

2.4. Assessment of empirical models

Empirical models can be useful for designers to help them in the conception of an optimized inland vessel. To evaluate the accuracy of such methods, various models are compared to the numerical and experimental results. The main idea behind the developed empirical models is that the components of ship resistance in restricted water at speed V_0 can be determined from open water formula (Holtrop (1984)) applied with corrected speeds. Schlichting (1934) and Karpov (1946) used two speed corrections to estimate the effect of shallow water. Landweber (1939) suggested an extension of Schlichting's method to width restriction by using the hydraulic radius instead of water depth to calculate the speed corrections. Artjuskov (1968) added a third speed correction to Karpov's method to include restricted width effect into shallow water resistance prediction. More recently, Geerts et al. (2010) devised a new method, inspired by that of Schlichting and Landweber, in which they replaced the critical velocity in shallow water by Schijf limiting speed. They also used the value of the return flow velocity, determined by using a one dimensional approach, as the second velocity correction.

Empirical prediction models for ship resistance

Holtrop and Mennen method for open water resistance

For their method, Holtrop and Mennen included physical aspects in their formula but used experimental data for determining the coefficients. For that, they used test results from 334 model testings including tankers, cargo ships, trawlers, ferries, etc. In their method, the resistance is divided into viscous and wave resistance. The viscous resistance is calculated with the following formula:

$$C_V = (1 + k)C_F \tag{2.11}$$

where k is the form factor.

C_F is obtained by the ITTC-57 formula:

$$C_F = \frac{0.075}{(log_{10}(Re) - 2)^2} \tag{2.12}$$

The wave resistance is given by the following formula:

$$R_W = c_1 c_2 c_5 \nabla \rho g \; exp(m_1 (Fr)^d + m_2 cos(\lambda (Fr)^{-2}) \tag{2.13}$$

where c_1, c_2, c_5, m_1 and m_2 are coefficient which are functions of the form parameters of the hull and the ship generated wavelength λ. More details about the values of those coefficients can be found in Holtrop and Mennen (1982).

The total resistance is then given by:

$$R_T = R_V + R_W + R_{APP} + R_B + R_{TR} + R_A \tag{2.14}$$

where R_{APP} is the resistance of appendages, R_B is the additional resistance pressure of bulbous bow near the water surface, R_{TR} is the additional pressure resistance of immersed transom stern and R_A is the model-ship correlation. More detailed information about those additional resistance can also be found in Holtrop and Mennen (1982).

Holtrop (1988) modified the Holtrop and Mennen method by including a form factor depending on the ship speed, revising the wave resistance formula and adding resistance due to incoming waves, head winds and shallow water corrections. However, this improvement of their method is seldom used.

Schlichting correction method for shallow water effects

Schlichting (1934) developed a method for calculating ship total resistance in shallow water for sub-critical speeds. For that, he supposed that the total resistance in shallow water was equal to that of total resistance in deep water plus the change in frictional resistance and wave resistance induced by shallow water. Let V_∞, $R_{W\infty}$ and $R_{F\infty}$ respectively be the speed, wave resistance and friction resistance in deep water. At this speed, the ship transverse waves have a wavelength λ_0 given by:

$$V_\infty = \sqrt{\frac{g\lambda_0}{2\pi}} \tag{2.15}$$

At a water depth H, the same wave length would be obtained at a lower speed V_I given by:

$$V_I = \sqrt{\frac{g\lambda_0}{2\pi} tanh \frac{2\pi H}{\lambda_0}} \tag{2.16}$$

Schlichting assumed that the wave resistance at speed V_I in shallow water would then be the same as wave resistance at speed V_∞ in deep water. The total resistance R_{T-V_I} at speed V_I is then equal to:

$$R_{T-V_I} = R_{W\infty} + R_{F_h} \tag{2.17}$$

where $R_{W\infty}$ is the wave-making resistance in deep water and R_{F_h} the frictional resistance in deep water at speed V_I.

However, as stated before, in shallow water, not only the wave resistance is increased, but also the frictional resistance. Schlichting also accounted for this increase in resistance by adding a supplementary speed reduction δV_P based on model tests in deep and shallow water. His conclusion from those tests was that this speed loss was mainly dependent on the ratio $\frac{\sqrt{A_M}}{h}$ where A_M is the maximum cross-sectional area of the hull and h is the water depth. Figure 2.16 shows the total speed loss $\delta V = \delta C + \delta V_P$ as a percentage of the deep-water speed. Figure 2.17 schematically illustrates how the ship total resistance can be calculated using Schlichting method.

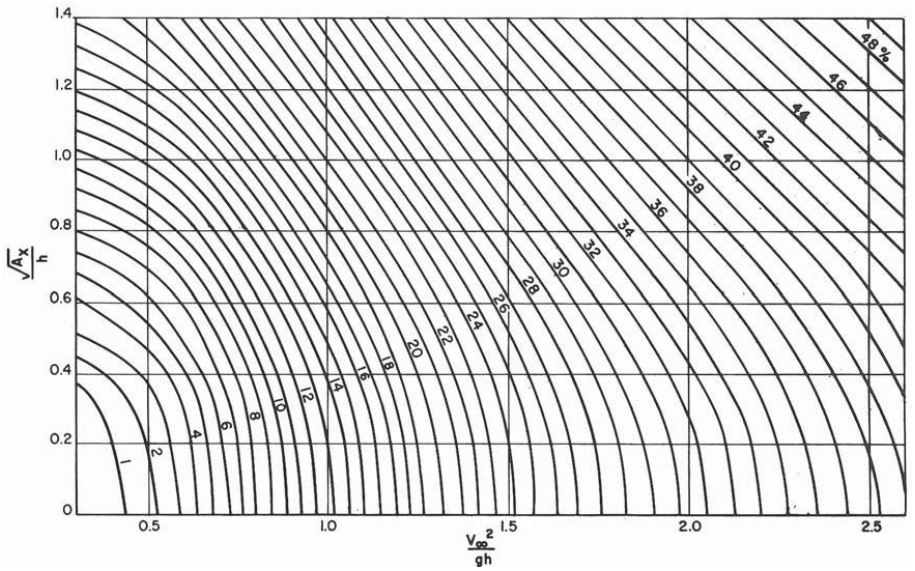

Figure 2.16.: *Chart for calculating reduction in speed in shallow water.*
Source: *Larsson and Raven (2010), p.46*

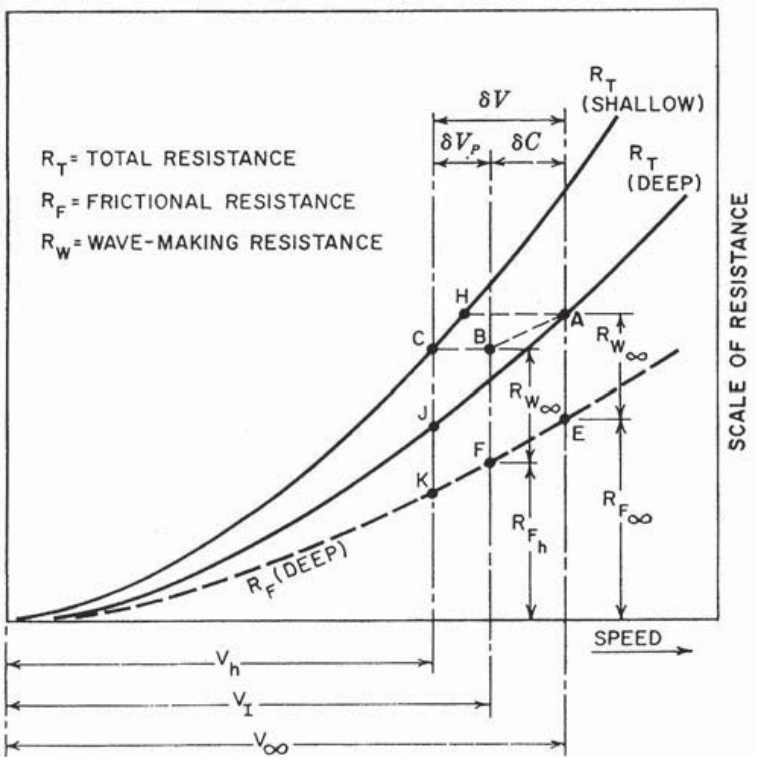

Figure 2.17.: *Determination of shallow water resistance by Schlichting method.*
Source: *Larsson and Raven (2010), p.44*

It should be noted that several objections can be made to Schlichting method:

- assuming that the wave-making resistance in deep and shallow water is the same as long as the wavelength has the same value is not totally true as diverging waves and the amplification of wave amplitude due to the bottom proximity are neglected;
- the viscous resistance is dependant on the ship hull form, which is not taken into account in this method.

Landweber correction method for restricted water effect

Landweber (1939) developed a method similar to that of Schlichting (1934). For moderate channel effects, it is possible to assume that Schlichting's correction of the wave-making resistance still avails. However, the correction for viscous resistance has to be modified. Landweber searched for a similar parameter to that used by

Schlichting ($\frac{\sqrt{A_M}}{h}$) and used the hydraulic radius R_H:

$$R_H = \frac{\text{area of channel cross section}}{\text{wetted perimeter}} \tag{2.18}$$

Using that parameter, he found a curve linking $\frac{V_H}{V_I}$ and $\frac{\sqrt{A_X}}{R_H}$ shown in Figure 2.18.

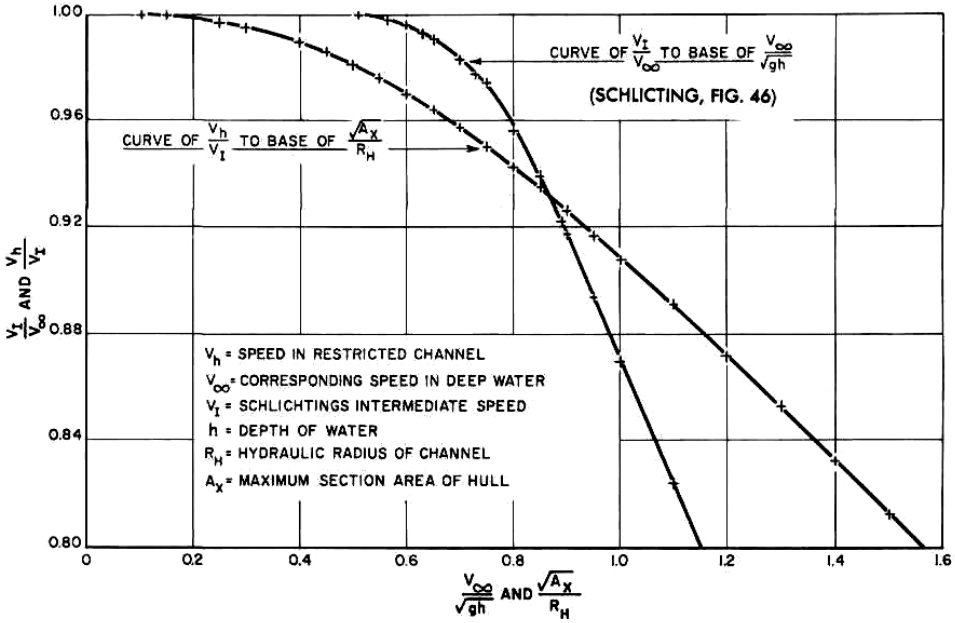

Figure 2.18.: *Curves of velocity ratio for calculating resistance in restricted channels.*
Source: *Larsson and Raven (2010)*

However, for more severe channel effects, Schlichting's correction of the wave-making resistance is no longer available and therefore, Landweber's method can not be used.

Karpov's and Artjuskov's method

Karpov (1946) developed a method to calculate resistance in shallow water. He used two effective speeds V_1 and V_2 instead of the service speed V to calculate the total resistance in a waterway depth h:

$$R_T = \frac{1}{2}\rho S((C_F + C_a)V_1^2 + C_R V_2^2) \tag{2.19}$$

where C_F is calculated with Equation (2.12) for Reynolds number based on speed V_1, C_R is calculated with Holtrop and Mennen's method (deep-water) at Froude number based on speed V_2 and C_a is the roughness allowance.

The effective speed V_1 and V_2 are given by:

$$V_i = \frac{V_i}{\alpha_i}, i = 1, 2 \tag{2.20}$$

where $\alpha_i, i = 1, 2$ are speed correction coefficients determined from Karpov's graph and are function of $\frac{H}{T}$ ratio and Froude number F_r.

Artjuskov (1968) used Karpov's method and included correction for limited waterway width. He kept Karpov's wave-making resistance correction and added correction for the supplementary friction resistance. The total resistance is calculated with the following formula:

$$R_T = \frac{1}{2}\rho S((C_F + C_a)V_1^2 + (C_R(\frac{V}{V'})^2 + \Delta C_R)V_2^2) \tag{2.21}$$

where C_R is calculated for unrestricted water depth for the speed V_2 defined by Karpov and $\frac{V}{V'}$ and ΔC_R are respectively the change in speed and in residual resistance due to waterway restriction whose values given by Artjuskov's tables as a function of $\frac{W}{B}$ and $\frac{H}{T}$ ratio.

Karpov's graph and Artjuskov's tables can be found in Luthra et al. (1982). This method was used by Georgakaki and Sorenson (2004) in order to evaluate energy consumption for different vessels in various waterway width and their results were on average on good terms with experimental data.

Geerts' method

Geerts et al. (2010) developped a method taking into account the effects of restricted water depth and width. Their method is similar to that of Schlichting (1934) and Landweber (1939). They use Holtrop and Mennen's method (Holtrop and Mennen, 1982; Holtrop, 1984) as a base and corrected speeds in order to calculate the total resistance.

In order to calculate the wave making resistance in restricted water depth and width, they use the following relation between velocity in deep water V_∞ and ve-

locity in restricted water V_R:

$$\frac{V_R}{V_\infty} = \sqrt{tanh((\frac{V_{CR}}{V_\infty})^2)} \tag{2.22}$$

where V_{CR} is the critical velocity in restricted waters, also known as Schijf's limiting speed, and is given by Briggs et al. (2009):

$$V_{CR} = \sqrt{gh}(2sin\frac{Arcsin(1-m)}{3})^{3/2} \tag{2.23}$$

where m is the blockage coefficient.

For the viscous resistance, a 1D equation (Dand and Ferguson, 1973) is used in order to evaluate the speed of the return flow ΔV in function of the ship's forward speed V:

$$\frac{1}{2}F_{nh}^2(\frac{V+\Delta V}{V})^3 - (\frac{1}{2}F_{nh}^2 + 1 - m)\frac{V+\Delta V}{V} + 1 = 0 \tag{2.24}$$

2.4.1. Results extrapolation to real scale

In order to compare the numerical and experimental results (at model scale) with the empirical models (designed for full-scale application), the results at model scale are extrapolated to full-scale with the ITTC78 method (ITTC, 1978) widely used by naval architects and towing tanks.

ITTC-78 extrapolation method

This method is based on the form factor approach where the ship total resistance is decomposed in a viscous resistance including the form effect on friction and pressure, and a wave resistance:

$$\begin{aligned} C_T &= (1+k)C_F + C_W \\ &= C_V + C_W \end{aligned} \tag{2.25}$$

where $C_V = (1+k)C_F$ and $(1+k)$ is a form factor which depends on hull form, C_F is the skin friction coefficient based on flat plate results, C_V is a viscous coefficient taking into account skin friction and viscous pressure resistance and C_W is the wave resistance coefficient.

The procedure to extrapolate the model scale results to full scale is as follows:

1. The model skin friction coefficient C_{FM} is calculated according to the ITTC-57 formula:
$$C_{FM} = \frac{0.075}{(log_{10}Rn_M - 2)^2} \tag{2.26}$$
where Rn_M is the model Reynolds number.
2. The wave resistance coefficient of the model C_{WM} is computed according to:
$$C_{WM} = C_{TM} - (1 + k)C_{FM} \tag{2.27}$$
where C_{TM} is the total resistance coefficient of the model.
3. The wave resistance coefficient for the ship at full scale C_{WS} is assumed to be equal to that of the model C_{WM} based on Froude's law stating that wave resistance only depends on Froude number F_n:
$$C_{WM} = C_{WS} \tag{2.28}$$
4. The friction coefficient of the full scale ship C_{FS} is calculated:
$$C_{FS} = \frac{0.075}{(log_{10}Rn_S - 2)^2} \tag{2.29}$$
5. The roughness allowance ΔC_f is computed according to Bowden formula:
$$\Delta C_f = \left(105\left(\frac{k_{MAA}}{L}\right)^{\frac{1}{3}} - 0.64\right) \cdot 10^{-3} \tag{2.30}$$
6. Finally, the total resistance coefficient at full scale C_{TS} is calculated as:
$$C_{TS} = (1 + k) \cdot C_{FS} + C_{WS} + \Delta CF \tag{2.31}$$

This method is schematically illustrated in Figure 2.19.

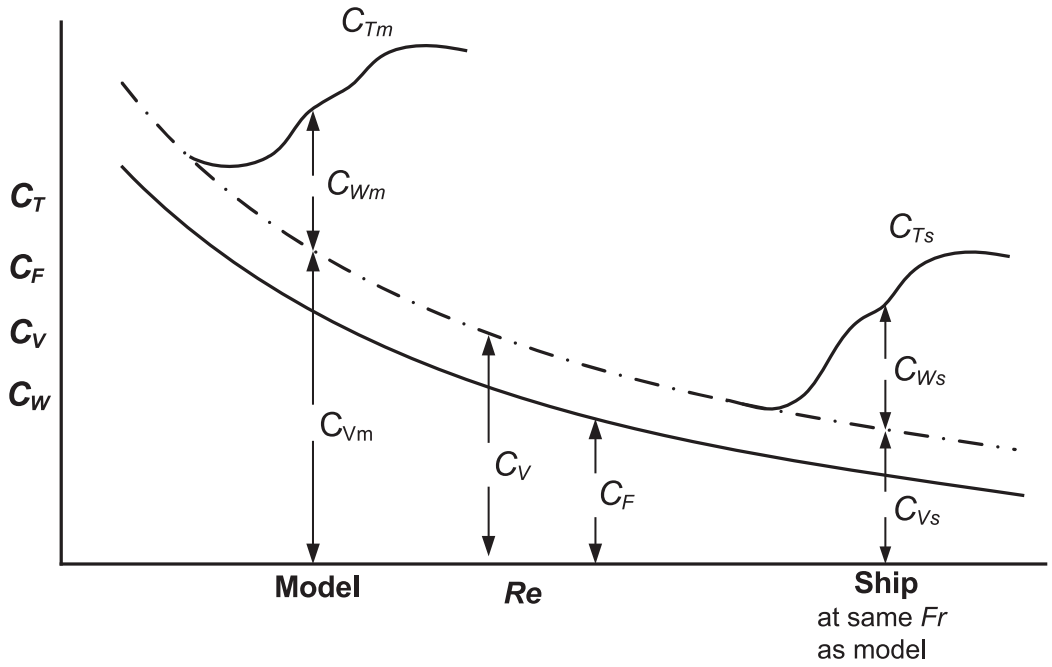

Figure 2.19.: *Graphical representation of model-ship extrapolation method based on form factor approach.*
Source: *Molland et al. (2011)*

Form factor derivation

As shown in Equation (2.31), the form factor needs to be determined before extrapolating the results to full scale. ITTC (Conference, 2008) recommends Prohaska's method (Prohaska, 1966) for experimental evaluation of the form factor. This method is based on the assumption that the wave resistance coefficient is proportional to the Froude number to the fourth power. Equation (2.25) can then be written:

$$C_T = (1 + k) \cdot C_F + AFr^4 \tag{2.32}$$

where A is a constant.
Equation (2.32) divided by C_F yields:

$$\frac{C_T}{C_F} = (1 + k) + A\frac{Fr^4}{C_F} \tag{2.33}$$

which is a straight line as illustrated in Figure 2.20.

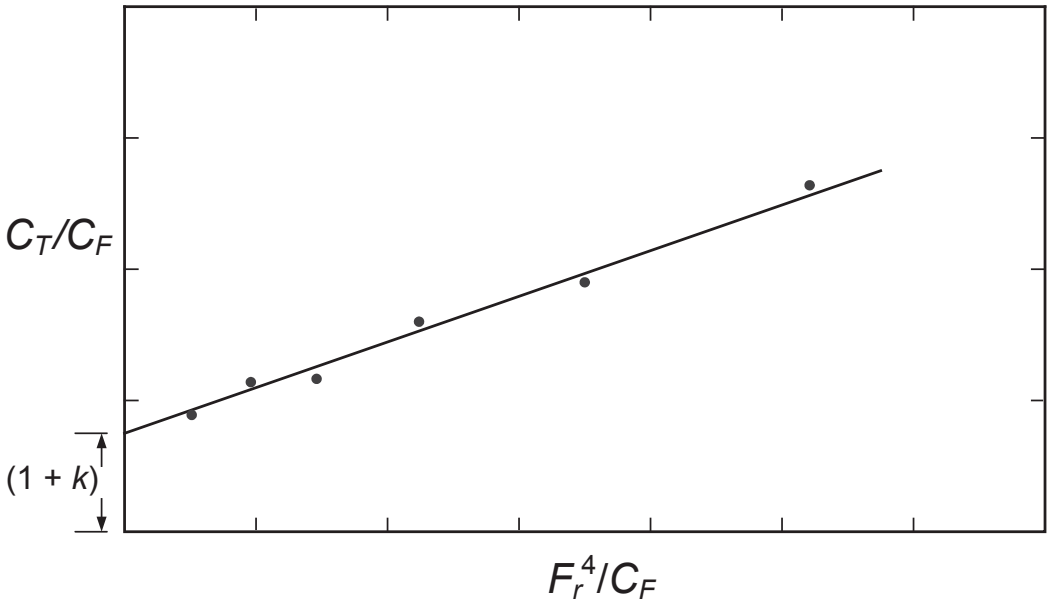

Figure 2.20.: *Illustration of Prohoaska's method for form factor derivation*
Source: *Molland et al. (2011)*

Thus, if the assumption on the wave resistance is verified, the measurement points should plot a straight line which intercepts $(1 + k)$ on the vertical axis. Molland et al. (2011) argued that for full form vessel, the measurement points might not fall on a straight line and recommend to use a power of Fr between 4 and 6. Thus, for each configuration indicated in Table 2.2, this method was applied for a power of Fr between 4 and 6, and the form factor was obtained from the power giving the best coefficient of determination R^2. Figure 2.21 shows the results obtained with Prohaska's method for configuration Table 2.7 and tab sums up the form factors obtained for each configuration listed in Table 2.2.

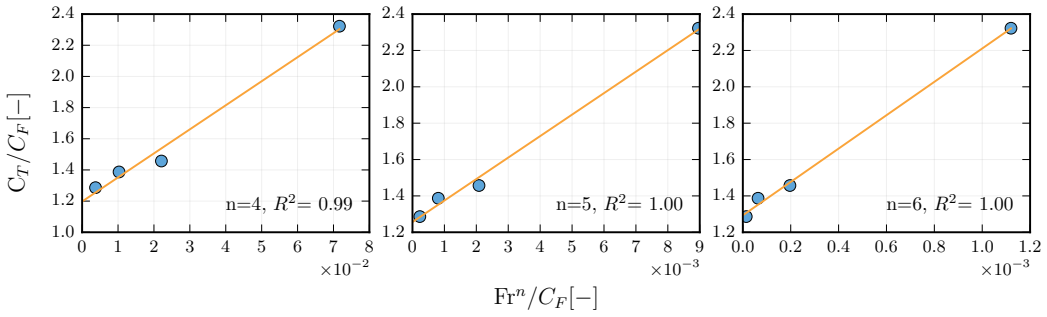

Figure 2.21.: *Form factor determination with Prohaska's method for configuration 4.*

Table 2.7.: *Form factors* $(1+k)$ *and coefficients of determination* R^2 *obtained for each tested configurations.*

Conf.	**Form factor** $(\mathbf{1+k})$ [-]	**Coefficient of determination** $\mathbf{R^2}$ [-]
C1	2.46	0.93
C2	1.79	0.98
C3	1.50	0.96
C4	1.29	1.00
C5	1.18	1.00

Table 2.7 shows that the form factor $(1+k)$ increases with the restriction of the waterway (i.e $\frac{A_C}{A_B}$ ratio decreases - C5 to C1). Those results are in agreement with the findings of Millward (1989) and Raven (2012) stating that form factor increases as water depth decreases.

2.4.2. Comparison between empirical formula and numerical results

In order to compare the numerical and experimental results (at model scale) with the empirical models (designed for full-scale application), the results at model scale were extrapolated to full-scale with the ITTC78 method (ITTC, 1978) described in Section 2.4.1. It should be noted that the scaling process from model scale to full scale being non-linear, the difference between experimental and numerical data is increased as well as the error bar range. Figure 2.22 shows the comparison of experimental, numerical and empirical results for configuration 1 to 4. It is worth mentioning that Karpov & Artjushkov's method (Karpov, 1946; Artjuskov, 1968) could not be applied for configuration 1 as this configuration is outside of the method range of validity. Similarly, Holtrop formula applies to loaded ships therefore, the numerical results for configuration 5 (empty ship) could not be compared with the empirical models.

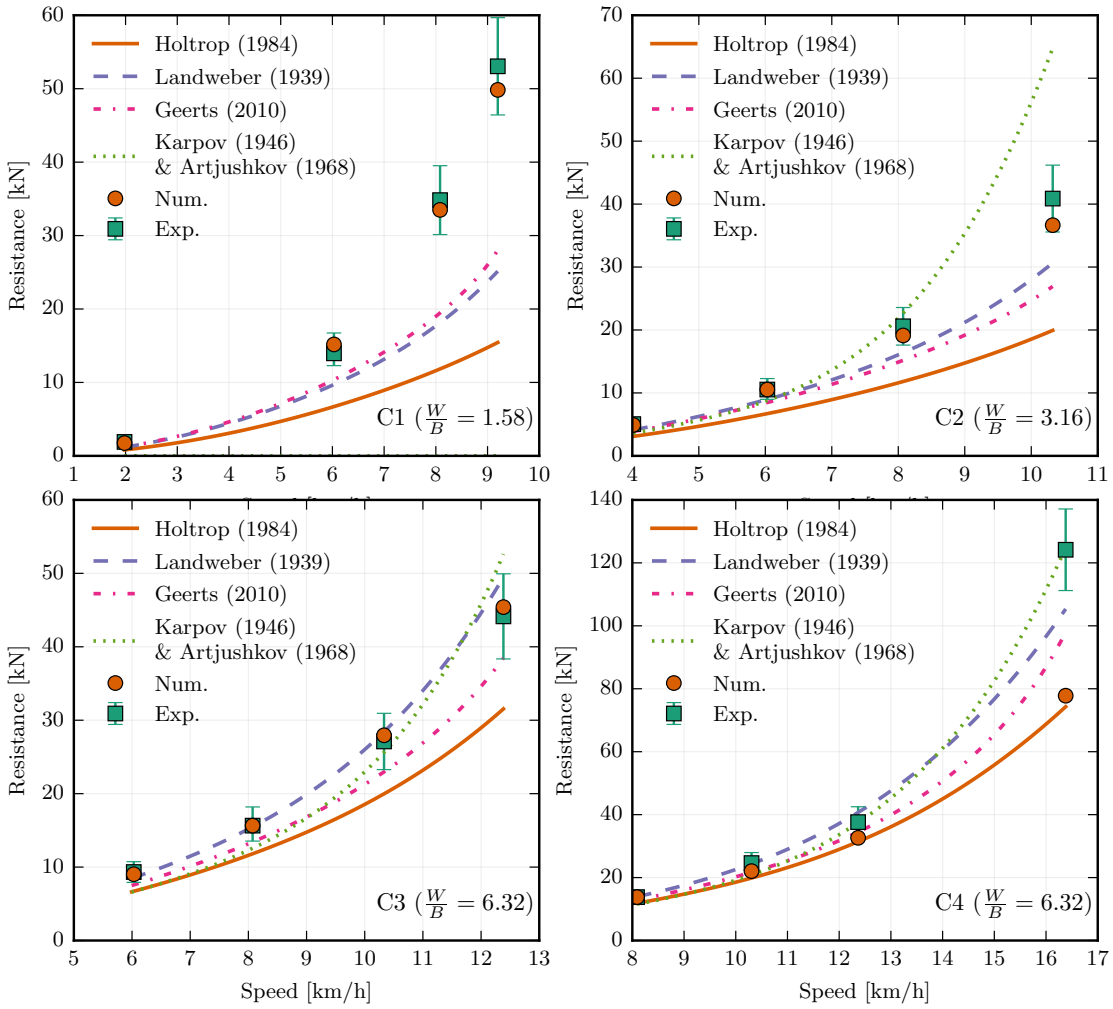

Figure 2.22.: *Comparison between experimental (Exp.), numerical (Num.) and empirical model results for configuration 1 to 4. Holtrop formula corresponds to ship resistance in open water. The results are presented at full scale.*

The comparison between the open water ship resistance Holtrop (1984) and experimental data illustrates the resistance increase due to navigation in restricted waters. For instance, to maintain the ship velocity at 9 km/h in configuration 1, it requires 3.4 times more power than in open sea. The comparison with experimental data shows that the empirical models do not accurately predict ship resistance for the most restricted configurations (configuration 1 and 2). They underestimate the resistance except for Karpov & Artjushkov's method in configuration 2 which overestimates it. For the less restricted configuration (configurations 3 and 4) the empirical models are in better agreement with the experimental data and Landweber and Karpov & Artjushkov's method are in better agreement than Geerts' method.

Altogether, based on the results presented for those four configurations, the correction of restricted water effect on resistance given by these models seems to give reasonable results for low lateral restriction but they might perform poorly when lateral restriction is severe. These discrepancies can be explained by the fact that the tested empirical methods were derived from results obtained with sea-going ships which have block coefficients smaller than the inland vessels used in this study. In his paper, Raven (2012) concluded that the most used empirical methods to predict shallow water resistance have very weak empirical and theoretical basis. For instance, he argued that Schilichting's method (on which Landweber's method tested here is based on) was derived from a very narrow selection of 3 warship cruisers not representative of modern merchant ships. He recommends the development of new prediction methods correcting each component of the total resistance separately. This point is one of the aims of the Top Ships project currently ongoing (Rotteveel et al., 2014). Finally, Figure 2.22 shows that the numerical model gives more accurate prediction of ship resistance than the empirical models except for the speed of 16 km/h in configuration C4.

2.5. Conclusion

The numerical model presented in this chapter allows to calculate ship resistance in restricted waterways by taking ship sinkage into account. The use of a Newtonian method in order to find the equilibrium position allows to skip the transient state. The sensitivity study conducted in section 2.2.3 has shown that for the configurations studied in this chapter, trim has almost no impact on ship resistance and ship sinkage is the predominant factor. The comparison between experimental data and numerical results has shown that the predicted resistance and sinkage are in close agreement with measurement for velocities below 0.7 m/s but discrepancies appeared for the highest tested velocity (0.9 m/s). Taking ship sinkage into account allowed to significantly reduce the prediction error. The model was used to study the influence of channel width and water depth restriction. The results showed that in case of water depth restriction, ship sinkage is more significant and results in higher ship resistance increase. Finally, the comparison between experimental data and various empirical models shows that those models can be used to calculate an approximate range of variation for ship resistance in shallow water with

low lateral restriction. However, when width restriction is severe, those models might perform poorly and underestimate ship resistance. The discrepancies found for the highest tested velocity (0.9 m/s) will be investigated more deeply in chapter 5. Overall, the numerical model presented in this chapter can provide a better understanding of hydrodynamics phenomena in confined waters.

CHAPTER 3

Further investigation for speed at critical regime

In 2015, GIS HED[2] (Groupement d'Intérêt Scientifique Hydraulique pour l'Environnement et le Développement Durable) funded a project (Caplier et al., 2015) whose objective was to compare shallow water ship waves experimental results from Pprime Institute [1] and numerical prediction of ship waves from the model used in this PhD. Previous studies (e.g. Ji et al. (2012)) have shown that numerical models can accurately reproduce ship generated waves in lowly confined waters and at subcricital regime. Therefore this project focused on highly restricted water depth and critical regime (regime between the subcritical and supercritical speed). This chapter gives a description of the experiments carried out in Pprime institute towing tank and presents the project results. The comparison between experimental and numerical results allows to evaluate the ability of the numerical model to reproduce the flow and waves generated by a ship navigating in shallow water for speeds greater than subcritical speed. Therefore, this study also allows to investigate the discrepancies for ship resistance prediction at high speed observed in chapter 3.

[1] Université de Poitiers, CNRS, ISAE ENSMA

3.1. Pprime towing tank experiments

3.1.1. Towing tank and model ship hulls

Pprime towing tank is 20 m long, 1.5 m wide and 1.2 m deep. The bottom part of the channel cross section has a trapezoidal shape and a fake bottom is set-up in the channel to run shallow water tests. The basin is equipped with a carriage running on two rails and towing the model ship. Measuring devices are installed on the towing carriage and its speed is controlled by computer. The measuring area where the ship waves are steady is located between 5 m and 10 m from the beginning of the basin (for the speed range allowed by the towing carriage - 0 to 2.35 m/s). Figure 3.1 and Figure 3.2 show an overview of Pprime Institute towing tank and the cross section of the basin.

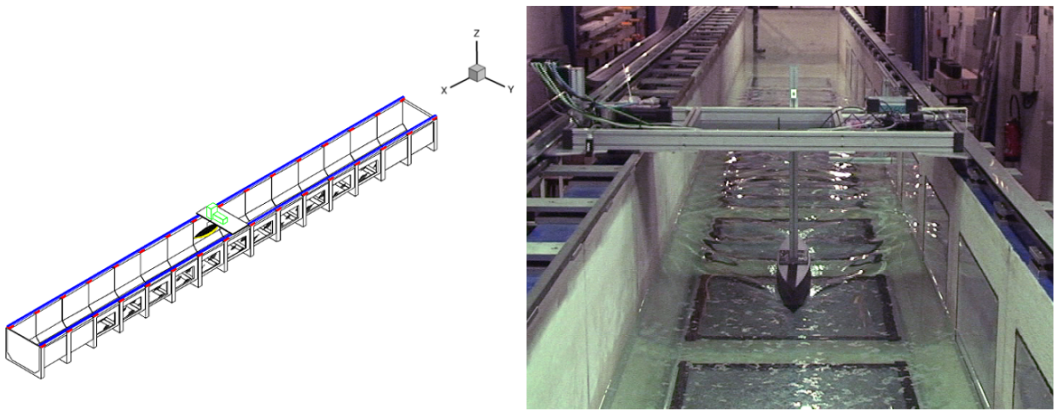

Figure 3.1.: *Overview of Pprime Institute towing tank*
Source: *Caplier et al. (2015)*

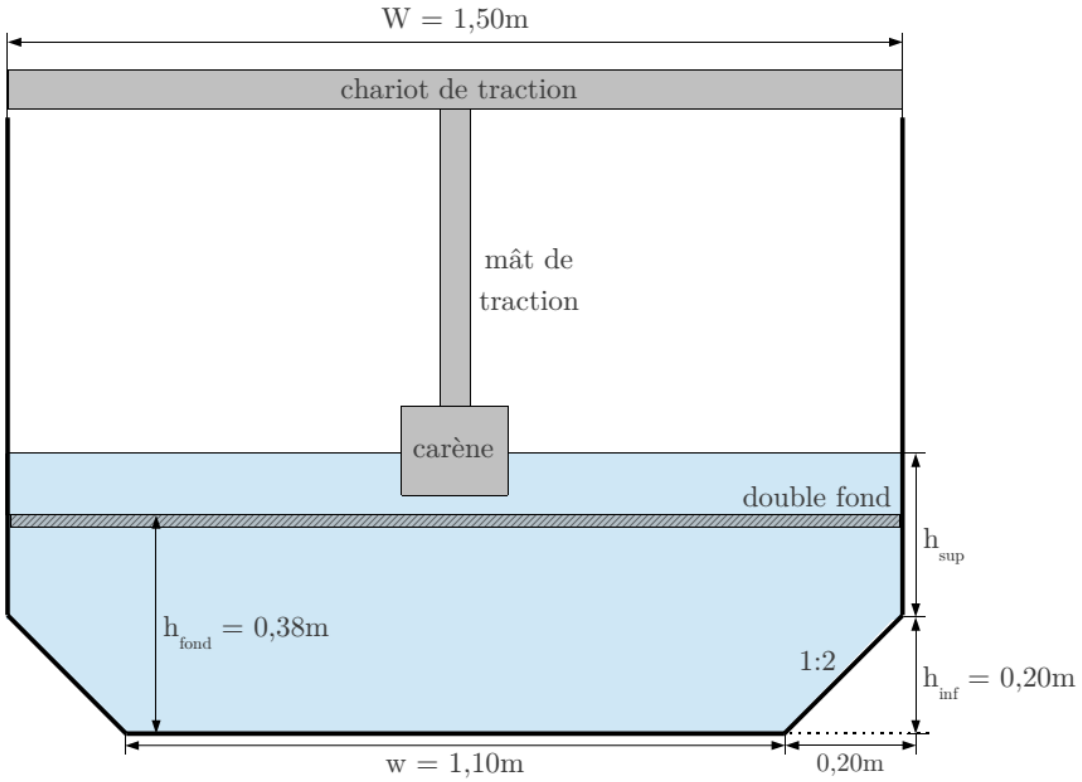

Figure 3.2.: *Diagram of the towing tank cross section*
Source: *Caplier et al. (2015)*

Ship hulls forms have a significant influence on the waves they generate and on the ship resistance. Inland vessels usually have a higher block coefficient than maritime ships. For the comparison between numerical and experimental results, two simplified hull forms were chosen. They are based on a modified Wigley hull with rectangular section and two different block coefficients corresponding to a maritime ship and an inland vessel. The form of those two hulls is governed by the following mathematical expressions:

$$y_{CWn2} = \frac{B}{2}\left[1 - \left(\frac{2x}{L}\right)^2\right] \tag{3.1}$$

$$y_{CWn8} = \frac{B}{2}\left[1 - \left(\frac{2x}{L}\right)^8\right] \tag{3.2}$$

They are referred to as CWn2 and CWn8, the number indicating the value of the n exponent. Their corresponding block coefficient is $Cb = 0.67$ for the maritime hull CWn2 and $Cb = 0.89$ for the inland ship hull CWn8. The length of both hulls is

$L = 1.20\ m$, their width is $B = 0.18\ m$ and their height is $Ht = 0.15\ m$. Figure 3.3 shows a picture of the model ship hulls.

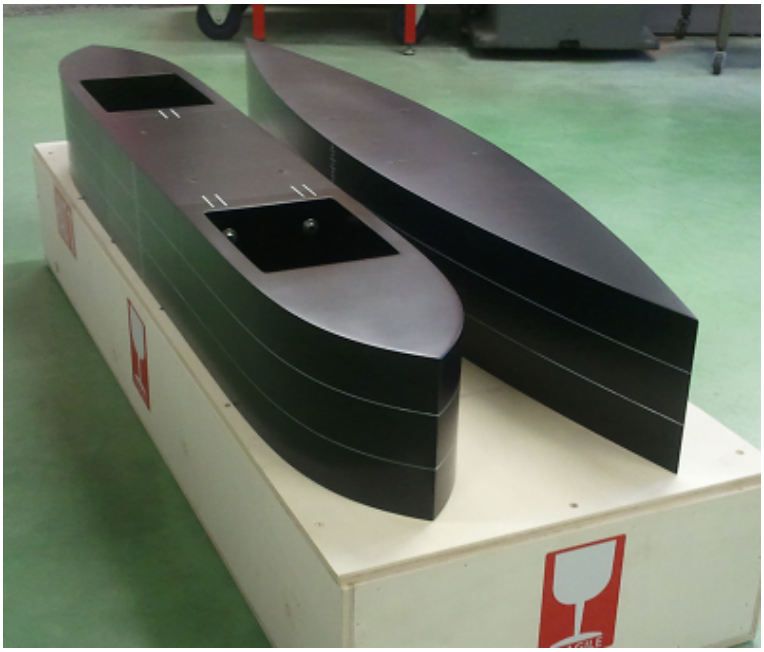

Figure 3.3.: *Picture of CWn8 (left) and CWn2 (right) model ship hulls*
Source: *Caplier et al. (2015)*

3.1.2. Ship waves optical measurement method

The ship waves are measured with an optical measurement method based on stereo correlation principle (Chatellier et al., 2010; Gomit et al., 2014). This non intrusive method allows to capture the entirety of the wave field with high precision. Two cameras focusing on the same zone are placed 1.5 m above the water surface with an angle of 35° with respect to the vertical axis and an opposite angle of ± 15° with respect to the horizontal axis. The cameras field covers a rectangular zone of $0.90 \times 0.75\ m^2$ corresponding to half of the canal width. Figure 3.4 shows a schematic view of the experimental set-up.

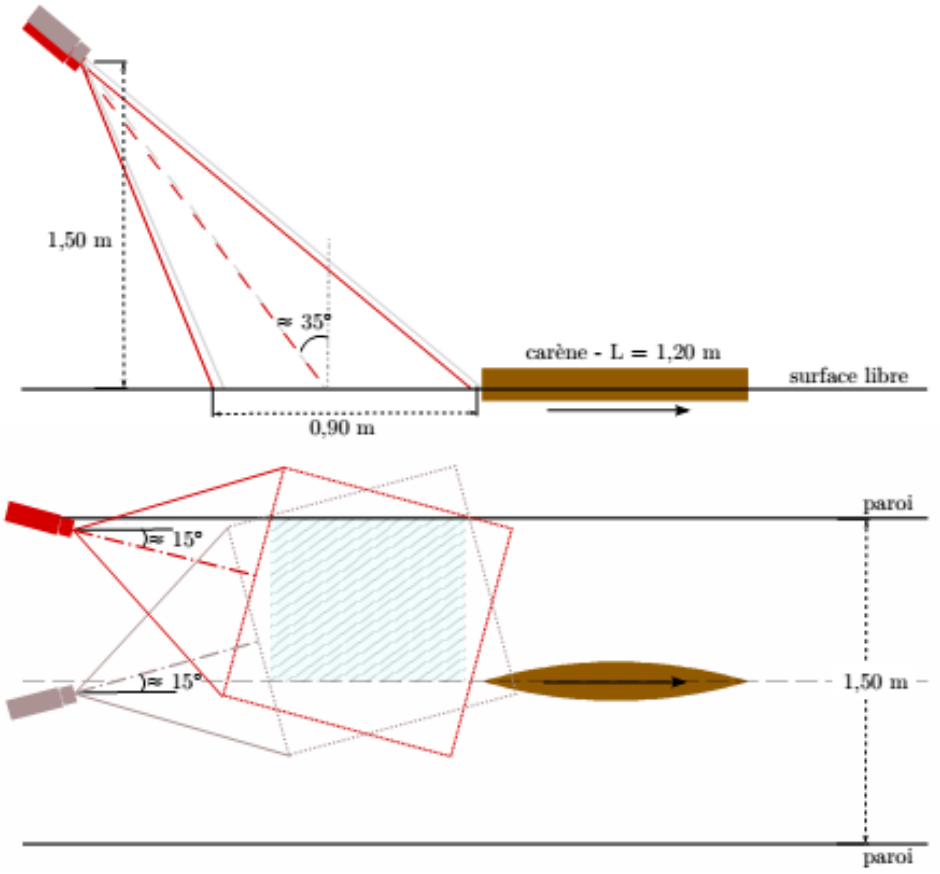

Figure 3.4.: *Schematic view of the wave measurement experimental set-up*
Source: *Caplier et al. (2015)*

The wave measurement procedure is as follows:

- the cameras are calibrated with a two-dimensional target of points displace along the longitudinal axis of the canal;
- the water surface is sowed with floating particles serving as markers following the free surface deformation before starting the video acquisition and launching the ship;
- each measurement is performed three times to check the reproducibility of the results;
- the wave field is reconstructed with a dedicated algorithm for each measurement and a mean wave field is calculated.

3.2. Numerical model

The numerical model described in chapter 2 is used for the comparison between experimental and numerical results. The geometrical configuration of the canal and ship hulls used in Pprime experiments have been reproduced. The numerical domain size extends from three times the ship length L in front of the model to five times the ship length behind the model; as showed in Figure 3.5.

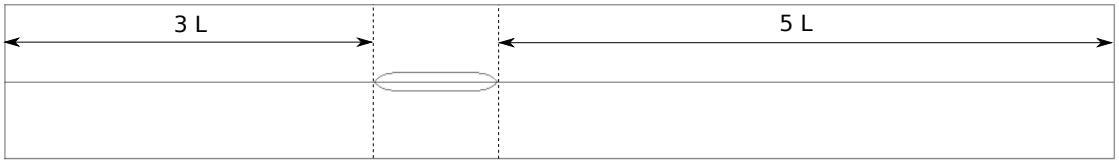

Figure 3.5.: *Schematic view of the numerical domain*

The mesh used for the numerical is composed of 680 000 structured elements. The mesh size is $dx = dy = 20\ mm$ between $x = -1.5L$ and $x = 3L$ and $dz = 2\ mm$ for the free surface. An overview of the generated mesh is shown in Figure 3.6 with a focus on the mesh around the ship.

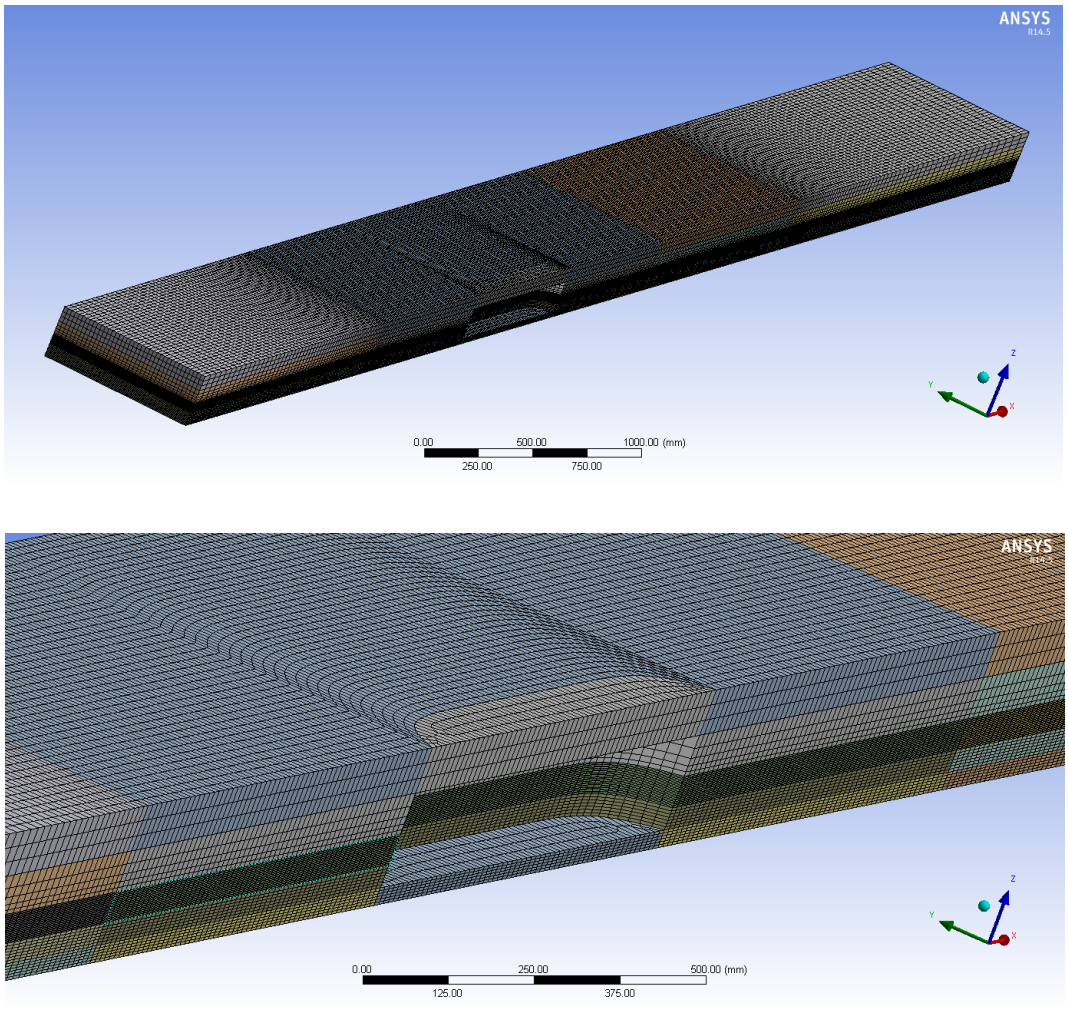

Figure 3.6.: *Generated mesh: (a) meshed domain with structured elements, (b) focus on the mesh around the ship*

3.3. Modelled configurations

The configurations used for the comparison between experiment and numerical simulation are summarized in Table 3.1 along with the corresponding parameters and Figure 3.7 shows a schematic view of the channel.

Table 3.1.: *Modelled configurations and corresponding parameters*

Hull	**V** [m/s]	$\mathbf{F_h}$ [-]	**H** [m]	**T** [m]	**W** [m]	**B** [m]	$\frac{\mathbf{H}}{\mathbf{T}}$ [-]	$\frac{\mathbf{W}}{\mathbf{B}}$ [-]	$\frac{\mathbf{A_C}}{\mathbf{A_S}}$ [-]
CWn2	0.45	0.45	0.103	0.075	1.5	0.18	1.37	8.33	11.44
CWn8	0.8	0.8	0.103	0.075	1.5	0.18	1.37	8.33	11.44

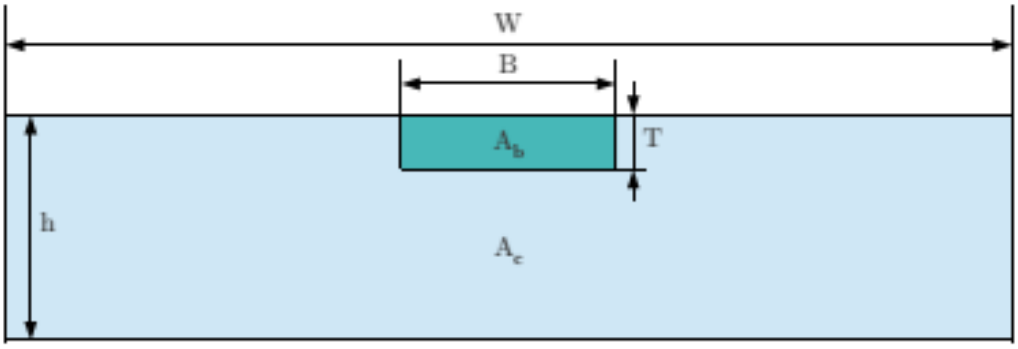

Figure 3.7.: *Schematic view of the channel cross section*

The following remarks can be made about the studied configurations:

- the ship was fixed and could not sink or trim;
- the channel configuration presents a high water depth restriction ($H/T = 1.34 < 4$) and no channel width restriction ($W/B = 8.33 > 4$);
- the speed tested for CWn8 hull is above Schijf limiting speed ($V_L = 0.81\ m/s$) for this configuration) and inland vessels do not navigate at such speeds.

3.4. Ship wave comparison between experimental and numerical results

3.4.1. CWn8 hull

Figure 3.8 shows (a) the experimental and (b) numerical results of the wave contours generated by the passage of CWn8 ship at a speed of 0.8 m/s.

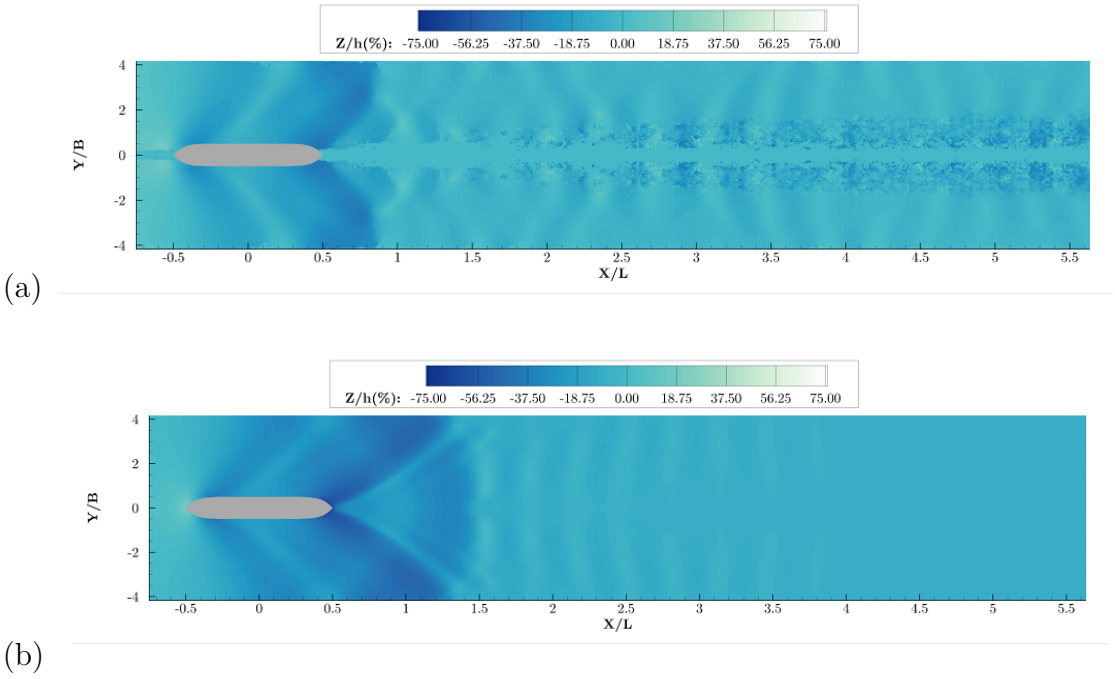

Figure 3.8.: *Wave contours generated by the passage of CWn8 ship at a speed of 0.8 m/s: (a) experimental results and (b) numerical results.*

The experimental and numerical wave contours exhibit the same wave pattern around the ship:

- transverse waves with a wavefront perpendicular to the ship movement direction;
- diverging waves with a wavefront forming a V shape;
- the intersection between diverging and transverse waves which forms a triangular area behind the ship.

However, some differences between the experimental and numerical results can also be observed:

- the triangular area formed by the intersection of diverging and transverse waves is larger in the numerical results;
- the height of the waves generated behind the ship (at $X/L > 1.5$) is decreasing faster in the numerical results than in the experimental results;
- the wave reflection on the banks is more important in the experimental results.

Figure 3.9 show the comparison between experimental (exp) and numerical (num) results on longitudinal profiles at $Y/B = 1,\ 2\ and\ 3$ for free surface elevation $Z - Z_0$.

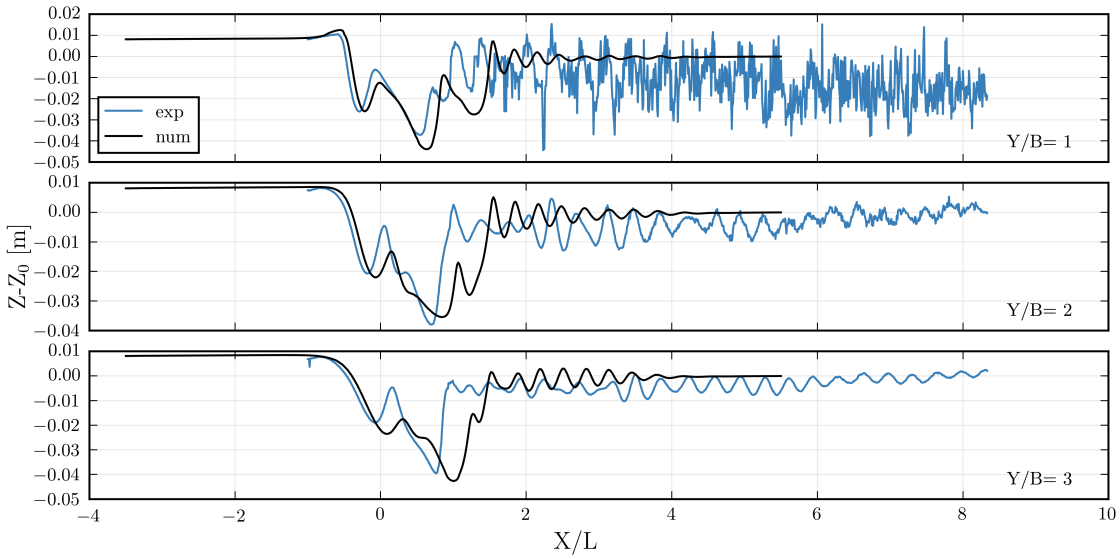

Figure 3.9.: *Free surface longitudinal profile $Z - Z_0$ (where $Z_0 = 0.103\ m$ is the water depth) at Y/B=1, 2 and 3.*

Figure 3.9 shows that the numerical free surface profiles closely correspond to the experimental profiles near the ship ($-1 < X/L < 1$); however, further away from the boat ($X/L > 1$), there seems to be an offset of the wave train. The wave amplitude of the numerical results also decreases faster than that of the experimental results. Finally, the numerical results profiles show an increase of water depth of around 0.01 m at the start of the numerical domain which is not present in the experimental profiles.

Figure 3.10 shows the comparison between experimental (exp) and numerical (num) results on longitudinal profiles at $Y/B = 1,\ 2\ and\ 3$ for free surface relative velocity $U - U_0$.

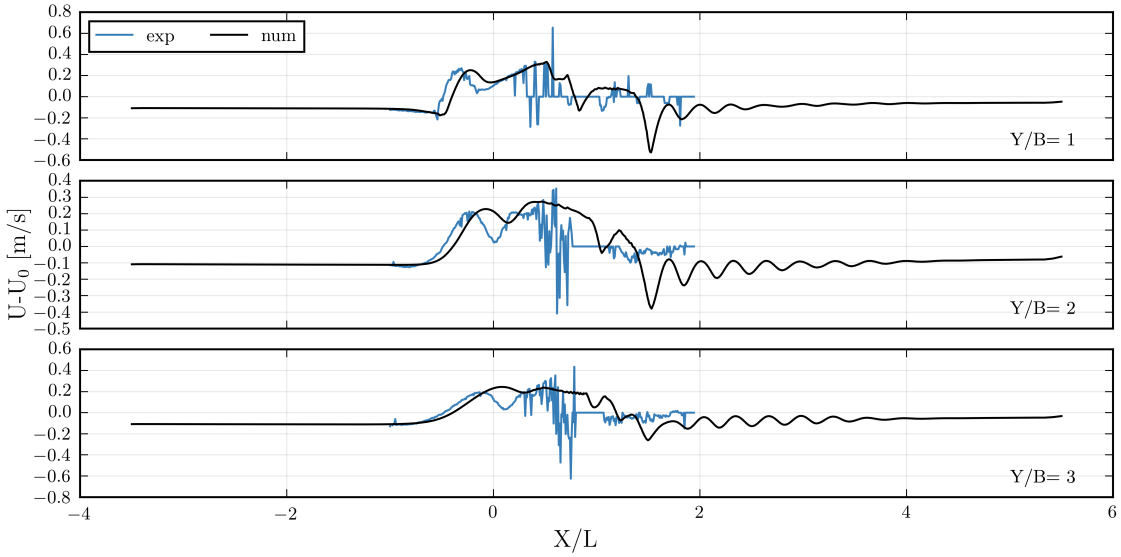

Figure 3.10.: *Free surface speed longitudinal profile $U - U_0$ (where $U_0 = 0.8\ m/s$ is the ship speed) at Y/B=1, 2 and 3.*

Figure 3.10 shows that the numerical and experimental results exhibit similar profiles for the relative free surface velocity. However, the numerical longitudinal profiles display negative velocity peak around $X/L = 1.5$ that is not present in the experimental profiles. This peak corresponds to the diverging wave forming the base of the triangle described in Figure 3.8. Indeed, the increase of water depth created by this wave also generates a decrease of free surface velocity. The numerical free surface profiles also show a 0.1 m/s velocity decrease at the front of the ship and propagating up to the inlet. This decrease in free surface velocity does not appear on the experimental profiles. Numerically, this decrease of velocity is explained by the conservation of mass: the water depth increase at the beginning of the numerical domain creates a velocity decrease. Physically, those two phenomenon (water depth increase and velocity decrease at the front of the ship) could be interpreted as if the bow wave is numerically propagating up to the beginning of the numerical domain. Finally, the quick variation of velocity and its peaks observed in the experimental data are due to experimental noise and do not represent any physical fluid behaviour These peaks are located after the stern of the ship where the flow is highly turbulent and the optical measurement method is able to accurately reconstruct the fluid flow.

Overall, the numerical model gives good hydrodynamic results around the ship.

However, in the numerical simulation, the amplitude of the ship waves and the wave reflection is too small and the bow wave seems to propagate up to the entry of the numerical domain. In order to study the source of those discrepancies, several parameters were studied such as the influence of the numerical domain size, mesh and speed. For simplification purpose, the mesh used for the numerical simulation presented in this section will be referred to as 'standard mesh'.

3.4.2. Influence of the numerical domain size

The same numerical simulation was run with a computational domain ranging from $-8.5L$ to $10L$ in the x-direction. Figure 3.11 shows the wave contour comparison between the (a) experimental results and (b) the numerical simulation with the domain increased in the x-direction. Figure 3.12 and Figure 3.13 show the comparison between experimental and numerical results on longitudinal profiles at $Y/B = 1,\ 2\ and\ 3$ respectively for free surface elevation $Z - Z_0$ and free surface relative velocity $U - U_0$. The numerical results obtained with the standard mesh are labeled as 'num std' and the results obtained with the extended computational domain are labeled as 'num X=[-8.5L,+10L]'.

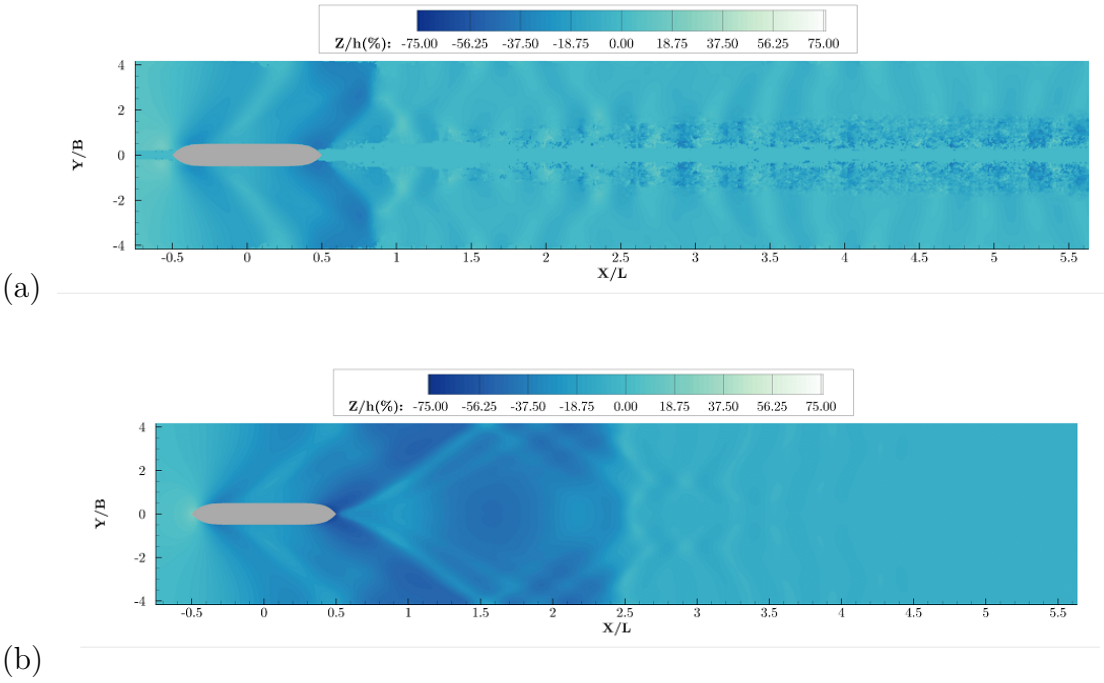

Figure 3.11.: *Wave contours generated by the passage of CWn8 ship at a speed of 0.8 m/s: (a) experimental results and (b) numerical results.*

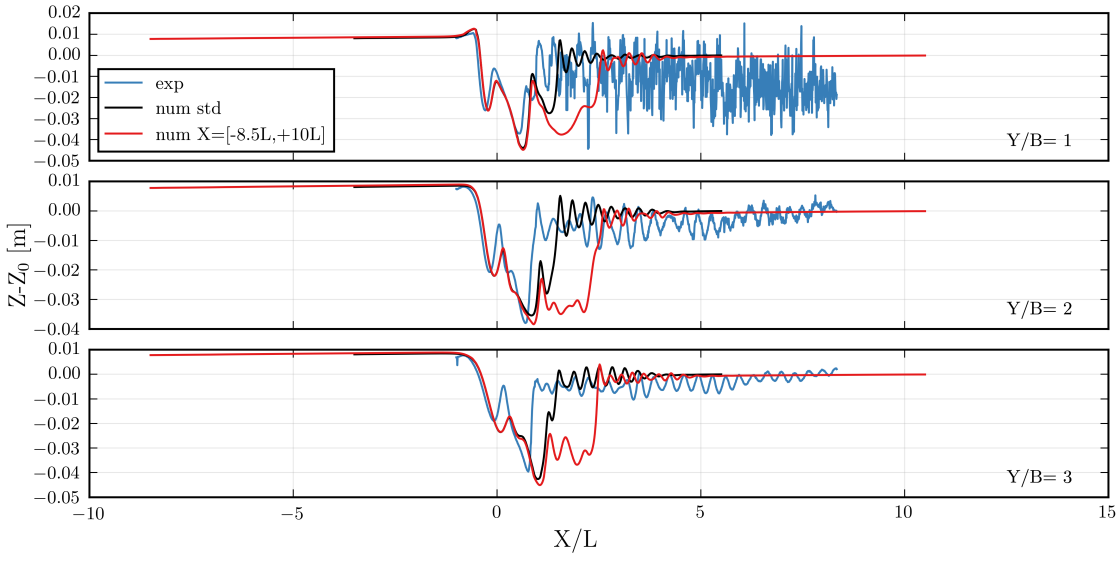

Figure 3.12.: *Free surface longitudinal profile $Z - Z_0$ (where $Z_0 = 0.103\ m$ is the water depth) at Y/B=1, 2 and 3.*

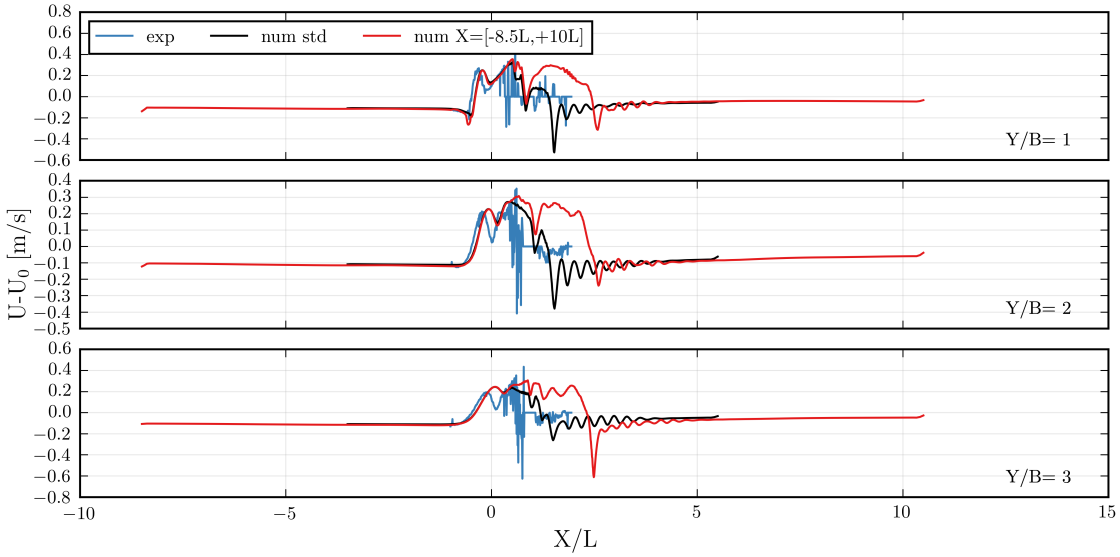

Figure 3.13.: *Free surface speed longitudinal profile $U - U_0$ (where $U_0 = 0.8\ m/s$ is the ship speed) at Y/B=1, 2 and 3.*

Figure 3.12 and Figure 3.13 show that the numerical results are the same for the standard and the extended domain around the ship: for $-0.5 \leq X/L \leq 0.5$, the red and black curves coincide. Those two figures also show that for the extended numerical domain, the bow wave still seems to be propagating up to the inlet and the amplitude of the simulated ship waves is too small. The main difference between the standard and extended numerical domain lie in the fact that the wave train for the extended numerical domain has been shifted toward the outlet. By comparing the wave contours for the numerical results in Figure 3.8 and Figure 3.11, the diverging waves for the extended domain seem to reflect on the bank at $1.5 \leq X/L \leq 2$ which is not the case for the standard domain.

Following the shift of the wave train toward the outlet with the extended domain, a simulation has been run with a computational domain ranging from $-1.5L$ to $+2L$ in the x-direction. Figure 3.14 and Figure 3.15 show the comparison between experimental and numerical results on longitudinal profiles at $Y/B = 1,\ 2\ and\ 3$ respectively for free surface elevation $Z - Z_0$ and free surface relative velocity $U - U_0$. The numerical results obtained with the standard mesh are labeled as 'num std' and the results obtained with the shrunk computational domain are labeled as 'num X=[-1.5L,+2L]'.

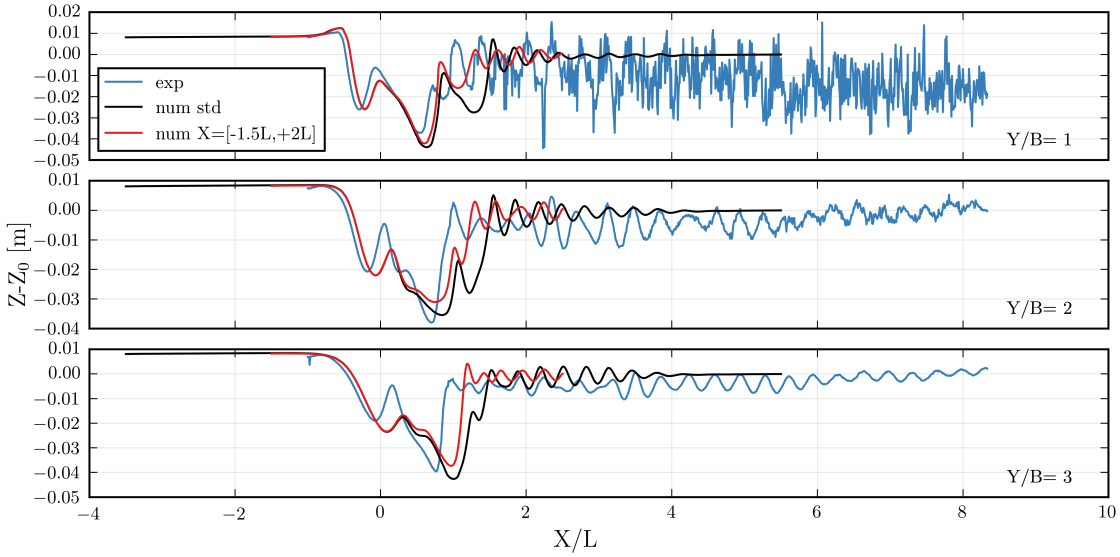

Figure 3.14.: *Free surface longitudinal profile $Z - Z_0$ (where $Z_0 = 0.103\ m$ is the water depth) at Y/B=1, 2 and 3.*

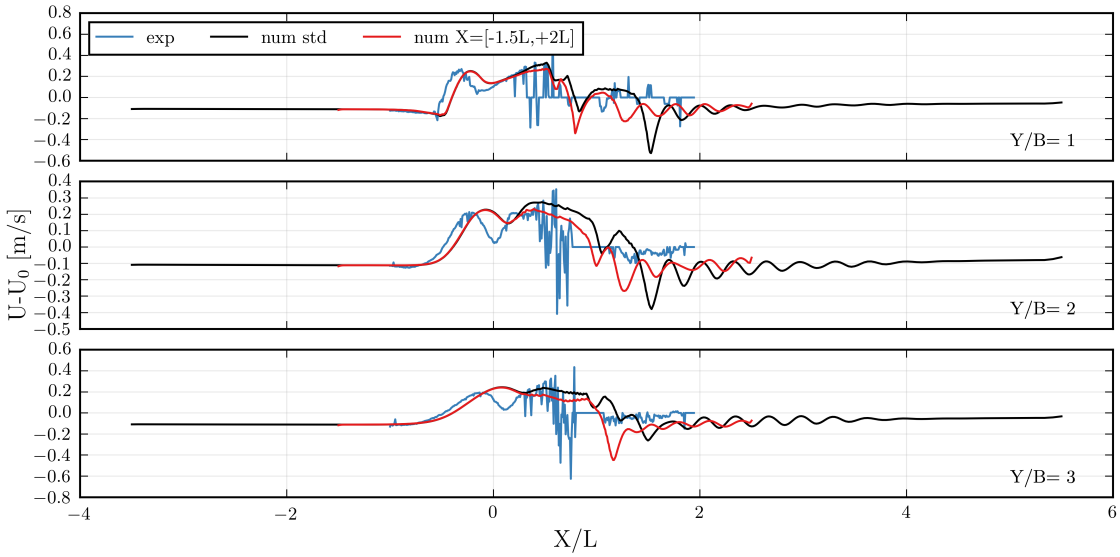

Figure 3.15.: *Free surface speed longitudinal profile $U - U_0$ (where $U_0 = 0.8\ m/s$ is the ship speed) at Y/B=1, 2 and 3.*

The observations made for the comparison between the results of the standard and extended numerical domain also apply for the comparison between the standard and shrunk domain: the numerical results are the same for the standard and the extended domain around the ship, the bow wave still seems to be propagating

up to the inlet and the amplitude of the simulated ship waves is too small. However, for the shrunk domain, the wave train has shifted toward the stern of the ship. Therefore, the distance between the ship and the outlet has an influence on the waves generated behind the ship.

A simulation has also been run with an extended numerical domain in the y-direction where the canal width is increased to four times the ship length. Theoretically, the influence on the numerical results should be small as in the studied configuration, the canal width restriction effect is very low. Figure 3.16 and Figure 3.17 show the comparison between experimental and numerical results on longitudinal profiles at $Y/B = 1,\ 2\ and\ 3$ respectively for free surface elevation $Z - Z_0$ and free surface relative velocity $U - U_0$. The numerical results obtained with the standard mesh are labeled as 'std' and the results obtained with the increased canal width are labeled as 'Binf'.

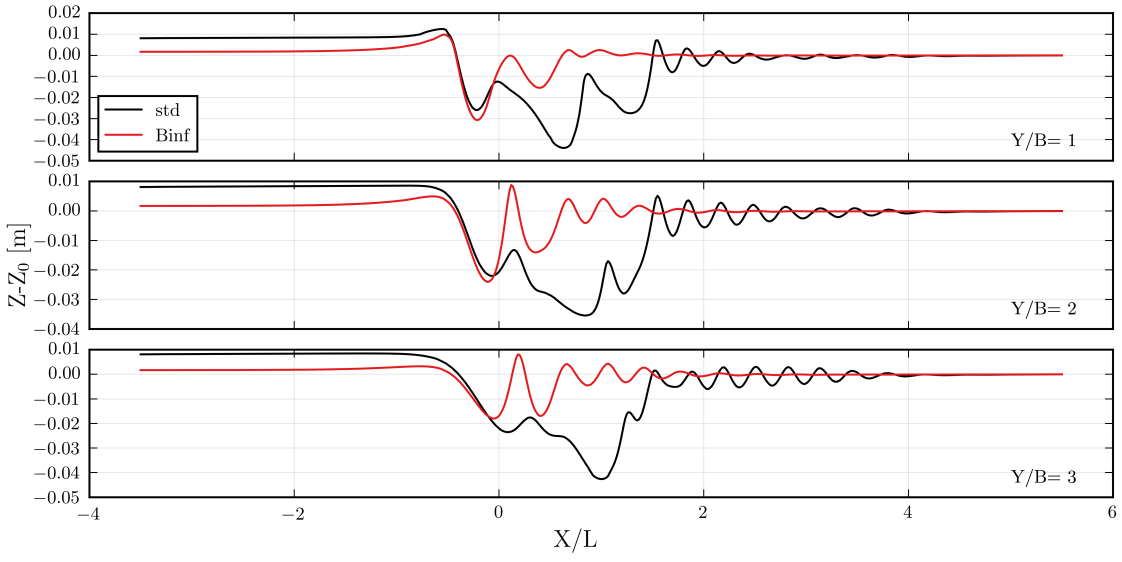

Figure 3.16.: *Free surface longitudinal profile $Z - Z_0$ (where $Z_0 = 0.103\ m$ is the water depth) at Y/B=1, 2 and 3.*

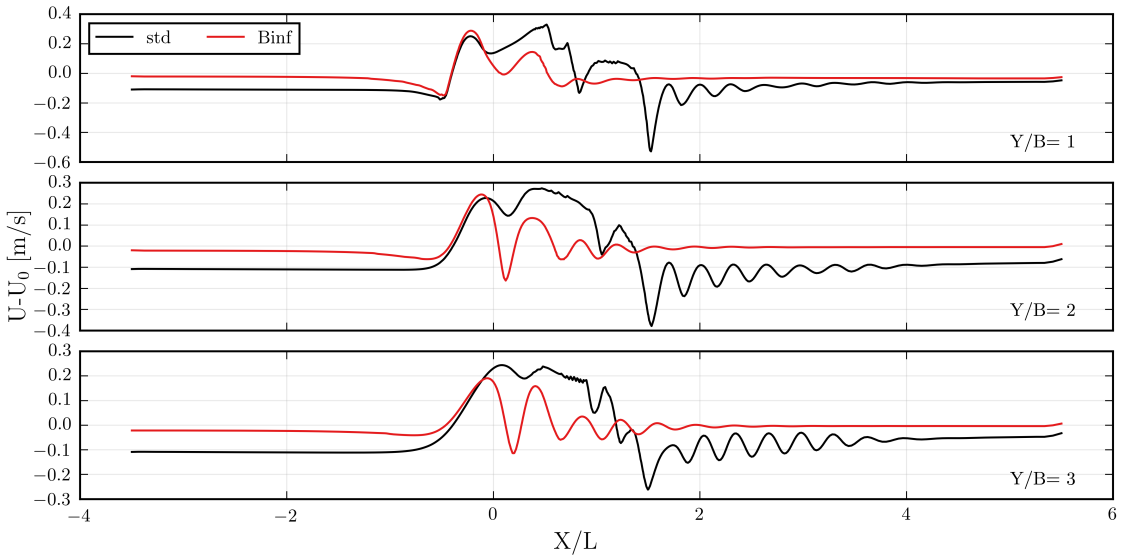

Figure 3.17.: *Free surface speed longitudinal profile $U - U_0$ (where $U_0 = 0.8\ m/s$ is the ship speed) at Y/B=1, 2 and 3.*

Figure 3.16 and Figure 3.17 show that for a wider domain in the y-direction, there is no water depth increase and no velocity decrease at the inlet. However, the flow around the ship is modified and less accurate compared to the standard domain. The amplitude of the waves behind the ship is also highly decreased compared to the initial domain.

Altogether, the distance between the ship and the outlet has an influence on the wave train position but no impact on the flow around the ship and the bow wave propagating up to the inlet. On the other hand, increasing the canal width seems to solve the flow problems at the inlet, however the flow around the ship is modified and less accurate.

3.4.3. Mesh influence

Several aspects of the initial mesh have been refined in order to study the influence on the simulated ship waves:

- free surface refinement, labelled as "SL";
- mesh refinement in the x-direction behind the ship, labelled as "dx";
- boundary layer mesh around the ship, labelled as "BL-S";

- boundary layer mesh at the bottom of the canal, labelled as "BL-B";
- boundary layer mesh at the wall (river banks), labelled as "BL-W".

Figure 3.18 and Figure 3.19 show the comparison between the numerical results for the mesh modifications described above on longitudinal profiles at $Y/B = 1,\ 2\ and\ 3$ respectively for free surface elevation $Z - Z_0$ and free surface relative velocity $U - U_0$.

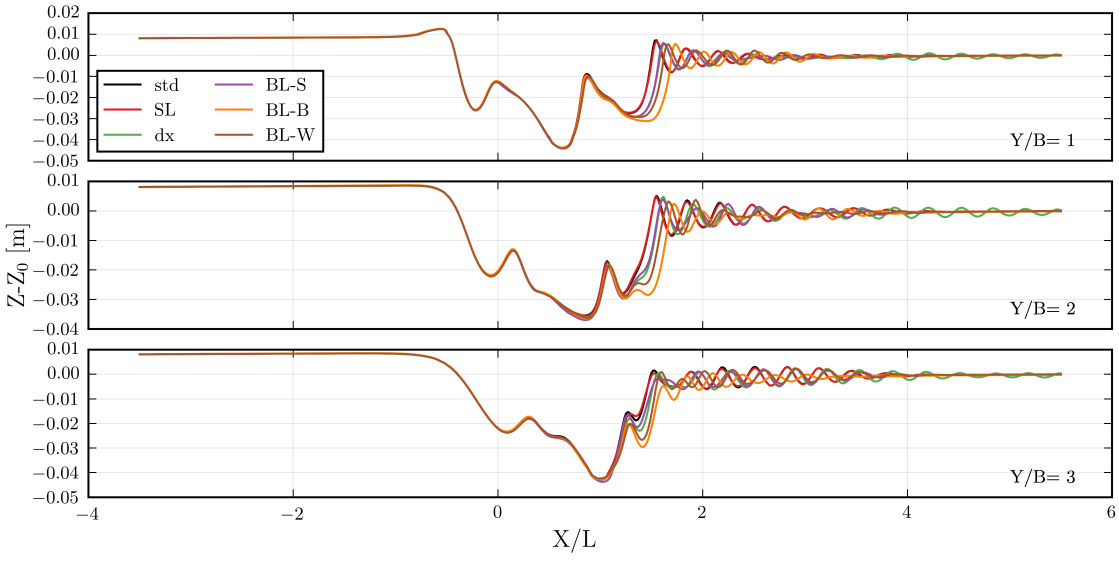

Figure 3.18.: *Free surface longitudinal profile $Z - Z_0$ (where $Z_0 = 0.103\ m$ is the water depth) at Y/B=1, 2 and 3.*

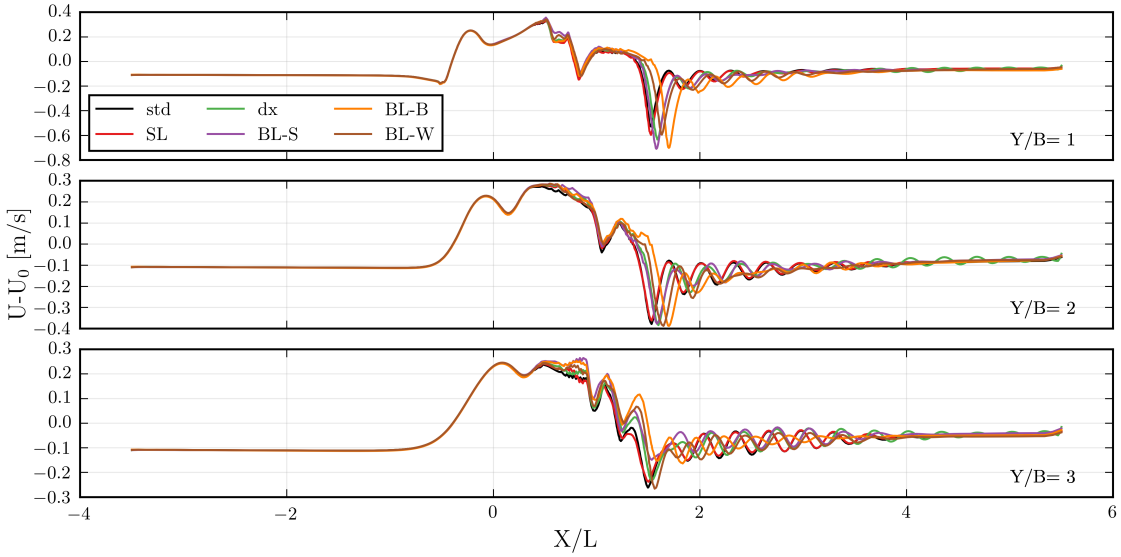

Figure 3.19.: *Free surface speed longitudinal profile $U - U_0$ (where $U_0 = 0.8\ m/s$ is the ship speed) at Y/B=1, 2 and 3.*

Figure 3.18 and Figure 3.19 show that the various mesh refinement do not influence the flow around and in front of the ship. However, all the refinement except that of the free surface cause a small shift of the wave train toward the outlet. Refining the mesh in the x-direction behind the ship (green curve) also allows to better capture the ship waves near the end of the domain. In the case of the standard mesh, the waves near the outlet are not captured because the grid spacing near the end of the domain is too coarse as an exponential grid biasing has been used. However the amplitude of those waves remains smaller than those observed in the experimental results.

3.4.4. Influence of ship speed and Froude number analysis

To study the influence of ship speed on the flow discrepancies near the inlet, a simulation with the CWn2 hull at 0.45 m/s speed has been run. Figure 3.20 shows the comparison between the numerical and experimental results on longitudinal profiles at $Y/B = 1,\ 2\ and\ 3$ for free surface elevation $Z - Z_0$.

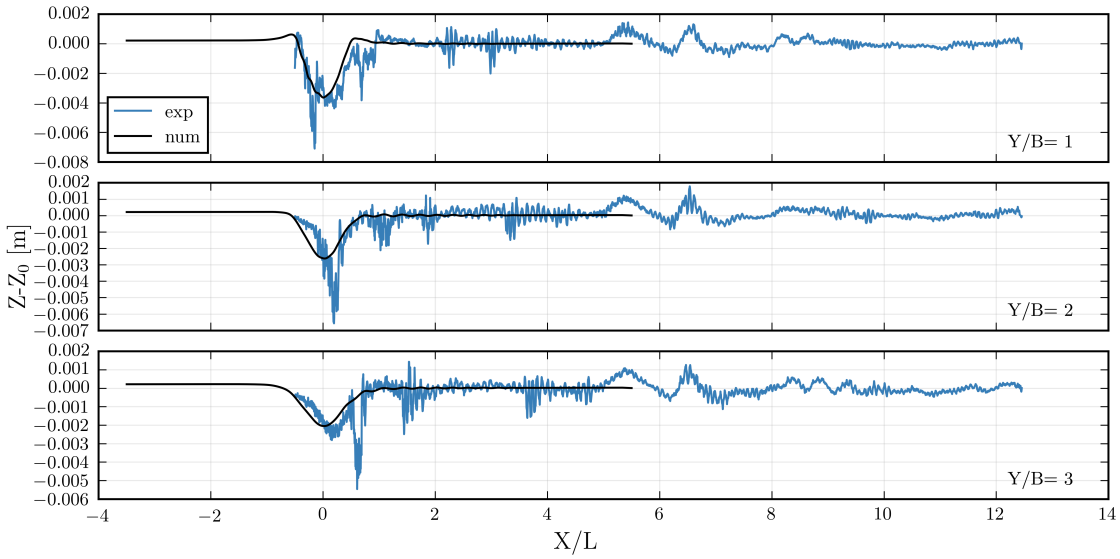

Figure 3.20.: *Free surface longitudinal profile $Z - Z_0$ (where $Z_0 = 0.103$ m is the water depth) at Y/B=1, 2 and 3.*

Figure 3.20 shows that for a speed of 0.45 m/s, there is no increase of water depth in front of the ship and therefore no propagation of the bow wave. The numerical results are also in good agreement with the experimental results even though the small waves are not captured. This is explained by the fact that the mesh used in this simulation is too coarse to capture the smaller waves. As a result, it would seem that the high velocity is the main cause for the flow discrepancies observed at the inlet.

It is possible that the discrepancies observed between the numerical and experimental results stem from the fact that in the numerical model the ship is not moving and its speed is applied to the fluid; while in the experiment the ship is towed. As a result, for high speed, a change in flow state (subcritical to supercritical) could explain the numerical errors. In order to investigate this hypothesis, a Froude number analysis has been carried out. Froude number is defined as follows:

$$Fr = \frac{U}{\sqrt{gH}} \tag{3.3}$$

where U and H are respectively the mean velocity in x-direction and mean water depth on a transversal section. Figure 3.21 shows the evolution of the Froude number for the CWn8 hull at 0.8 m/s with the initial mesh and the numerical

domain with the extended canal width (respectively labeled 'CWn8' and 'CWn8-Binf'), and the CWn2 hull at 0.45 m/s.

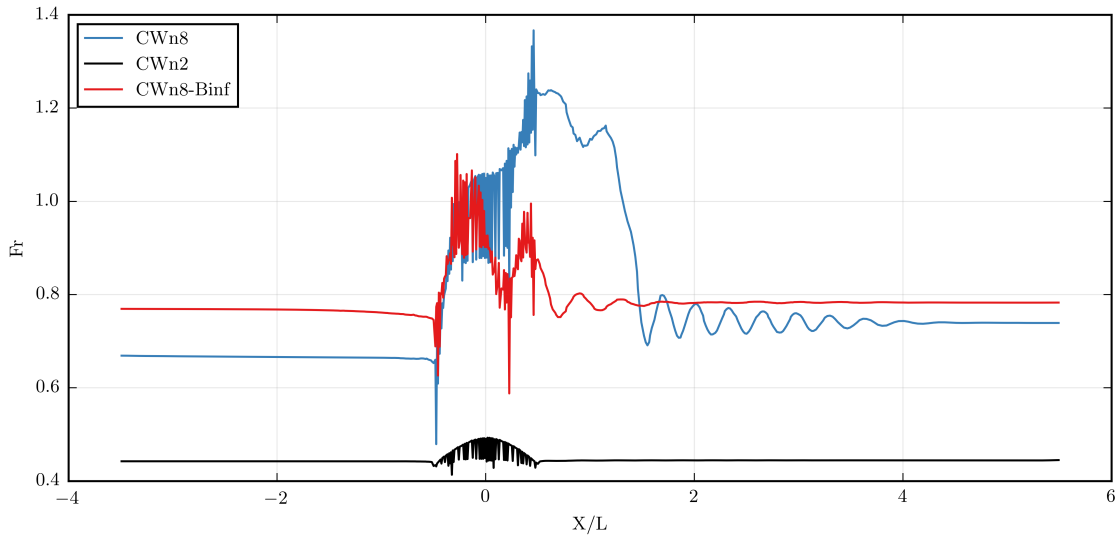

Figure 3.21.: *Evolution of the Froude number along x-axis for the CWn8 hull at 0.8 m/s with the initial mesh and the numerical domain with the extended canal width (respectively labeled 'CWn8' and 'CWn8-Binf'), and the CWn2 hull at 0.45 m/s*

Figure 3.21 shows that for the simulation with the CWn8 hull and the standard mesh, three flow regime conditions can be distinguished:

- in front of the ship ($X/L \leq 0.25$), the flow regime is subcritical;
- a flow regime transition from subcritical to supercritical occurs at $X/L \approx 0.25$ and the flow is supercritical around the ship;
- a new flow regime transition from supercritical to subcritical occurs at $X/L \approx 1.5$ and the flow is subcritical up to the outlet.

However, no flow regime transition are observed for the CWn8 hull at 0.8 m/s with the extended canal width and the Cwn2 hull. For those two configurations, no bow wave propagation was observed in the numerical results as well. As a result, there seems to be a correlation between the flow discrepancies observed near the inlet of the domain and the flow regime transition.

3.5. Conclusions

The comparison between empirical and numerical results highlighted some discrepancies in the simulation results. Overall, the hydrodynamic flow around the ship is accurate. However, several differences for the waves generated by the ship have been observed:

- little reflection of the waves on the banks;
- the numerical wave amplitude is too small;
- the bow wave seems to be propagating up to the inlet.

A sensitivity study on the influence of several numerical parameters on the results has been carried and showed that:

- the waves generated behind the ship are strongly influenced by the distance between the stern and the outlet;
- the bow wave propagation seems to be created by a change in flow regime due to the fact that the speed is given to the fluid and not the ship.

It should be noted that for accurate ship resistance evaluation, a good prediction of the flow around the ship is more important than a good prediction of the ship waves as in our model, the ship resistance is calculated by integrated fluid forces acting on the hull. However, it is possible that the differences in the hydrodynamic flow observed in this chapter are the source the ship resistance prediction errors at high speed reported in chapter 3.

Part II.

EcoNav speed optimization model for inland waterway

CHAPTER 4

EcoNav modules and numerical methods

This chapter describes the speed optimization model developed in this PhD. An overview of EcoNav modules is first given, then the methods used in each modules are described.

4.1. Model overview

EcoNav is based on an optimization algorithm minimizing the fuel consumption by finding the optimal speed profile for a given itinerary (operating conditions) under specified constraints (maximum travel duration). The fuel consumption FC_T is evaluated by a fuel consumption model which computes the fuel specific consumption corresponding to the thrust input. The thrust necessary to counteract the hydrodynamic forces is calculated with a ship resistance model. The ship resistance model calculates the hydrodynamic force R_T opposing the ship movement for given conditions (ship's load, channel geometry conditions, ship's speed, and current velocity). The constraint used in the optimization process is the maximum travel duration T_{max}. Finally, the operating conditions are defined by the parameters describing the hydrodynamics conditions in which the ship will sail on the itinerary. These conditions are the channel width W, the water depth H and the current velocity U. The last two quantities are predicted by using a 2D hydraulic

model (Telemac2D V7P0). Figure 4.1 below illustrates the working principle of EcoNav.

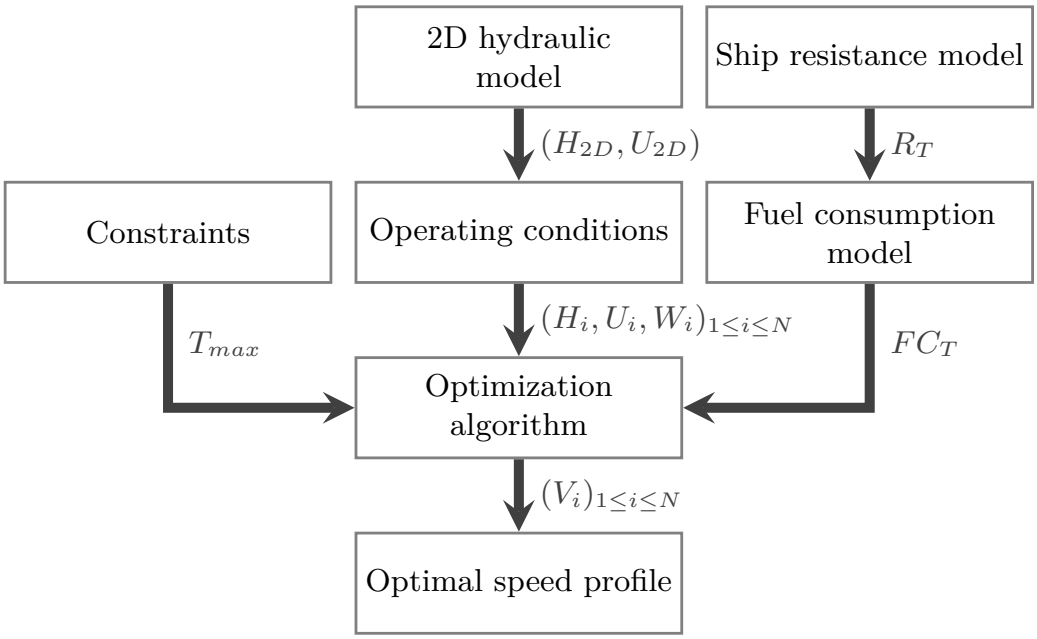

Figure 4.1.: *EcoNav flowchart*

4.2. Ship resistance model

In order to evaluate the fuel consumption of the ship, it is necessary to calculate the effective (towing) power $P_E = R_T \times V$ required to move the ship at a constant speed V. As a result, the ship resistance R_T has to be computed. This is done with the ship resistance model developed in this PhD and described in Chapter 2. However, the required computational time for this model is expensive, and the optimization algorithm requires many function calls before converging. To avoid expensive CFD simulations, a surrogate model (meta-modelling) is built from sampled data obtained via a Design of Experiment (DoE).

In this chapter, the experimental results from the University of Liege are used to build the response surface model (RSM) as the number of experimental samples available are greater than those of CFD simulations. In the long term, it is planned to replace the experimental data with numerical results from the ship resistance model described in chapter 2. Indeed, the experimental data used for this model

is specific to one ship and the numerical method presented in chapter 3 can be applied for any restricted waterway configuration and any inland vessel to calculate accurate results of ship resistance. Popular surrogate model techniques include ordinary least square (LSM), moving least square (MLS), Kriging, support vector regression (SVR) and radial basis functions (RBF).

4.2.1. Surrogate model techniques

In order to avoid repeated use of computationally expensive simulations, surrogate models are often used to provide rapid approximations of more expensive models. These models are used in the engineering community for a wide range of application (Koziel and Leifsson, 2013). Queipo et al. (2005) presented an overview of the most popular methods used for surrogate-based analysis and optimization. Forrester and Keane (2009); Simpson et al. (2008) reviewed the progresses made by surrogate-model analysis since it was first introduced by Sacks et al. (1989).

The surrogate modelling approach approximates the simulation or experimental data $f_p(\boldsymbol{x})$ with the surrogate model output $\widehat{f}_p(\boldsymbol{x})$:

$$f_p(\boldsymbol{x}) = \widehat{f}_p(\boldsymbol{x}) + \varepsilon(\boldsymbol{x}) \tag{4.1}$$

where $\boldsymbol{x}$ is the coordinate vector where the function is evaluated and $\varepsilon(\boldsymbol{x})$ is the approximation error.

In this chapter, the experimental results from the University of Liège are used to build the response surface model (RSM) as the number of experimental samples available are greater than those of CFD simulations. The governing parameters used for this surrogate model are the water depth H to ships draught T ratio H/T (quantifying the water depth restriction); the channel width W to ships breadth B ratio W/B (characterizing the channel width restriction) and the vessels speed V. It is worth mentioning that those parameters are independent and characterize the three main factors who have an effect on ship resistance in restricted waterway. As a result, the ship total resistance R_T is expressed as follows:

$$R_T = f(V, \frac{H}{T}, \frac{W}{B}) = f(X) = \widehat{R}_T + \varepsilon \tag{4.2}$$

where $\boldsymbol{X} = (V, H/T, W/B)$ is the coordinate vector and $\widehat{R}_T$ is the approximation function of R_T given by the surrogate model.

To evaluate the accuracy of the model, the mean square error (MSE) is calculated:

$$MSE = \frac{1}{n}\sum_{i=1}^{n}(R_{Ti} - \widehat{R}_{Ti})^2 \tag{4.3}$$

where $(\widehat{R}_{Ti} = \widehat{R}_T(\boldsymbol{X_i}))_{i=1..n}$ are the n predictions of the n observed data points $(R_{Ti} = R_T(\boldsymbol{X_i}))_{i=1..n}$.

The following popular surrogate modelling methods have been tested for the construction of the ship resistance surrogate model:

- polynomial regression model;
- moving least square method (MLS);
- Kriging modelling;
- support vector regression (SVR);
- radial basis functions (RBF).

Polynomial regression model

The classic polynomial response surface model is the original form of surrogate model and is still widely used in the engineering community. Box et al. (1987) extensively covered this subject. A polynomial approximation of order $Np = 2$ is used for the ship resistance $\widehat{R}_T$:

$$\widehat{R}_T(\boldsymbol{X}) = \sum_{j=1}^{m} a_j p_j(\boldsymbol{X}) = \boldsymbol{p^T}(\boldsymbol{X})\boldsymbol{a} \tag{4.4}$$

where $\boldsymbol{p}$ is a matrix of polynomial basis functions, $\boldsymbol{a} = [a_1, ..., a_m]^T$ is the vector of unknown coefficients and m is the number of elements in $\boldsymbol{a}$ (dimension of the polynomial basis). The dimension m of the space of polynomials of total degrees Np in d spatial dimension is given by $m = \frac{(Np+d)!}{Np!d!}$ (in this case, $d = 1$ as R_T is a function in $\mathbb{R}$; see Levin (1998)).
The regression coefficients vector $\boldsymbol{a}$ is then computed as:

$$\boldsymbol{a} = (\boldsymbol{p}^T\boldsymbol{p})^{-1}\boldsymbol{p}^T\boldsymbol{R_T} \tag{4.5}$$

Moving least square method

The moving least squares method (Lancaster and Salkauskas, 1981; Levin, 1998) is a technique developed for smoothing and interpolating data from a set of unorganized point samples. This method can be considered as an extension of the weighted least square approach (Aitken, 1936) where each observation is given a sample $w_i \geq 0$ defining the importance of each data point. In the moving least squares method, the weighting coefficients w_i are not constant and depend on the distance between the observation points and the point to be predicted. As a result, the coefficients must be computed for every prediction and the method is computationally more expensive. In MLS method, the approximated ship resistance is written as:

$$\widehat{R}_T(\boldsymbol{X}) = \sum_{j=1}^{m} p_j(\boldsymbol{X}) a_j(\boldsymbol{X}) = \boldsymbol{p^T}(\boldsymbol{X})\boldsymbol{a}(\boldsymbol{X}) \tag{4.6}$$

The formulation is the same as in the polynomial regression method except that the regression coefficient vector $\boldsymbol{a}$ depends on the coordinate vector $\boldsymbol{X}$. The coefficients $a_j(\boldsymbol{X})$ are determined by minimizing the following function:

$$J(\boldsymbol{X}) = \sum_{i=1}^{n} w(\boldsymbol{X} - \boldsymbol{X_i})(\widehat{R}_{Ti} - R_{Ti})^2 = \sum_{i=1}^{n} w(\boldsymbol{X} - \boldsymbol{X_i})(\boldsymbol{p^T}(\boldsymbol{X_i})\boldsymbol{a}(\boldsymbol{X_i}) - R_{Ti})^2 \tag{4.7}$$

where w is a weighting function.

The commonly used weighting functions include the Gaussian, the cubic spline and the quadratic weighting functions:

$$w_i(\boldsymbol{X}) = \begin{cases} e^{\frac{r_i}{\alpha}}, & \text{if } r_i \leq 1 \\ 0, & \text{si} r_i > 0 \end{cases} \tag{4.8}$$

$$w_i(\boldsymbol{X}) = \begin{cases} \frac{2}{3} - 4r_i^2 + 4r_i^3, & \text{if } r_i \leq 0.5 \\ \frac{4}{3} - 4r_i + 4r_i^2 + \frac{4}{3}r_i^3, & \text{if } 0.5 \leq r_i \leq 1 \\ 0, & \text{if } r_i > 0 \end{cases} \tag{4.9}$$

$$w_i(\boldsymbol{X}) = \begin{cases} 1 - 6r_i^2 + 8r_i^3 - 3r_i^4, & \text{if } r_i \leq 1 \\ 0, & \text{if } r_i > 0 \end{cases} \tag{4.10}$$

where $r_i = \frac{\|\boldsymbol{X}-\boldsymbol{X_i}\|}{r_0}$ is the relative distance, r_0 is the influencing radius and α is a shape parameter.

Equation (4.7) can be written in matrix form:

$$J = [\boldsymbol{Pa}(\boldsymbol{X}) - \boldsymbol{R_T}]^T \boldsymbol{W} [\boldsymbol{Pa}(\boldsymbol{X}) - \boldsymbol{R_T}] \tag{4.11}$$

where $\boldsymbol{R_T} = [R_{T1}, R_{T2}, ..., R_{Tn}]^T$ and $\boldsymbol{P}$ and $\boldsymbol{W}$ are given by:

$$\boldsymbol{P} = \begin{bmatrix} \boldsymbol{p}^T(\boldsymbol{X_1}) \\ \boldsymbol{p}^T(\boldsymbol{X_2}) \\ \vdots \\ \boldsymbol{p}^T(\boldsymbol{X_n}) \end{bmatrix}_{n \times m} = \begin{bmatrix} p_1(\boldsymbol{X_1}) & p_2(\boldsymbol{X_1}) & \cdots & p_m(\boldsymbol{X_1}) \\ p_1(\boldsymbol{X_2}) & p_2(\boldsymbol{X_2}) & \cdots & p_m(\boldsymbol{X_2}) \\ \vdots & \vdots & \ddots & \cdots \\ p_1(\boldsymbol{X_n}) & p_2(\boldsymbol{X_n}) & \cdots & p_m(\boldsymbol{X_n}) \end{bmatrix} \tag{4.12}$$

$$\boldsymbol{W} = \begin{bmatrix} w(\boldsymbol{X} - \boldsymbol{X_1}) & 0 & \cdots & 0 \\ 0 & w(\boldsymbol{X} - \boldsymbol{X_2}) & \cdots & 0 \\ \vdots & \vdots & \ddots & \vdots \\ 0 & 0 & \cdots & w(\boldsymbol{X} - \boldsymbol{X_n}) \end{bmatrix} \tag{4.13}$$

The coefficients $\boldsymbol{a}(\boldsymbol{X})$ and the approximated ship resistance $\widehat{R}_T(\boldsymbol{X})$ can be calculated with :

$$\boldsymbol{a}(\boldsymbol{X}) = \boldsymbol{A}^{-1}(\boldsymbol{X}) \boldsymbol{B}(\boldsymbol{X}) \boldsymbol{R_T} \tag{4.14}$$

$$\widehat{R}_T(\boldsymbol{X}) = \boldsymbol{p^T}(\boldsymbol{X}) \boldsymbol{a}(\boldsymbol{X}) = \boldsymbol{p^T}(\boldsymbol{X}) \boldsymbol{A}^{-1}(\boldsymbol{X}) \boldsymbol{B}(\boldsymbol{X}) \boldsymbol{R_T} \tag{4.15}$$

where $\boldsymbol{A} = [\boldsymbol{P}^T \boldsymbol{W} \boldsymbol{P}]$ and $\boldsymbol{B} = [\boldsymbol{P}^T \boldsymbol{W}]$. This method has been programmed in Python 3 language.

Kriging method

Kriging is a method originally designed by the South African mining engineer Krige (1951) and the theoretical basis for this method was developed by the French mathematician Matheron (1963). The use of Kriging method in the context of modelling and optimization of deterministic functions was popularized following the work of Sacks et al. (1989). Kriging is based on the hypothesis the function to approxi-

mate is the sum of two components: a linear model (e.g. polynomial trend) and a statistical model:

$$\widehat{R}_T = \boldsymbol{f}(\boldsymbol{X})^T\boldsymbol{\beta} + Z(\boldsymbol{X}) \tag{4.16}$$

where $\boldsymbol{f}(\boldsymbol{X}) = [f_1(\boldsymbol{X}), f_2(\boldsymbol{X}), \cdots, f_K(\boldsymbol{X})]^T$ are known functions, $\boldsymbol{\beta} = [\beta_1, \beta_2, \cdots, \beta_K]^T$ are the unknown model parameters, and $Z(\boldsymbol{X})$ is a normally distributed Gaussian process with zero mean and variance σ^2. it should be noted that in this model, unlike with the MLS method, the unknown regression parameter β does not depend on the coordinate vector $\boldsymbol{X}$. Therefore, this method is computationally less expensive than MLS.

The linear regression part $\boldsymbol{f}(\boldsymbol{X})^T\boldsymbol{\beta}$ globally approximates the function and the statistical part $Z(\boldsymbol{X})$ accounts for local variations. The covariance matrix of $Z(\boldsymbol{X})$ is given by:

$$Cov[Z(\boldsymbol{X_i})Z(\boldsymbol{X_j})] = \sigma^2\boldsymbol{R}([R(\boldsymbol{X_i}, \boldsymbol{X_j})]) \tag{4.17}$$

where $\boldsymbol{R}$ is a $n \times n$ correlation matrix with $R_{ij} = R(\boldsymbol{X_i}, \boldsymbol{X_j})$. $R(\boldsymbol{X_i}, \boldsymbol{X_j})$ is a correlation function between observation data points $\boldsymbol{X_i}$ and $\boldsymbol{X_j}$.

In Python pogramming language, Kriging method is implemented in an open source package called "scikit-learn" (Pedregosa et al., 2011). This implementation is based on a translation of the DACE Matllab toolbox (Lophaven et al., 2002). This package provides linear regression models with polynomials of order 0, 1 and 2 and various correlation functions are also available. This package has been used to predict ship resistance values with a 2$^{\text{nd}}$ order polynomial as regression model and a Gaussian correlation function:

$$R(\boldsymbol{X}, \boldsymbol{Y}) = exp\Big[-\sum_{k=1}^{m}\theta_k|X_k - Y_k|^2\Big] \tag{4.18}$$

where θ_k are unknown correlation parameters, and X_k and Y_k are respectively the k^{th} component of the vectors $\boldsymbol{X}$ and $\boldsymbol{Y}$.

Support vector regression method

SVR is the application of support vector machine (SVM) theory developped at AT&T Bell Laboratories in the 1980s (Drucker et al., 1997). A comprehensive tutorial on SVR has been published by Smola and Schölkopf (2004) and Basak et al. (2007)

reviewed the existing theory, methods and recent developments of SVR. The basic idea behind SVR is to find an approximating function $\widehat{R}_T(\boldsymbol{X})$ that has a maximum deviation ε from the sample data and at the same time is as flat as possible. In the linear case, the approximating function is written as:

$$\widehat{R}_T(\boldsymbol{X}) = \boldsymbol{w}^T \boldsymbol{X} + b \tag{4.19}$$

where the parameter vector $\boldsymbol{w}$ and the bias b are the unknowns. A solution satisfying the conditions cited above can be found by solving the following optimization problem:

$$\begin{aligned} \min_{\boldsymbol{\alpha},\boldsymbol{\alpha}^*} \quad & \frac{1}{2}\sum_{i=1}^{n}\sum_{j=1}^{n}(\alpha_i - \alpha_i^*)(\alpha_j - \alpha_j^*)\boldsymbol{X_i}^T\boldsymbol{X_j} + \varepsilon\sum_{i=1}^{n}(\alpha_i + \alpha_i^*) + \sum_{i=1}^{n} R_{Ti}(\alpha_i^* - \alpha_i) \\ \text{subject to} \quad & \begin{cases} \sum_{i=1}^{n}(\alpha_i - \alpha_i^*) = 0 \\ 0 \leq \alpha_i, \alpha_i^* \leq C, i = 1 \cdots, n \end{cases} \end{aligned} \tag{4.20}$$

where $C > 0$ determines the trade off between the flatness of the function and the amount up to which deviations larger than ε are tolerated and α and $\boldsymbol{\alpha}^*$ are Lagrangian multipliers.

The solution of this optimization problem is then equal to:

$$\widehat{R}_T(\boldsymbol{X}) = \sum_{i=1}^{n}(\alpha_i^+ - \alpha_i^-)\boldsymbol{X}_i^T\boldsymbol{X} \tag{4.21}$$

This method can be extended to non linear cases by using kernel functions $K(\boldsymbol{X_i}, \boldsymbol{X_j}) = \phi(\boldsymbol{X_i})^T\phi(\boldsymbol{X_j})$ where $\phi(\boldsymbol{X})$ is a transformation that maps $\boldsymbol{X}$ to a high dimensional space. The optimization problem to solve for the non linear algorithm is:

$$\begin{aligned} \min_{\boldsymbol{\alpha},\boldsymbol{\alpha}^*} \quad & \frac{1}{2}\sum_{i=1}^{n}\sum_{j=1}^{n}(\alpha_i - \alpha_i^*)(\alpha_j - \alpha_j^*)K(\boldsymbol{X_i}, \boldsymbol{X_j}) + \varepsilon\sum_{i=1}^{n}(\alpha_i + \alpha_i^*) + \sum_{i=1}^{n} R_{Ti}(\alpha_i^* - \alpha_i) \\ \text{subject to} \quad & \begin{cases} \sum_{i=1}^{n}(\alpha_i - \alpha_i^*) = 0 \\ 0 \leq \alpha_i, \alpha_i^* \leq C, i = 1, ..., n \end{cases} \end{aligned} \tag{4.22}$$

an the solution is then equal to:

$$\widehat{R}_T(\boldsymbol{X}) = \sum_{i=1}^{n}(\alpha_i - \alpha_i^*)K(\boldsymbol{X_i}, \boldsymbol{X}) \tag{4.23}$$

The SVR method is also implemented in the "scikit-learn" Python package. This package has been used to predict ship resistance values with a Gaussian kernel:

$$K(\boldsymbol{X}, \boldsymbol{Y}) = exp(-\gamma \parallel \boldsymbol{X} - \boldsymbol{Y} \parallel^2) \tag{4.24}$$

Radial basis function

Hardy (1971) first used radial basis functions for the interpolation of scattered multivariate data. This method uses a weighted linear combination of radially symmetric functions ϕ to approximate ship resistance as:

$$\widehat{R}_T(\boldsymbol{X}) = \boldsymbol{w}^T\boldsymbol{\phi} = \sum_{i=1}^{n} w_i\phi(\|\boldsymbol{X} - \boldsymbol{X_i}\|) \tag{4.25}$$

where $\boldsymbol{w} = [w_1, ..., w_n]$ represents the unknown coefficients of the linear combination.

This linear system can the be resolved by using the matrix method of linear least squares. It is worth noticing that this formulation of the RBF method is an interpolating method, but it can be extended to an approximating method by adding a bias term $b(\boldsymbol{X})$ (often taken as a polynomial) to Equation (4.25). In this chapter, the RBF method was used without any bias term and further details about the use of a bias term can be found in Amouzgar and Strömberg (2015). The RBF method is implemented in the Python package Scipy (Jones et al., 2001) and has been used to approximate ship resistance with a cubic RBF:

$$\phi(r) = r^3 \tag{4.26}$$

4.3. Fuel consumption model

To evaluate fuel consumption, it is necessary to calculate the break power P_B delivered by the main engine to move the ship at a speed V. However, this power

is greater than the effective (towing) power $P_E = R_T \times V$ because of the various energy loss occurring in the ship propulsion.

4.3.1. Ship propulsion

The main components of ship propulsion are:

- a prime mover (engine) transforming an energy source into rotational mechanical energy;
- a reduction gear reducing the high rotation speed of the engine;
- a main shaft supported and held in alignment by bearings and transmitting the rotational mechanical energy from the reduction gear to the propeller;
- a propeller converting rotational motion into thrust by imparting velocity to a column of water and moving it in the opposite direction of the ship movement.

Figure 4.2 illustrates the basic principle of geared ship propulsion.

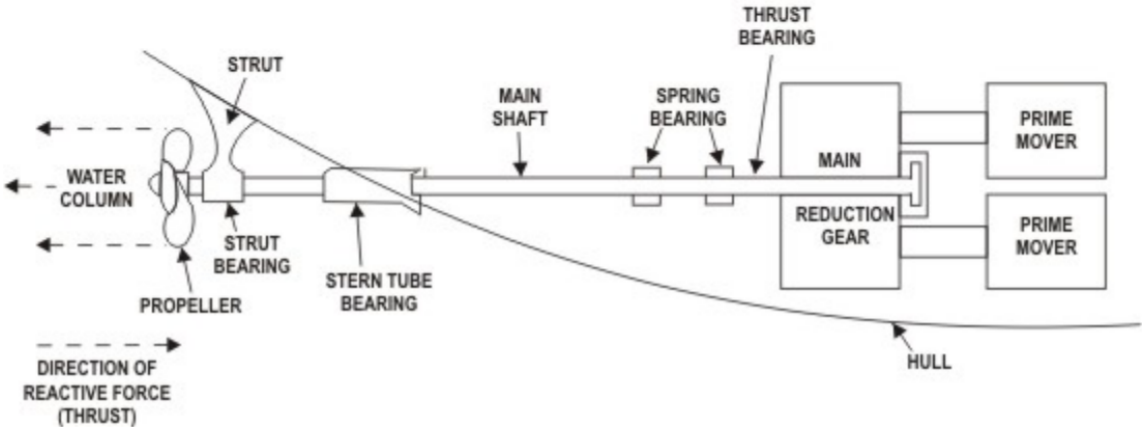

Figure 4.2.: *General principal of geared ship propulsion*
Source: *www.propellerpages.com*

The energy loss occurring between each energy transformation is quantified through the use efficiency parameters:

- the hull efficiency $\eta_H = \frac{P_E}{P_T}$ is the ratio between the effective power P_E and the thrust power P_T delivered by the propeller to the water,
- the propeller efficiency $\eta_B = \frac{P_T}{P_B}$ is the ratio between the thrust power P_T and the power delivered to the propeller P_D;

- the shaft efficiency $\eta_S = \frac{P_D}{P_B}$ is the ratio between the power P_D delivered to the propeller and the brake power P_B delivered by the main engine.

The global propulsion efficiency η_G is defined as the product of the three efficiencies described above:

$$\eta_G = \eta_H \times \eta_B \times \eta_S \tag{4.27}$$

Figure 4.3 illustrates the performance quantification of a typical ship propulsion.

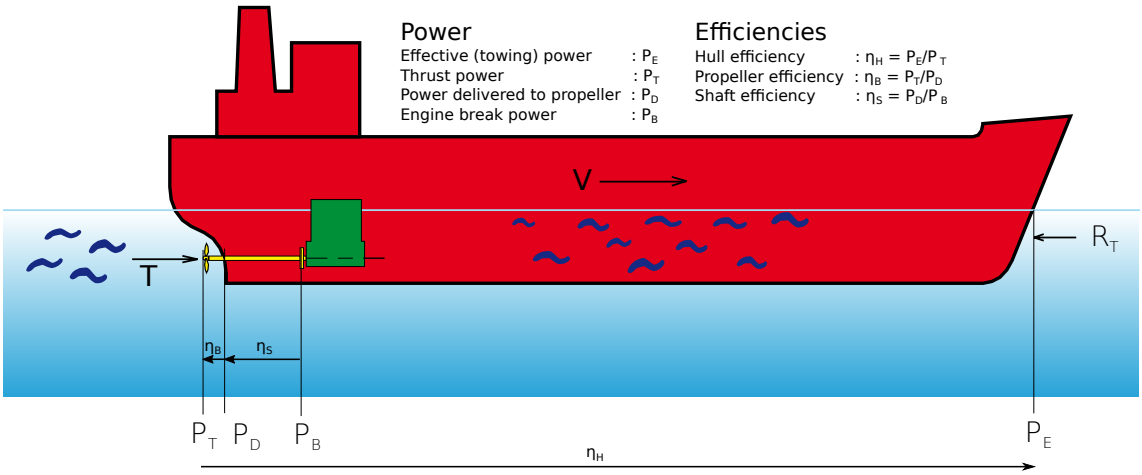

Figure 4.3.: *Performance of a typical ship propulsion*
Source: *adapted from MAN (2011)*

By using the energy efficiencies described above, the link between the break power P_B delivered by the main engine and the effective power P_E can be written as:

$$P_B = \frac{1}{\eta_H \times \eta_S \times \eta_S} P_E = \frac{1}{\eta_G} P_E \tag{4.28}$$

Knowing the engine break power P_B (kW), it is possible to calculate the fuel consumption rate $\dot{m}_f$ (kg/h) through the specific fuel consumption SFC (kg/kW/h):

$$SFC = \frac{\dot{m}_f}{P_B} \tag{4.29}$$

In this study, the global propulsion efficiency η_G is taken equal to 0,5 as it is the average value observed for inland vessels (Hidouche et al., 2015). However, this estimation can be more accurate if each performance ratio is detailed, especially the propeller efficiency, but this implementation needs other parameters (propeller characteristics, hull shape,...).

4.3.2. Specific fuel consumption

The specific fuel consumption is a measure of fuel efficiency used for comparing different engines regardless of their power. The specific fuel consumption model used in this study has been developed within the framework of Cerema's Naval research program and is described in greater detail in Hidouche et al. (2015). This model uses a single parameter as input (engines power ratio P_B/P_{max}) to calculate the specific fuel consumption of the ship SFC. The calculation is based on a regression analysis of specific fuel consumption curves against power ratio. The specific fuel consumption data from recent and representative engine were collected from the manufacturers (mainly Cummins, MAN, Caterpillar and Wartsila). Furthermore, the declination of the model by engines power class and the split of the model in two zones of regression (power regression for zone 1 and polynomial regression for zone 2) provide a better accuracy to this model. Figure 4.4 shows an example of the model regression performed in this model and Table 4.1 summarizes the equations of the model and the error range.

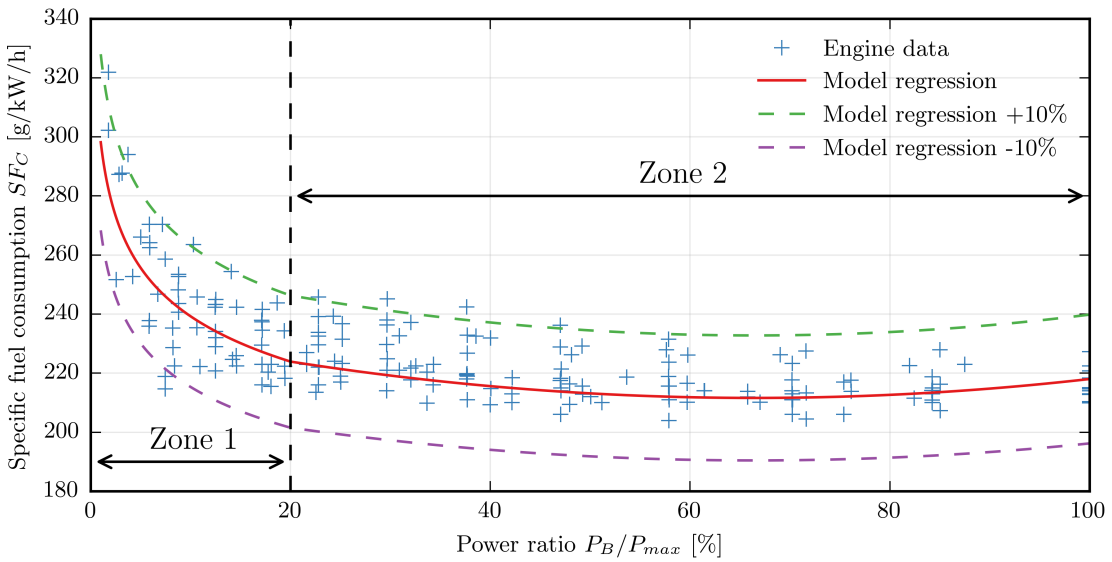

Figure 4.4.: *Specific fuel consumption for 1000kW-2000kW range; model curve and engine data*
Source: *adapted from Hidouche et al. (2015)*

Table 4.1.: *Specific fuel consumption model equations and errors*

$\mathbf{P_{max}}$ [kW]	$\mathbf{X = P_B/P_{max}}$ [%]	$\mathbf{SFC = f(X)}$ [g/kW/h]	**Error** [%]
100-300	$0-20$	$398.89(X)^{-0.1987}+8.945$	10
	$20-100$	$242.51-0.810(X)+0.0065(X)^2$	7
300-500	$0-20$	$342.077(X)^{-0.1361}$	10
	$20-100$	$237.84-0.5957(X)+0.0040(X)^2$	7
500-1000	$0-20$	$327.708(X)^{-0.1262}+1.984$	15
	$20-100$	$230.192-0.4496(X)+0.0033(X)^2$	10
1000-2000	$0-20$	$296.346(X)^{-0.0963}-1.06$	10
	$20-100$	$236.786-0.7577(X)+0.0064(X)^2$	10
2000-10000	$0-30$	$265.583(X)^{-0.0570}-1.743$	7
	$30-100$	$240.204-0.9639(X)+0.0064(X)^2$	5
>10000	$0-30$	$218.92(X)^{-0.0570}-1.4368$	-
	$30-100$	$198-0.7945(X)+0.0053(X)^2$	5

4.4. Hydraulic model

As described in section 4.1, in order to define the operating conditions used as an input in the optimization algorithm, a 2D hydraulic model has been developed within the framework of Cerema's Naval research program and is described in greater detail in Huybrechts et al. (2015). This model covers the Seine river between Andresy and Poses and is divided in four river reaches to account for hydraulic discontinuities and weirs:

- between Chatou and Andrésy (reach 1);
- between Andrésy and Méricourt (reach 2);
- between Méricourt and Notre Dame La Garenne (reach 3);
- between Notre Dame La Garenne and Poses (reach 4).

This area was chosen for the case study because it is one of the main French river route for good transport and the model ship used for the ship resistance model corresponds to two ships operating in this area (Bosphore and Oural). Figure 4.5 illustrates the part of Seine river modelled and the four reaches.

Figure 4.5.: *Seine river between Chatou and Poses*
Source: *Huybrechts et al. (2015)*

Seine river flow is modelled with Telemac2D software, which solves the Saint-Venant equations using the finite-element method and a computation mesh of triangular elements (Hervouet, 2007). Distance between the mesh nodes varies between 3 m (typically in ship locks) and 12.5 m (typically in the middle of the reach). For each reach, measured discharge is imposed at the upstream boundaries and measured water level is set for the downstream boundary. The measured dam discharge and water level are extracted from Banque Hydro[1]. Friction coefficient is calibrated using measured water level at the upstream boundary. The data used for this model is the December 2012 river flood. The average observed discharge for Seine river between 2008 and 2015 is $480\ m^3/s$. In December 2012, the river flood started with low discharge ($< 200\ m^3/s$) during the first few days, then a first increase in discharge was observed (up to $500\ m^3/s$) and a final surge in discharge (up to $950 - 1000\ m^3/s$) occurred near the end of then event. Therefore, this event allows to simulate Seine river hydrodynamic conditions for three characteristic discharges (200, 500 and 900 m^3/s). Futhermore, for this event, measured data are available at every weirs for the validation of the model. Figure 4.6 shows a plot the measured discharge at Chatou's dam during this event.

[1] `http://www.hydro.eaufrance.fr/`

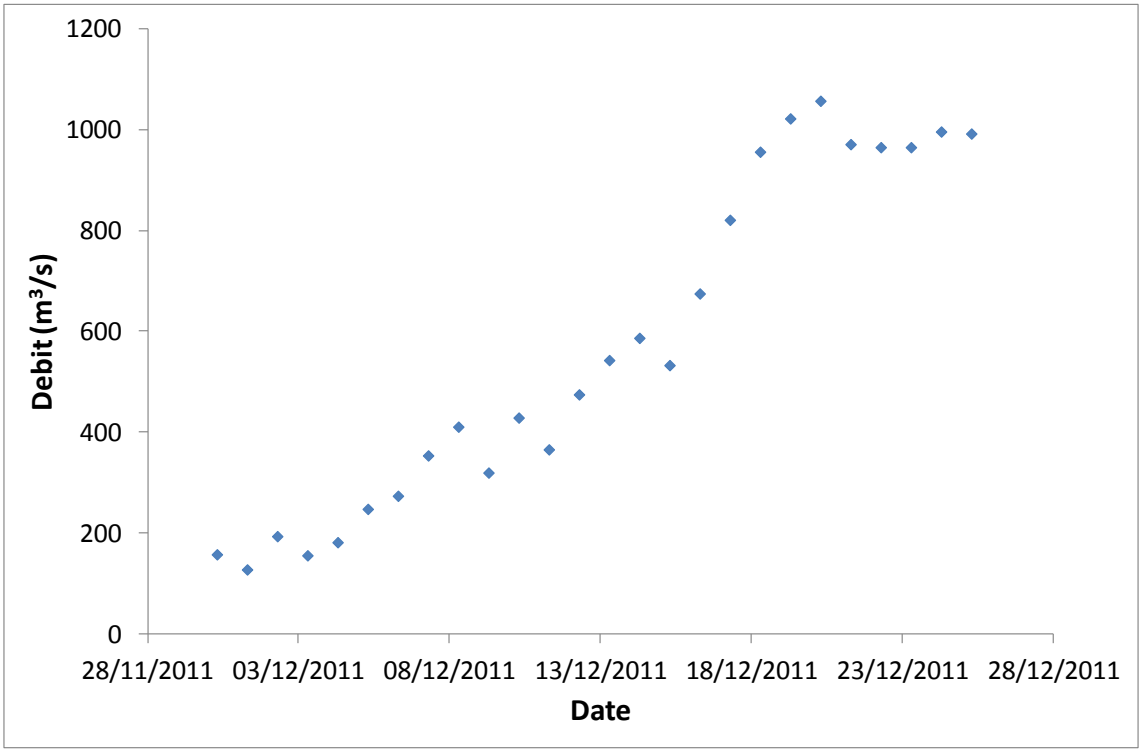

Figure 4.6.: *Measured discharge at Chatou's dam during December 2012 river flood*
Source: *Huybrechts et al. (2015)*

The model accuracy is evaluated by calculating the relative mean absolute error $RMAE$ (Sutherland et al., 2004):

$$RMAE = \frac{\langle |X - Y| \rangle}{\langle |X| \rangle} \tag{4.30}$$

where X is a set of N observed data values $[x_1, ..., x_N]$, Y is a set of N predicted values $[y_1, ..., y_N]$ and $\langle |X| \rangle = \frac{1}{N} \sum_{i=1}^{N} |x_i|$ is the mean absolute value. Sutherland et al. (2004) defines five quality levels for the $RMAE$: excellent ($RMAE < 0.2$), good ($0.2 < RMAE < 0.4$), reasonable ($0.4 < RMAE < 0.7$), poor ($0.7 < RMAE < 0.1$) and bad ($RMAE > 0.1$). The bottom friction coefficient is chosen in order to minimize the $RMAE$ critieria.

Table 4.2 gives the $RMAE$ calculated values for each reach and Figure 4.7 shows the evolution of modelled water level near Chatou.

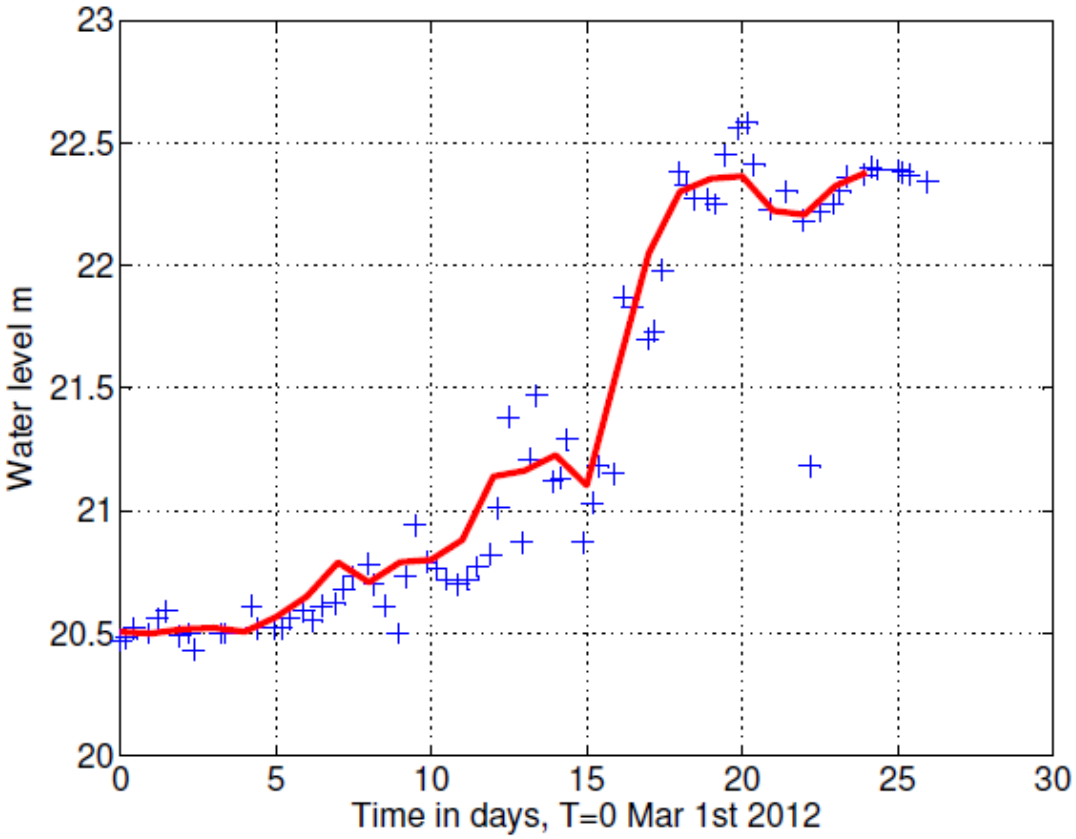

Figure 4.7.: *Modelled water level downstream Chatou's dam*
Source: *taken from Huybrechts et al. (2015)*

Table 4.2.: *Calculated RMAE for the four reaches*

Reach	**RMAE** [-]
1	0.018
2	0.009
1	0.011
1	0.020

Table 4.2 and Figure 4.7 show that the hydraulic model gives accurate results. However, the following limitations can be listed:

- bridge peers are not taken into account in the model;
- the model has only been validated for water level predictions and flow velocity measurement are required to validate the current prediction;
- an estuarian model should be developed between Le Havre and Rouen.

4.5. Operating conditions

The itinerary on which the ship speed is optimized is characterized by a set of parameters called operating condition. These parameters are the channel width W, the water depth H and the current velocity U and are required in order to calculate the ship resistance with the model described in section 4.1. From the results of the hydraulic model described in section 4.4, water depth H, current velocity U and river width W are extracted every 10 m on the vessel trajectory. The itinerary is then approximated by n legs of length $l_i = 10m$ and characterized by the parameters $(H_i, U_i, W_i)_{1 \leq i \leq n}$. This itinerary is then further simplified for the optimization process by merging the n fine legs into N coarser legs LC_i of length L_i, by using the Piecewise Aggregate Approximation technique (Keogh et al., 2001).

If $X = [x_1, ..., x_n]_{1 \leq i \leq n}$ is the list of parameters (x denotes either the water depth H, the current velocity U or the river width W) extracted every 10 m, the data $Y = [y_1, ..., y_N]_{1 \leq i \leq N}$ characterizing the N coarser legs is calculated as follows:

$$y_i = \frac{N}{n} \sum_{j=\frac{n}{N}(i-1)+1}^{\frac{n}{N}i} x_j \tag{4.31}$$

4.6. Optimization algorithm

The optimization algorithm minimizes the global fuel consumption for the itinerary by finding the optimal speed at which the ship should sail on each leg.

4.6.1. Optimization problem formulation

The quantity of fuel FC_i (kg) consumed by the ship on leg LC_i of length L_i (km) is given by:

$$FC_i = \dot{m}_{fi} \times \Delta T_i = SFC_i \times P_{Bi} \times \Delta T_i \tag{4.32}$$

where ΔT_i (h) is the time necessary for the ship to cover the distance L_i.

It is assumed that ship sails at constant speed V_i on leg LC_i, therefore $\Delta T_i = \frac{L_i}{V_i}$. Equation (4.28) also gives $P_B = \frac{1}{\eta_H \times \eta_S \times \eta_S} P_E = \frac{R_{Ti} \times V_i}{\eta_H \times \eta_S \times \eta_S}$. As a result the quantity of fuel FC_i can be written:

$$FC_i = \frac{SFC_i \times R_{Ti} \times L_i}{\eta_H \times \eta_S \times \eta_S} \tag{4.33}$$

The total fuel consumption FC_T on the itinerary is then given by:

$$FC_T = \sum_{i=0}^{N} FC_i \tag{4.34}$$

The expression FC_T thus defined is a non linear continuous function of variable $\boldsymbol{V} = (V_0, ..., V_N)$. The formulation of the optimization problem can then be written as:

$$\begin{aligned} \underset{V}{\textbf{minimize}} \quad & FC_T(\boldsymbol{V}) \\ \textbf{such that} \quad & \sum_{i=0}^{N} \frac{L_i}{V_i} \leq T_{max} \\ & V_i > 0 \ , \ i = 0, ..., n \end{aligned} \tag{4.35}$$

The first constraint set a maximum travel duration and the other constraints are only set to restrict the speed values to positive values. This optimization problem is a non-linear optimization problem with nonlinear constraints. Several methods are available to solve this type of optimization problem such as penalty function method, gradient projection method, feasible directions method and multiplier methods. However, these methods often performs better for linear constraints. For

this reason, the optimization problem is reformulated as follows:

$$\begin{aligned} \underset{V}{\textbf{minimize}} \quad & FC_T^*(\boldsymbol{X}) \\ \textbf{such that} \quad & \sum_{i=0}^{N} L_i \times X_i \leq T_{max} \\ & X_i > 0 \ , \ i = 0, ..., n \end{aligned} \tag{4.36}$$

where $\boldsymbol{X} = \frac{\mathbf{1}}{\boldsymbol{V}} = (\frac{1}{V_0}, ..., \frac{1}{V_N})$ and $FC_T^*(\boldsymbol{X}) = FC_T(\frac{\mathbf{1}}{\boldsymbol{X}}) = FC_T(\boldsymbol{V})$. With this formulation, the problem is now a non linear optimization problem with linear constraints in X.

4.6.2. Non-linear optimization techniques

This section describes the non-linear optimization techniques which have been tested to solve the optimization problem. For simplification purpose, in this section, the optimization problem is rewritten as:

$$\begin{aligned} \underset{\boldsymbol{X}}{\textbf{minimize}} \quad & f(\boldsymbol{X}) \\ \textbf{such that} \quad & g_i(\boldsymbol{X}) = \sum_{i=1}^{n_c} a_{ji} X_i - b_j \geq 0, \ i = 0, ..., n_c \end{aligned} \tag{4.37}$$

where f is the function to minimize and g_i are the n_c linear constraints of the optimization problem. In vector form, the constraints can be written as:

$$g_i(\boldsymbol{X}) = \boldsymbol{a_j}^T \boldsymbol{X} - b_j \geq 0 \tag{4.38}$$

This method has been programmed in Python 3 language.

Penalty function method

The idea behind the penalty method is to transform the constrained optimization problem to an unconstrained one by adding a penalty terms to the objective function. This method was first introduced by Zangwill (1967) and Pietrzykowski (1969). Three types of penalty functions φ can be found: exterior, interior and extended interior penalty functions. In every case, the constrained optimization problem in Equation (4.37) is replaced by the following unconstrained optimiza-

tion problem:

$$\begin{aligned} &\underset{\boldsymbol{X}}{\textbf{minimize}} \qquad \phi(\boldsymbol{X}, r) = f(\boldsymbol{X}) + r \sum_{i=1}^{n_c} \varphi(h_i(\boldsymbol{X})) \\ &r = r_1, r_2, ..., \quad r_i \to 0 \; (interior\ penalty) \; or \; r_i \to \infty \; (exterior\ penalty) \end{aligned} \tag{4.39}$$

where r is a positive multiplier controlling the amplitude of the penalty. The minimization is started with a small value of r and is then gradually increased. A typical value of r_{i+1}/r_i is 5. In the exterior penalty function method, the penalties are applied only in the exterior of the feasible domain whereas in the interior penalty function method, the penalty term prevent the solution from leaving the feasible region. However, when using one of those two techniques, it is possible that the temporary solution will jump either inside or outside of the feasible domain (often due to the use of approximations) causing the iterative process to fail. The use of a combination of interior and exterior penalty function allows to avoid such problem. An example of such functions is the quadratic extended interior penalty function of Haftka and Starnes (1975):

$$\phi(a) = \begin{cases} \dfrac{1}{a} & \text{if } a \geq a_0 \\ \dfrac{1}{a_0}(3 - 3(\dfrac{a}{a_0}) + (\dfrac{a}{a_0})^2) & \text{if } a < a_0 \end{cases} \tag{4.40}$$

where a_0 is a parameter defining the boundary between the interior and exterior parts of the penalty terms. Usually a_0 is taken as $a_0 = Cr^{1/2}$ where C is a constant. Figure 4.8 shows an application of the extended interior penalty method for the objective function $f = 0.5x$ subject to $x - 4 \geq 0$.

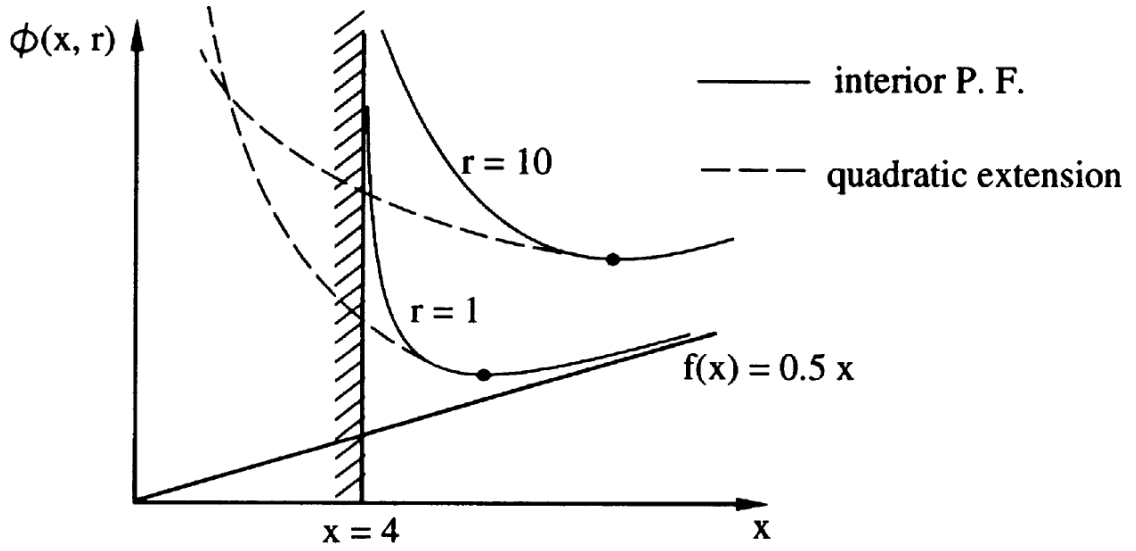

Figure 4.8.: *Illustration of extended interior penalty function method*
Source: *taken from Haftka and Gürdal (2012)*

An approximation of the solution of Equation (4.37) is found by iteratively finding the solution of Equation (4.39) for a sequence of values of r. The following convergence criteria is used to stop the iterative process:

$$\left| \frac{f(\boldsymbol{X^{k+1}}) - (\boldsymbol{X^{k}})}{(\boldsymbol{X^{k+1}})} \right| \leq \varepsilon \tag{4.41}$$

where $\varepsilon = 0.001$. This method has been programmed in Python 3 language.

Gradient projection method

Rosens gradient projection method Rosen (1960) consists into projecting the search direction into the subspace tangent to the active constraints. For a position vector $\boldsymbol{X}$, the equations of active constraints can be written in matrix form:

$$\boldsymbol{g_a} = \boldsymbol{N}^T \boldsymbol{X} - \boldsymbol{b} = 0 \tag{4.42}$$

where $\boldsymbol{g_a}$ is the vector of active constraints and the columns of the matrix $\boldsymbol{N}$ are the gradients of these constraints. This method is based on the assumption that $\boldsymbol{X}$ lies in the subspace tangent to the active constraints. Therefore if:

$$\boldsymbol{X_{i+1}} = \boldsymbol{X_i} + \alpha \boldsymbol{s} \tag{4.43}$$

and both $\boldsymbol{X_{i+1}}$ and $\boldsymbol{X_i}$ satisfy Equation (4.42), then:

$$\boldsymbol{N}^T\boldsymbol{s} = 0 \tag{4.44}$$

In order to find the steepest descent direction satisfying Equation (4.44), the following optimization problem can be solved:

$$\begin{aligned} &\underset{\boldsymbol{X}}{\textbf{minimize}} && \boldsymbol{s}\nabla f \\ &\textbf{such that} && \boldsymbol{N}^T\boldsymbol{s} = 0 \\ &\textbf{and} && \boldsymbol{s}^T\boldsymbol{s} = 1 \end{aligned} \tag{4.45}$$

This problem can be solved by using Lagrange multipliers $\boldsymbol{\lambda}$ and μ, and it is shown that:

$$\boldsymbol{s} = \frac{1}{2\mu}[\boldsymbol{I} - \boldsymbol{N}(\boldsymbol{N}^T\boldsymbol{N})^{-1}\boldsymbol{N}^T]\nabla f = \frac{1}{2\mu}\boldsymbol{P}\nabla f \tag{4.46}$$

where $\boldsymbol{P}$ is the projection matrix projecting a vector into the subspace tangent to the active constraints. It can be shown that Haftka and Gürdal (2012):

$$\boldsymbol{P} = \boldsymbol{Q_2^T}\boldsymbol{Q_2} \tag{4.47}$$

where $\boldsymbol{Q_2}$ is the matrix containing the last $n - r$ rows of the $\boldsymbol{Q}$ factor in the QR factorization of $\boldsymbol{N}$. Once the descent direction $\boldsymbol{s}$ is obtained from Equation (4.46), two cases can be distinguished. If $\boldsymbol{s} = \boldsymbol{0}$, the Kuhn-Tucker conditions may be satisfied and the Lagrange multipliers are then calculated. If all the components of $\boldsymbol{\lambda}$ are positive, the Kuhn-Tucker conditions are satisfied and the optimization algorithm is stopped. Otherwise, if some Lagrange multipliers are negative, it indicates that no progress is possible with the current set of active constraints. The constraints associated with the negative multipliers are then removed and the calculation of $\boldsymbol{P}$ and $\boldsymbol{s}$ is repeated. This process is iterated until all the Lagrange multipliers become positive or until a non-zero descent direction $\boldsymbol{s}$ is found.

Once a non-zero descent direction $\boldsymbol{s}$ has been found, a one dimensional search is carried out to determine the value of α in eq. (4.43). There is however an upper limit on α set by the inactive constraints. By substituting $\boldsymbol{X_{i+1}} = \boldsymbol{X_i} + \alpha\boldsymbol{s}$ in Equation (4.38), the following equation is obtained:

$$\alpha \geq -(\boldsymbol{a_j^T}\boldsymbol{X_i} - b_j)/\boldsymbol{a_j^T}\boldsymbol{s} = -g_j(\boldsymbol{X_i})/\boldsymbol{a_j^T}\boldsymbol{s} \tag{4.48}$$

This equation is valid only if $\boldsymbol{a_j^T s} < 0$, otherwise there is no upper limit on α set by the j^{th} constraint. The upper limit α_{up} is then calculated by:

$$\alpha_{up} = \min_{\alpha_j > 0, j \notin I_A} \alpha_j \tag{4.49}$$

Once the step α is obtained, the solution $\boldsymbol{X_{i+1}}$ is calculated with Equation (4.43) and the set of active constraints is updated before undertaking the next move. This iterative process is stopped either when the Kuhn-Tucker conditions are satisfied or the stopping criteria defined in Equation (4.41) is met. This method has been programmed in Python 3 language.

Feasible direction method

The feasible direction method Zoutendijk (1960) has the opposite approach to that of the gradient projection method. In this method, instead of following the constraints boundaries, the solution is kept as far as possible from them. This method is usually started at the boundary of the feasible domain. If no constraints are active at the start, unconstrained minimization techniques are used until one of the constraint boundary is reached. If $\boldsymbol{X_i}$ is on the boundary of the feasible domain, a direction $\boldsymbol{s}$ keeping the solution in the feasible domain and improving the objective function is searched. $\boldsymbol{s}$ is called a feasible direction if at least a small step can be taken along it that does not leave the feasible domain. This condition is satisfied if:

$$\boldsymbol{s}^T \nabla g_j > 0 \; j \in I_A \tag{4.50}$$

where I_A is the set of active constraints at position $\boldsymbol{X_i}$. Furthermore, $\boldsymbol{s}$ is called a usable direction at position $\boldsymbol{X_i}$ if it satisfies:

$$\boldsymbol{s}^T \nabla f = \boldsymbol{s}^T \nabla \boldsymbol{g} < 0 \tag{4.51}$$

If Equation (4.51) is satisfied, $\boldsymbol{s}$ is a direction reducing the objective function.

Equation (4.50) and Equation (4.51) define two criteria for selecting a direction: keeping away from constraint boundary and improving the objective function. A compromise between these two criteria can be defined with the following maxi-

mization problem:

$$\begin{aligned} \underset{\boldsymbol{X}}{\textbf{maximize}} \quad & \beta \\ \textbf{such that} \quad & -\boldsymbol{s}^T \nabla g_j + \theta_j \beta \geq 0,\ j \in I_A, \\ & \boldsymbol{s}^T \nabla f + \beta \geq 0 \\ & |s_i| \geq 1 \end{aligned} \tag{4.52}$$

where θ_j are "push-off" factors whose magnitude determines how far $\boldsymbol{X_i}$ will move from the boundary. A value of $\theta_j = 0$ will result in a move tangent to the j^{th} constraint (appropriate for linear constraint) and a large value of θ_j will result in a large angle between the search direction $\boldsymbol{s}$ and the constraint boundary (appropriate for highly non linear constraint). The optmization problem thus defined is linear and is solved with simplex algorithm implemented in the Python package Scipy (Jones et al., 2001).

Once a search direction has been found by solving Equation (4.52), a one dimensional search is carried out to determine the step value in the same way described in Section 4.6.2. If at the end of the step no constraints are active, unconstrained minimization techniques are used until one of the constraint boundary is reached and the next iteration is started. This iterative process is stopped when the stopping criteria defined in Equation (4.41) is met. This method has been programmed in Python 3 language.

Sequential quadratic programming method

Sequential quadratic programming (SQP) is a class of algorithms for solving nonlinear optimization problems (Nocedal and Wright, 2006). These methods can be viewed as an extension of Newton's method for unconstrained optimization. At each iteration, a quadratic subproblem is generated by replacing the objective function with a quadratic approximation and the constraint functions by linear approximations. The solution of this subproblem is used to form a search direction for a line search procedure. This method is implemented in the Python package Scipy (Jones et al., 2001). Further details about theses methods can be found in Nocedal and Wright (2006).

4.7. Summary

EcoNav is based on an optimization algorithm minimizing the fuel consumption by finding the optimal speed profile for a given itinerary (operating conditions) under specified constraints (maximum travel duration). The optimization problem described in this chapter is non linear and four non linear optimization techniques allowing to solve this problem were presented. The fuel consumption is evaluated by a fuel consumption model based on a specific fuel consumption empirical model developed by Hidouche et al. (2015). This model uses the ship resistance as an input which is calculated by the ship resistance numerical model presented in chapter 2. However, the required computational time for this model is expensive, and the optimization algorithm requires many function calls before converging. To avoid expensive CFD simulations, a surrogate model (meta-modelling) is built from sampled data obtained with the numerical model. Five popular surrogate model techniques are proposed and described in this chapter. In this PhD, the experimental results from the University of Liege are used to build the response surface model (RSM) as the number of experimental samples available are greater than those of CFD simulations. In the long term, it is planned to replace the experimental data with numerical results from the ship resistance model as this model can be used for any restricted waterway configuration and any inland vessel to calculate accurate results of ship resistance. Finally, the operating conditions are defined by the parameters describing the hydrodynamics conditions in which the ship will sail on the itinerary. These conditions are the channel width W, the water depth H and the current velocity U. The last two quantities are predicted by using a 2D hydraulic model (Telemac2D V7P0). The methods applicable for the surrogate model and the optimization algorithm, described in this chapter, are compared in chapter 6 to determine which ones are the most adapted for EcoNav.

CHAPTER 5

Validation of EcoNav modules and application to Oural vessel on Seine river

The speed optimization model developped in this PhD and its modules are described in chapter 4. Several methods are available for the surrogate model and the optimization module. In this chapter, the surrogate model techniques and optimization methods presented in chapter 4 are compared and analysed to determine which ones are the most suited for EcoNav. Once these methods have been selected, the speed optimization model is used to simulate a real case: the itinerary of the self-propelled ship Oural on river Seine, between the locks of Chatou and Poses. The effect of the ship trajectory and travel duration on fuel consumption is also investigated.

5.1. Comparison of surrogate model techniques for ship resistance prediction

5.1.1. Polynomial regression model

Figure 5.1 shows the comparison between the experimental data (markers) and the surrogate model (lines) obtained with the polynomial regression model. Figure 5.2

shows the iso-contours of ship resistance in function of W/B and H/T at four different ship speeds (V=0.2, 0.4, 0.6 and 0.8 m/s) calculated with this surrogate model.

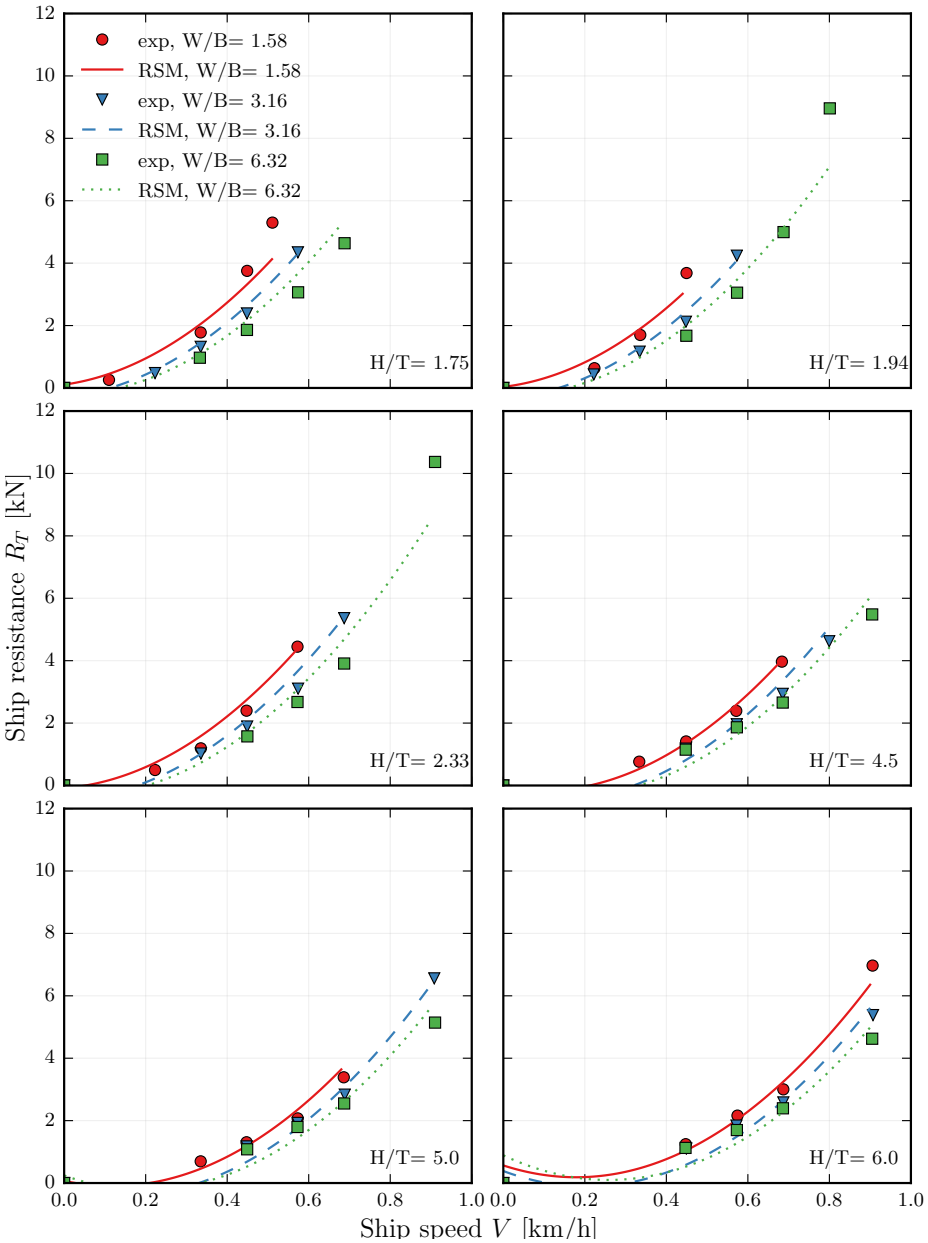

Figure 5.1.: *Comparison between experimental data and surrogate model output for the polynomial regression model.*

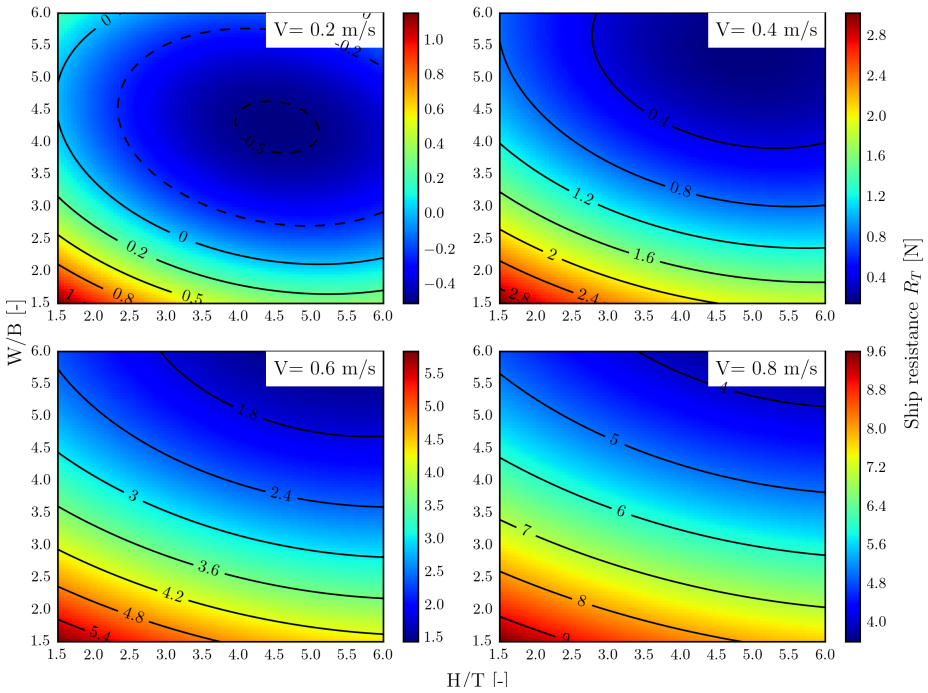

Figure 5.2.: *Iso-contours of ship resistance in function of W/B and H/T ratios at V=0.2, 0.4, 0.6 and 0.8 m/s calculated with the polynomial regression method.*

Figure 5.1 shows that overall, the surrogate model results are in good agreement with the experimental results. However, some discrepancies can be seen for low speed ($V \leq 0.2\ m/s$) where the surrogate model predicts a negative resistance. The error between the surrogate model predictions also tend to increase for high velocities ($V \geq 0.7\ m/s$) and the most restricted configurations. The mean square error computed for this model is $MSE = 0.20$. Figure 5.2 shows that the evolution of the iso-contours of ship resistance is fairly regular, which is mainly due to the polynomial regression. The iso-contours calculated for a speed of 0.2 m/s show that the negative resistance values cover a wide area of plot. Figure 5.2 also shows that the increase in ship resistance is more influenced by H/T parameter than W/B. Indeed, the H/T component of the ship resistance gradient (perpendicular to the iso-contour) is more important than the W/B component. This result is in agreement with the conclusion of the study on the restriction parameter influence ship resistance presented in chapter 3.

5.1.2. Moving least square model

Figure 5.3 shows the comparison between the experimental data (markers) and the surrogate model (lines) obtained with the MLS method. Figure 5.2 shows the iso-contours of ship resistance in function of W/B and H/T at four different ship speeds (V=0.2, 0.4, 0.6 and 0.8 m/s) calculated with this surrogate model.

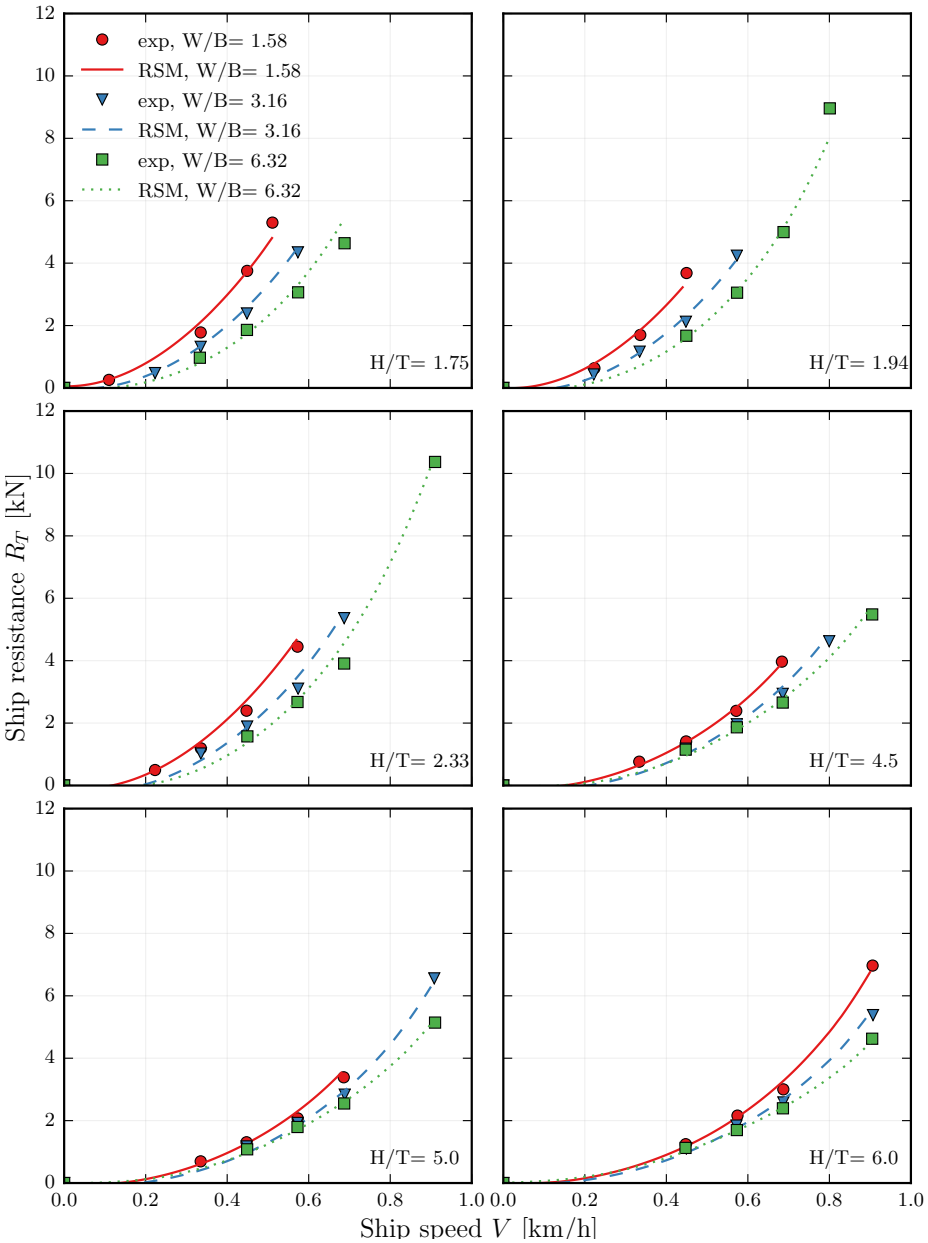

Figure 5.3.: *Comparison between experimental data and surrogate model output for the polynomial regression model.*

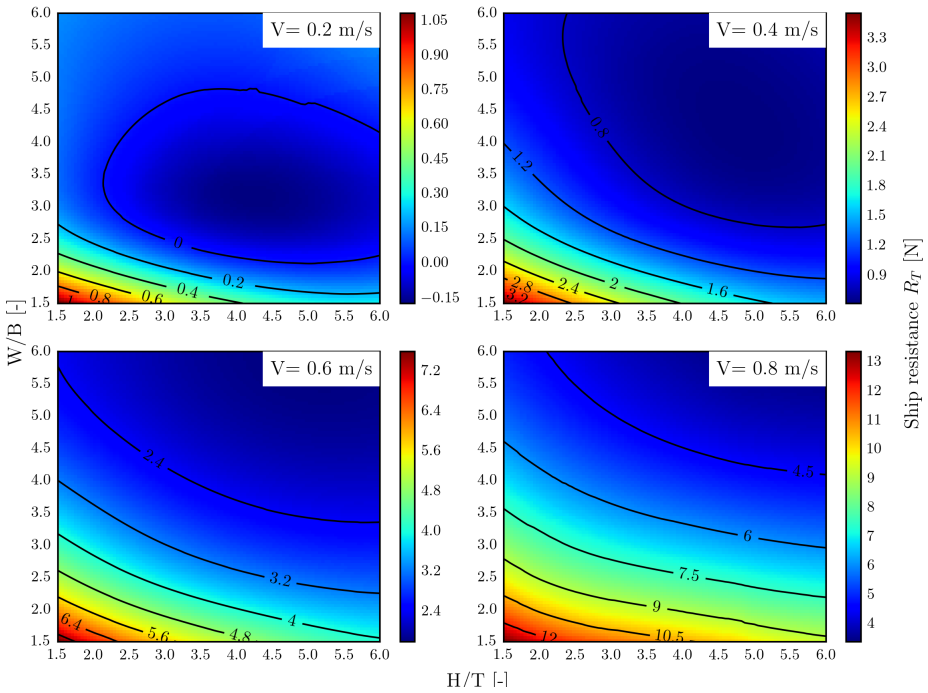

Figure 5.4.: *Iso-contours of ship resistance in function of W/B and H/T ratios at V=0.2, 0.4, 0.6 and 0.8 m/s calculated with the polynomial regression method.*

Figure 5.3 shows that the MLS method gives more accurate results than the PR method: for low speed ($V \leq 0.2\ m/s$) the surrogate model predicts fewer negative resistance values, and high velocities ($V \geq 0.7\ m/s$) the predicted values with the MLS method are closer to the experimental data. The mean square error calculated with this method is $MSE = 0.04$ which is five times smaller that the one calculated with the PR method. Figure 5.4 shows that the evolution of the iso-contours of ship resistance is also regular and that the negative resistance values obtained for a speed of 0.2 m/s cover a smaller area of the plot than in Figure 5.2. Moreover, the maximum amplitude of the negative values (0.15 N) is significantly lower than the maximum negative amplitude obtained with the PR model (0.5 N). Finally, the same conclusion drawn for the ship resistance gradient with the PR method applies with the MLS method. The main drawback of this method is its high computational cost making it difficult to use for an optimization process requiring many function evaluations.

5.1.3. Kriging model

Figure 5.5 shows the comparison between the experimental data (markers) and the surrogate model (lines) obtained with the Kriging method. Figure 5.6 shows the iso-contours of ship resistance in function of W/B and H/T at four different ship speeds (V=0.2, 0.4, 0.6 and 0.8 m/s) calculated with this surrogate model.

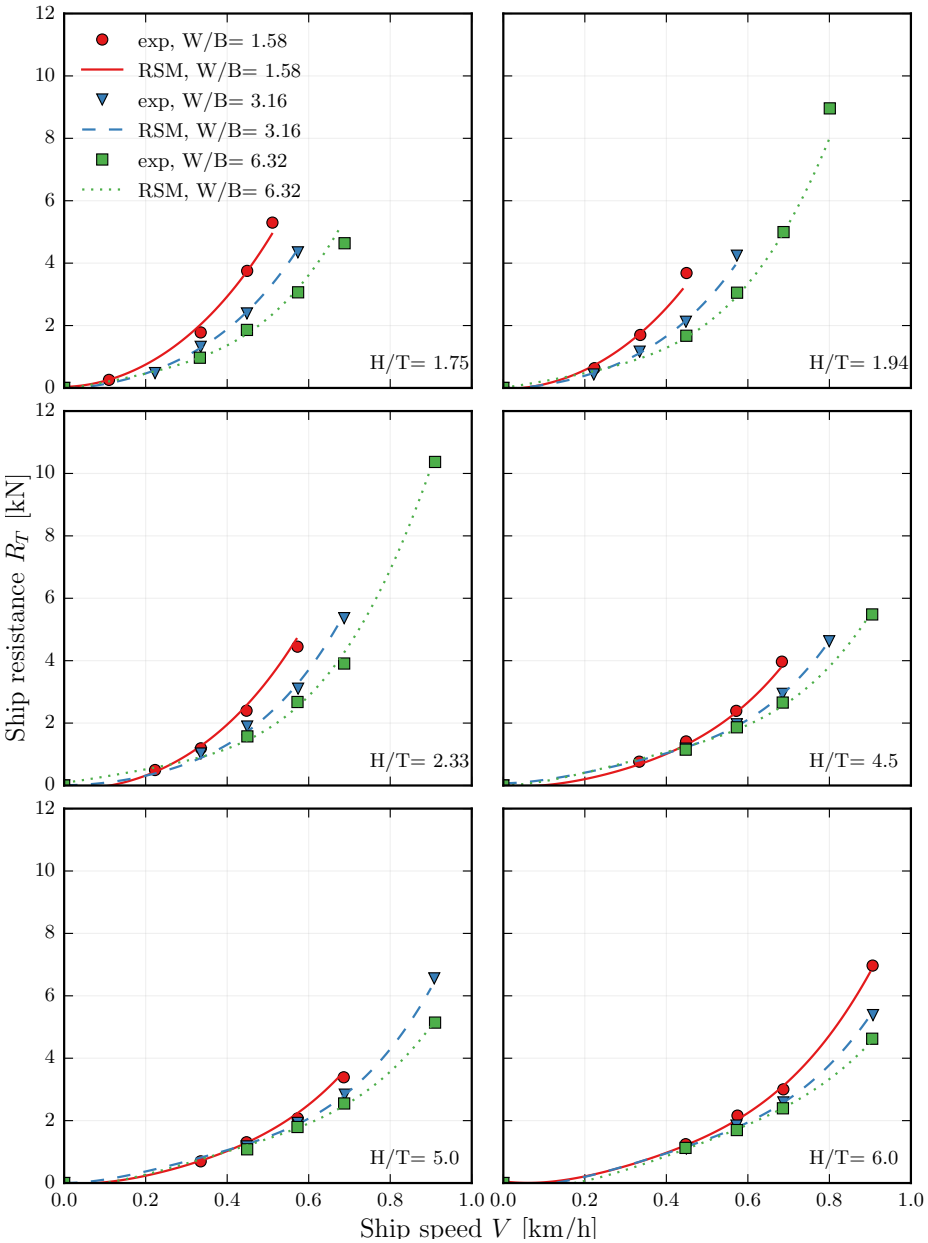

Figure 5.5.: *Comparison between experimental data and surrogate model output for Kriging method.*

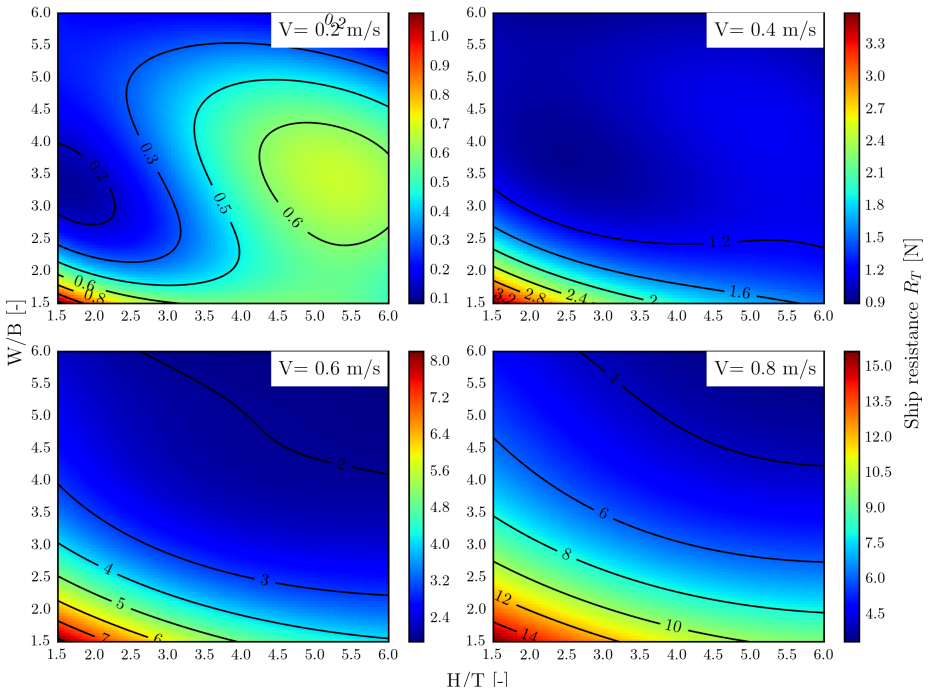

Figure 5.6.: *Iso-contours of ship resistance in function of W/B and H/T ratios at V=0.2, 0.4, 0.6 and 0.8 m/s calculated with the Kriging method.*

Figure 5.5 shows that the Kriging method also gives more accurate results than the PR method. This method also predicts less negative ship resistance values than the MLS method: with the Kriging model, for a speed of $V = 0.2\ m/s$ no negative values are calculated which is not the case with the MLS method. This can be verified in Figure 5.6 where the heatmap produced for the this speed shows that the minimum calculated resistance is $R_T = +0.1N$. The mean square error calculated with this method is $MSE = 0.03$ which is slighly lower than the one calculated for the MLS method (0.04). The iso-contours of ship resistance presented in Figure 5.6 also show a very regular behaviour except for the speed $V = 0.2\ m/s$. Indeed, for this speed, at equal width restriction (W/B ratio fixed), the ship resistance increases with H/T ratio. However, this discrepancy should not impact the optimization process as it only concerns very low speeds. Finally, the same conclusion drawn for the ship resistance gradient with the PR method apply with the Kriging method. Overall, this method is more accurate than the MLS method and less computationally expensive.

5.1.4. SVR model

Figure 5.7 shows the comparison between the experimental data (markers) and the surrogate model (lines) obtained with the SVR method. Figure 5.8 shows the iso-contours of ship resistance in function of W/B and H/T at four different ship speeds (V=0.2, 0.4, 0.6 and 0.8 m/s) calculated with this surrogate model.

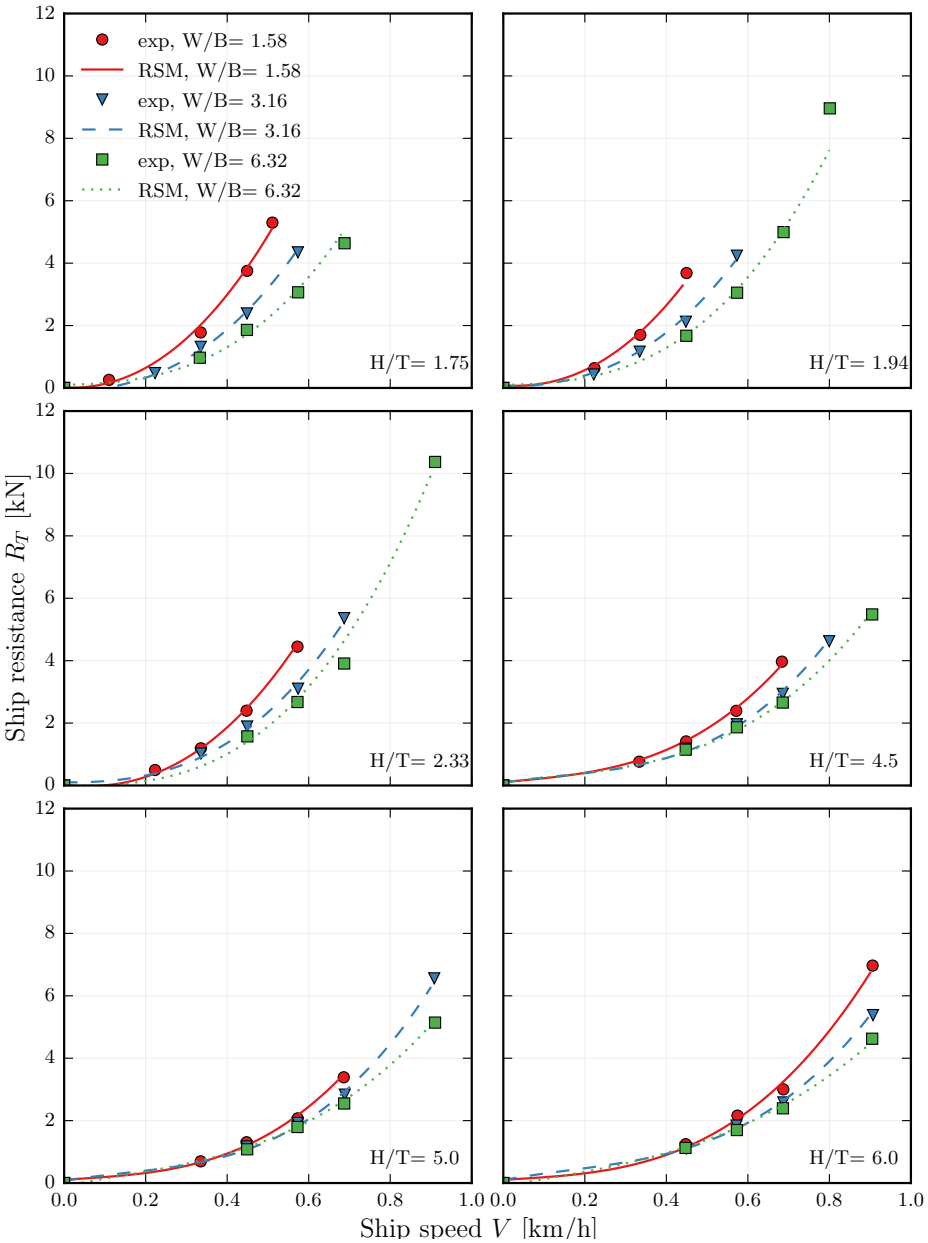

Figure 5.7.: *Comparison between experimental data and surrogate model output for SVR method.*

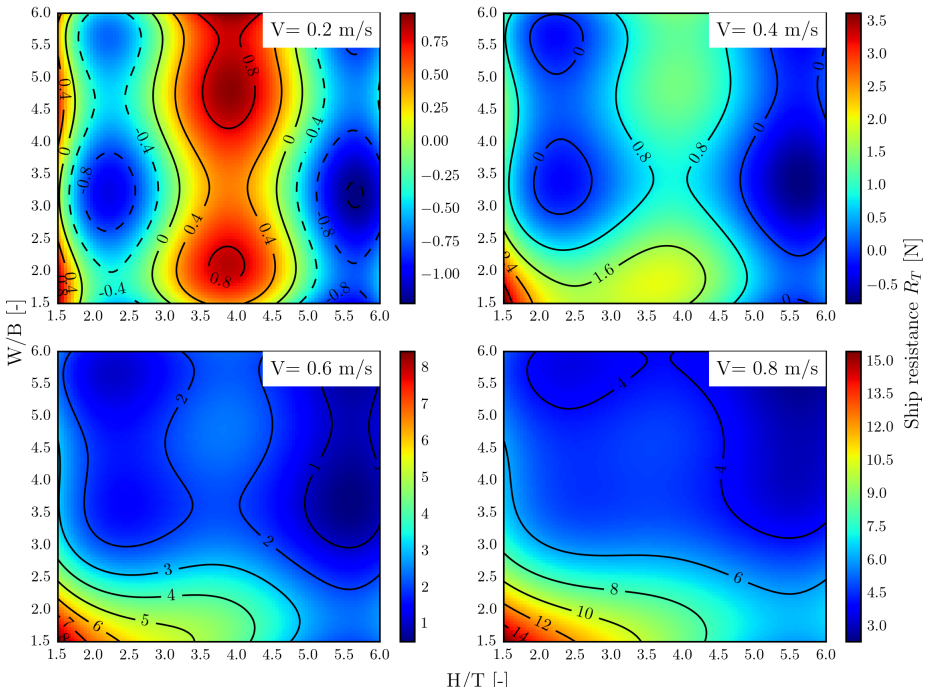

Figure 5.8.: *Iso-contours of ship resistance in function of W/B and H/T ratios at V=0.2, 0.4, 0.6 and 0.8 m/s calculated with the SVR method.*

Figure 5.7 shows that the SVR method also gives accurate results for the prediction of ship resistance. The mean square error calculated for this method is $MSE = 0.04$. It is the same value as the one obtained for MLS method and slightly greater than the one obtained with the Kriging method (0.03). However, the iso-contours of approximated ship resistance presented in Figure 5.8 are far more irregular than those plotted for the Kriging and MLS method. This behavior is not physical and therefore this method seems less suited than MLS or Kriging.

5.1.5. RBF model

Figure 5.9 shows the comparison between the experimental data (markers) and the surrogate model (lines) obtained with the RBF method. Figure 5.10 shows the iso-contours of ship resistance in function of W/B and H/T at four different ship speeds (V=0.2, 0.4, 0.6 and 0.8 m/s) calculated with this surrogate model.

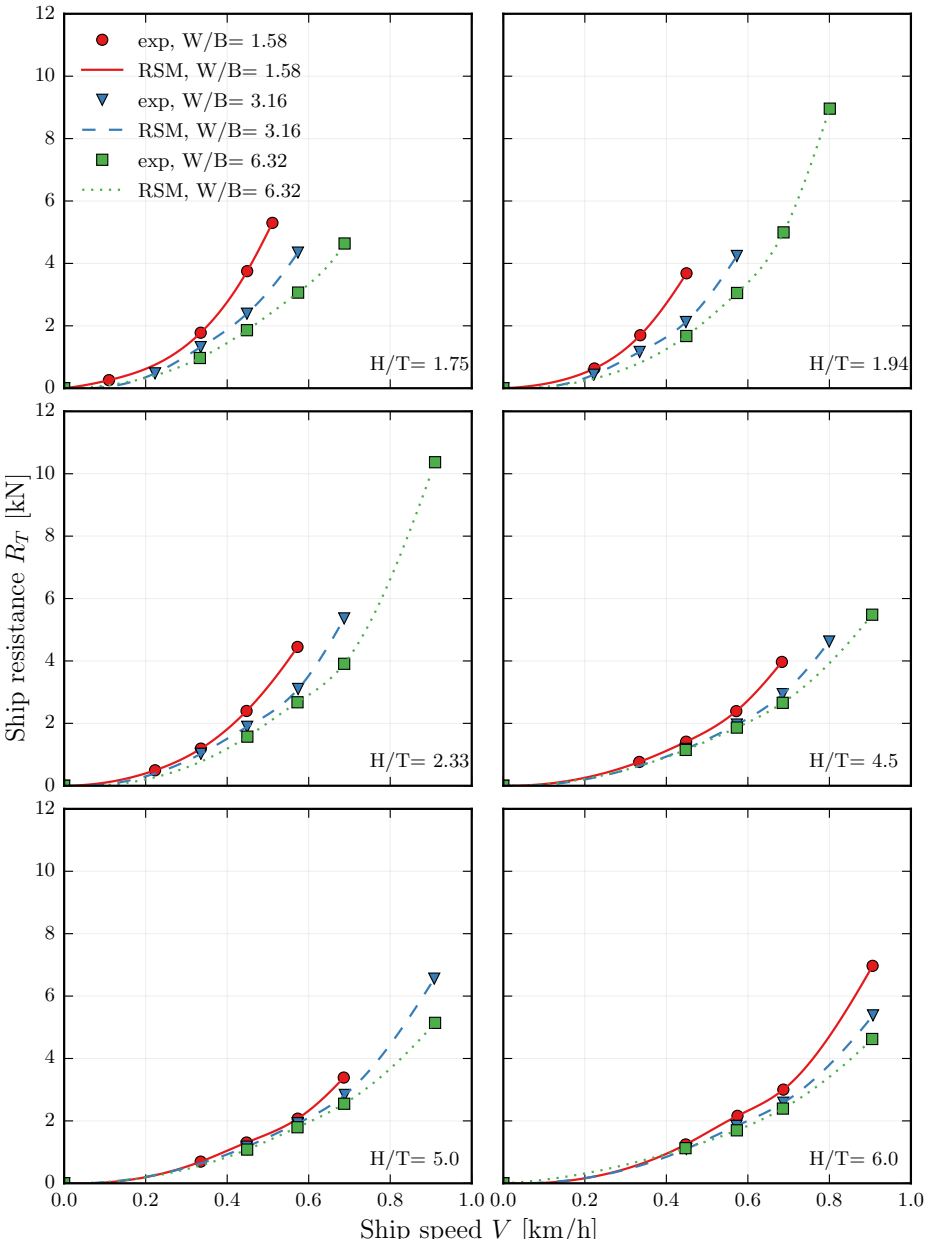

Figure 5.9.: *Comparison between experimental data and surrogate model output for RBF method.*

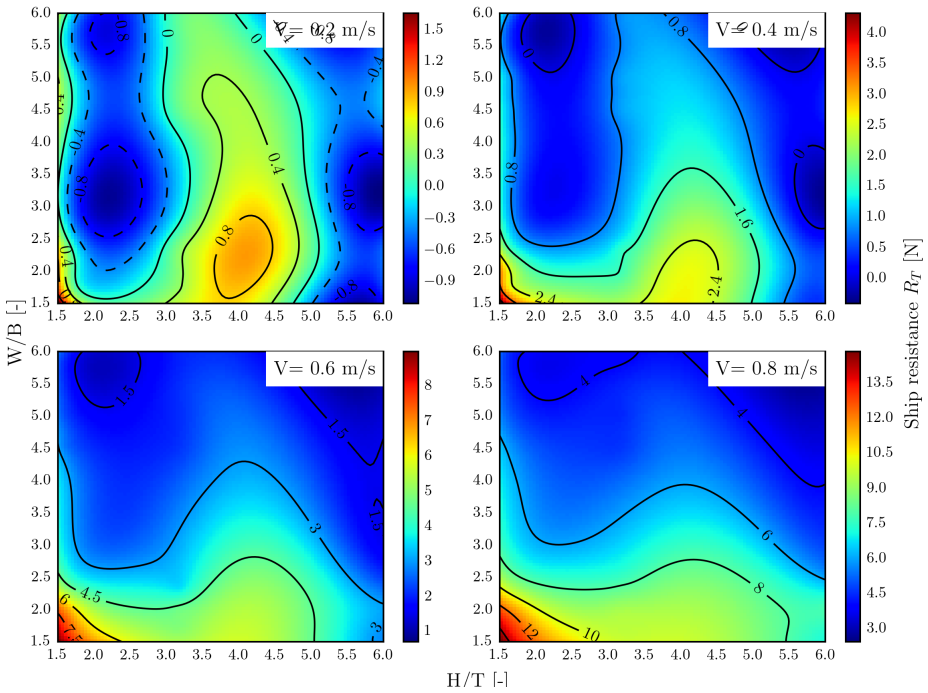

Figure 5.10.: *Iso-contours of ship resistance in function of W/B and H/T ratios at V=0.2, 0.4, 0.6 and 0.8 m/s calculated with the RBF method.*

Figure 5.9 shows that the ship resistance curves obtained with the RBF method interpolate all the experimental data points and remain smooth. However, the plots of ship resistance iso-contours presented in Figure 5.10 show that their evolution is less regular than those obtained with the Kriging and MLS method. Therefore, the MLS and Kriging method seem more adapted than RBF method for the speed optimization algorithm.

5.1.6. Summary

The mean square error calculated for the four tested methods showed that overall; MLS, Kriging, SVR and RBF methods give more accurate predictions than the PR method. Moreover, the iso-contours of ship resistance obtained with the SVR and RBF methods are fairly irregular and this behaviour does not represent a physical evolution of the ship resistance. Therefore, the MLS and Kriging methods are more adapted for this surrogate model. However, the MLS method is computationally more expensive than the Kriging method because the approximation coefficients have to be calculated for each prediction. The optimization process needing many

function evaluations, the Kriging method is chosen for this surrogate model as it is computationally quicker than the MLS method.

5.2. Comparison of optimization techniques

The four optimization techniques described in Section 4.6.2 have been tested on Reach one (see Section 4.4) for a discharge of 200 m^3/s and a ship sailing upstream. In order to evaluate the performance of each method, 50 random uniformly distributed samples for initial speed distribution have been generated in the bounded region defined by the optimization problem (see Equation (4.36)). This random sampling is achieved by using the Billiard Walk algorithm (Gryazina and Polyak, 2014). Each optimization technique has been run on this random sample and the average converging time to the solution is calculated. Table 5.1 shows the average number of iteration $Niter$, the average calculation time, the average total fuel consumption FC_T and its standard deviation σ_{FC} calculated for each method over the 50 initial speed samples.

Table 5.1.: *Comparison of the optimization algorithm performance*

Method	**Niter** [-]	**Time** [s]	$\mathbf{FC_T}$ [L]	$\sigma_{\mathbf{FC}}$ [L]
PM	14.0	17.7	203.37	0.002
GPM	6.58	3.2	203.31	0.011
FDM	19.5	9.8	209.0	2.95
SLQP	77.9	25.3	204.02	1.26

From Table 5.1 it can be seen that each method converges to the same optimum fuel consumption value ($FC_T \backsimeq 467\ kg$) except for the Feasible Direction Method. The standard deviation calculated for FDM is also important which indicates a large spreading of the optimum values found around the mean. This large spread is caused by the value of the stopping criteria ε (taken as $\varepsilon = 0.001$) which is too high for this method. Indeed, the philosophy of the Feasible Direction Method is to stay as far away as possible from the constraint boundaries. As a result the search direction tends to keep the solution away from the constraint boundary. However, by the nature of the optimization problem in itself, it can be guessed that the solution will

lie in the constraint boundary. Therefore, when V_k approaches the solution, very small step length are calculated by the line search giving very small improvement in the objective function and the stopping criteria is met before the "real" optimum is reached. Figure 5.11 illustrates the convergence of the Penalty Method, Feasible Direction Method and Gradient Projection Method for the first point of the random sample.

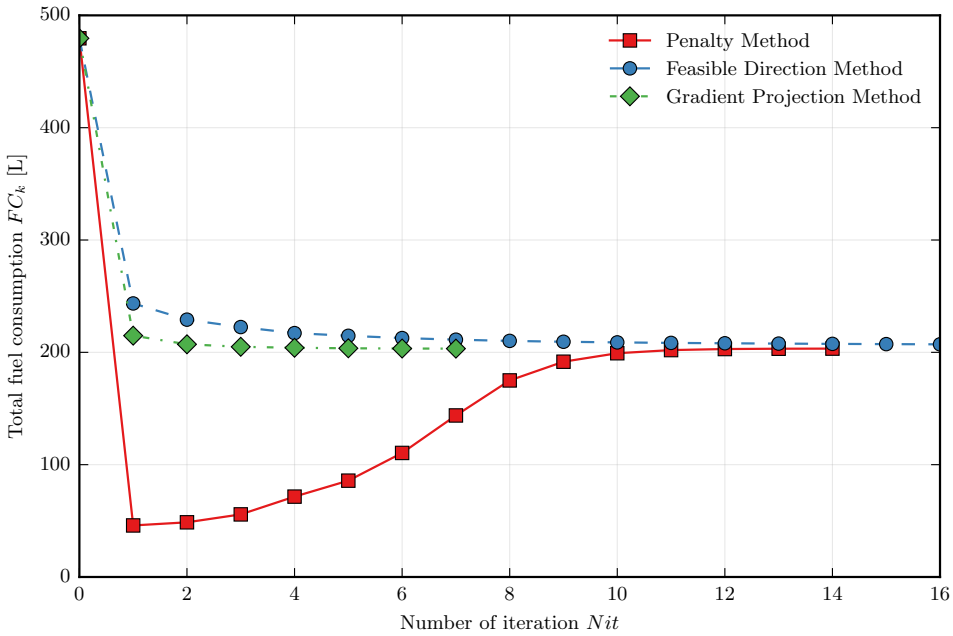

Figure 5.11.: *Illustration of the convergence of Penalty Method, Feasible Direction Method and Gradient Projection Method for a random initial speed.*

Figure 5.11 shows that the Gradient Projection Method converges much faster (7 iterations) than the Penalty (14 iterations) and Feasible Direction Method (17 iterations). It can be seen that after the first iteration of the Penalty method, the solution is located out of the feasible domain (the updated calculated speed solution is small which explains the low fuel consumption FC_T), therefore the penalty function is switch to exterior penalty function, and after a few iterations, the solution is brought back into the feasible domain and converges to the solution. The evolution of the solution calculated by the Feasible Direction Method shows a significant improvement in the objective function after first few iterations; however, after the 5^{th} iteration, this improvement is very small and continues to decrease very slowly which explains why the stopping criteria is met before the solution reaches the "real" minimum.

Table 5.1 also shows that the Penalty Method and Gradient Projection Method have lower standard deviation σ (better accuracy) and also converge faster than the SLSQP method. In average, the Gradient Projection Method is 6 times faster than the Penalty Method and shows good accuracy (low standard deviation).

Overall, the Gradient Projection Method performs better than the three other optimization techniques tested for this problem. This method is particularly adapted for this problem because it projects the search direction into the subspace tangent to the active constraints which is where the solution lies. For these reasons, this method is used to solve the speed optimization problem.

5.3. Influence of the initial speed

The four optimization techniques described in Section 4.6.2 are all local optimization methods and therefore there is no guarantee that they are converging to a global minimum. In order to ensure convergence to a global optimum, methods such as Multistart techniques (Boender et al., 1982), clustering methods (Rinnooy Kan and Timmer, 1987a) and Multi Level Single Linkage algorithm (Rinnooy Kan and Timmer, 1987b) combining a global phase and a local phase (using a local optimization method) can be used. However, those methods are outside the scope of this chapter and will not be used. To study if different local minimums are found by the Gradient Projection Method for the speed optimization problem, this algorithm was run on a random uniformly distributed samples of 500 points generated the Billiard Walk algorithm (Gryazina and Polyak, 2014). Figure 5.12 shows an example of sampling with Billiard Walk algorithm obtained for the 2D case (two legs/speed).

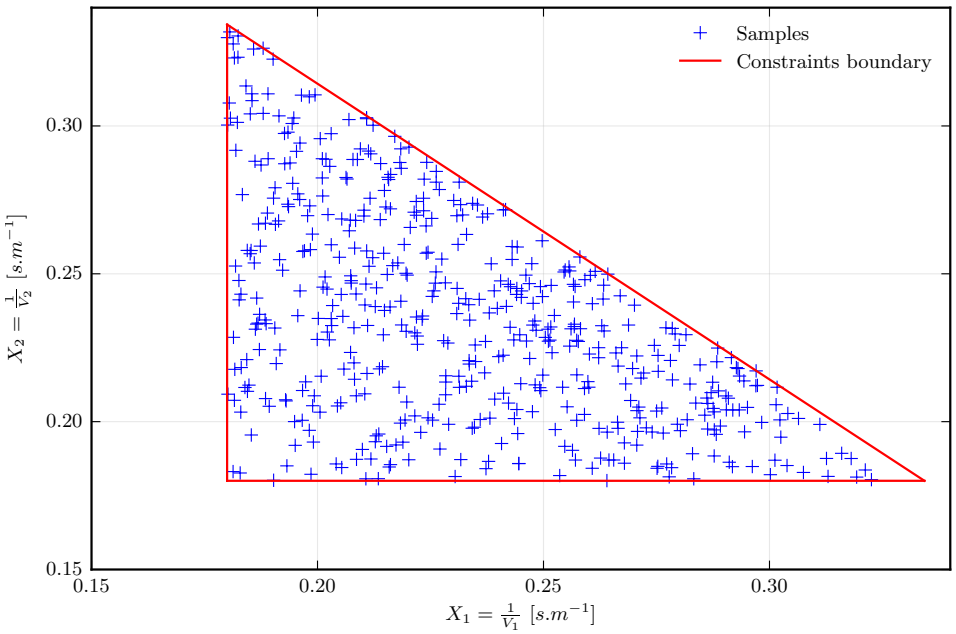

Figure 5.12.: *Illustration of the Billiard Walk algorithm sampling for the 2D case.*

This figure shows that adequate sampling of the constrained space can be obtained with this algorithm. As is illustrated in Figure 5.12, some areas of the feasible domain are more densely populated than others; however, most of the feasible domain is covered covered by samples. The total fuel consumption for the initial speed and the optimised speed is plotted in Figure 5.13 for each of the 500 samples (ship sailing upstream on Reach one for a discharge of 200 m^3/s).

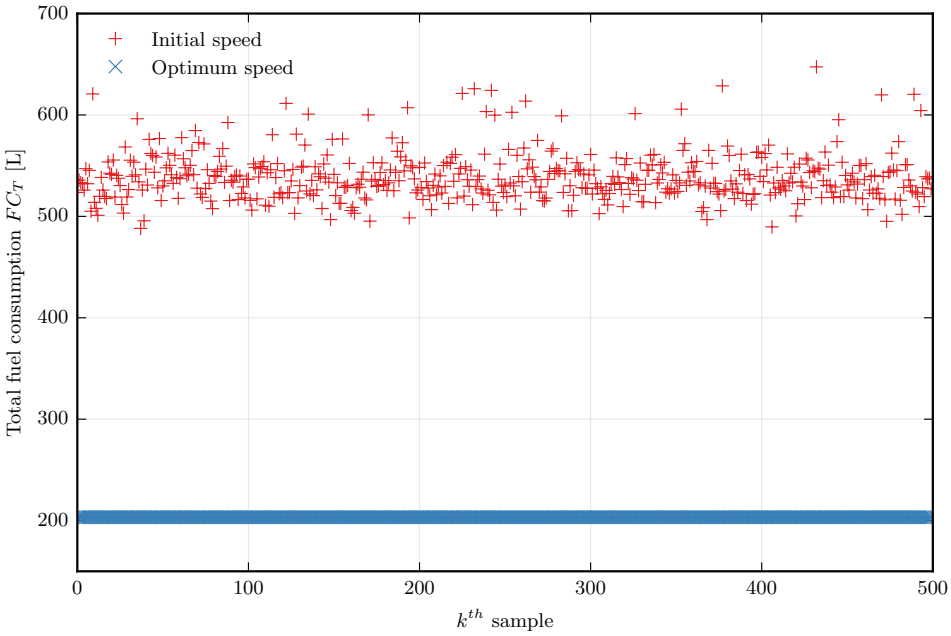

Figure 5.13.: *Total fuel consumption calculated for the initial and optimised speed of the 500 samples.*

Figure 5.13 shows a large spread of the fuel consumption calculated for the initial speed of the 500 samples varying between 500 L and 650 L. On the other hand, the value of the fuel consumption calculated for the 500 optimum speed is the same (203 L). To estimate the spread of the 500 optimum speed given by the algorithm, it is possible to calculate $\overline{\sigma_V}$, the mean of the standard deviation of each of 500 speed V_i on i^{th} leg:

$$\overline{\sigma_V} = \frac{1}{Nleg} \sum_{k=1}^{Nleg} \sigma(Vi) \tag{5.1}$$

The mean fuel consumption $\overline{FC_T}$ and its standard deviation σ_{FC} and the mean standard deviation $\overline{\sigma_V}$ are calculated and presented in Table 5.2 for the 500 initial and optimum speed.

Table 5.2.: *Statistical analysis of the results obtained by the speed optimization algorithm on the 500 samples.*

Speed	$\overline{FC_T}$ [L]	$\sigma_{\mathbf{FC}}$ [L]	$\overline{\sigma_{\mathbf{V}}}$ [m/s]
Initial	538.9	23.36	0.899
Optimum	203.3	0.01	0.009

Table 5.2 shows that the fuel consumption standard deviation σ_{FC} and the mean standard deviation of the speed $\overline{\sigma_V}$ is very small in the case of the optimum speed which indicates a very small spreading of the calculated optimum speed and consumption. Therefore, for each of the 500 samples, the optimization algorithm always converges to the same solution. Given those results, it will be assumed that the optimization algorithm applied to this problem converges to a global minimum.

5.4. Speed optimization applied to river Seine

Speed optimization tests have been run for the case of a 135 m self-propelled vessel sailing on river Seine between Chatou and Poses (153 km). Three different discharge Q (200, 500 and 900 m^3/s) and two sailing direction (upstream and downstream) are modelled. The ship used for the speed optimization process is the Bosphore, a 135m self-propelled vessel, whose characteristics correspond to those of the ship for which the resistance model has been developed. The ship draft T is 2 m corresponding to 3 layers of containers used for 80% of the travels for this ship. In the non-optimised case, the ship speed is considered constant and the value set is the average speed observed for this trajectory with AIS data ($V = 14\ km/h$ for the ship sailing downstream and $V = 12.5\ km/h$ for the ship sailing upstream). The maximum travel duration T_{max} is set as the travel time necessary for the ship to complete the itinerary at constant speed V ($T_{max} \approx 11h$ for the downstream direction and $T_{max} \approx 12h15$ for the upstream direction). In this scenario, the ship travels in the middle of the waterway which is coherent with the observed AIS (automatic identification system) trajectory. The AIS is an automatic tracking and tracing device which enables ships equipped with this system to identifyand learn the status, position and course of vessels located in the navigation area. On river Seine, since the first of January 2016, AIS equipment is mandatory for ships longer than 20 m.

Figure 5.14 and Figure 5.15 show the profile of (a) instant fuel consumption, (b) speed V and (c) water depth restriction H/T, in the case of constant speed and optimised speed for a discharge $Q = 500\ m^3/s$ and a ship sailing upstream (Figure 5.14) and downstream (Figure 5.15)

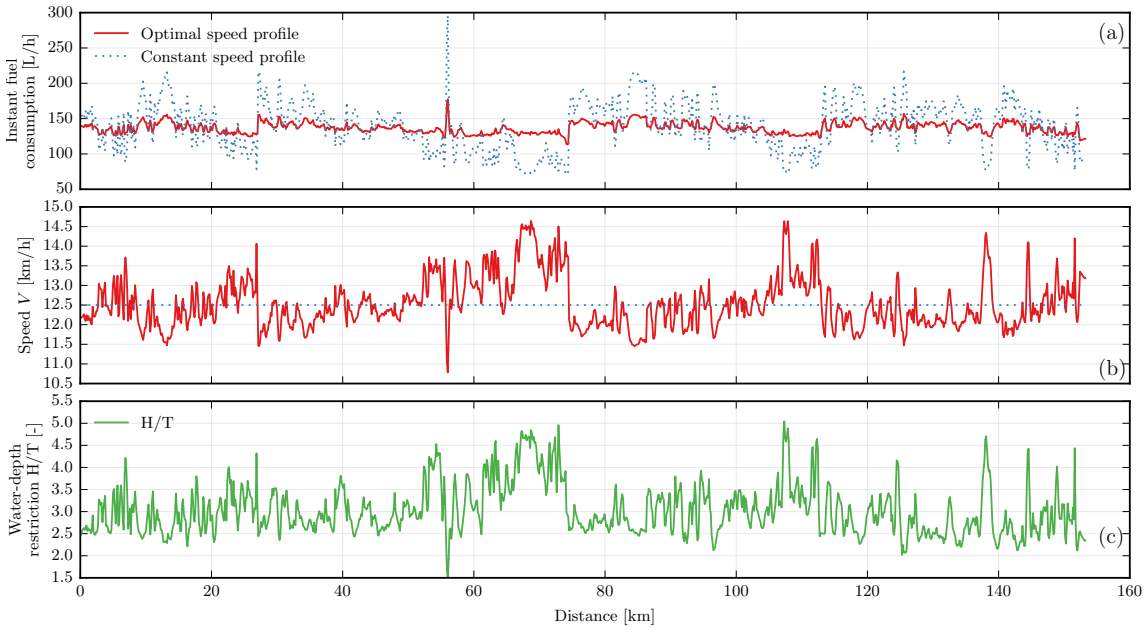

Figure 5.14.: *Profile of (a) instant fuel consumption, (b) speed V and (c) water depth restriction H/T for constant and optimal speed ($Q = 500\ m^3/s$, upstream).*

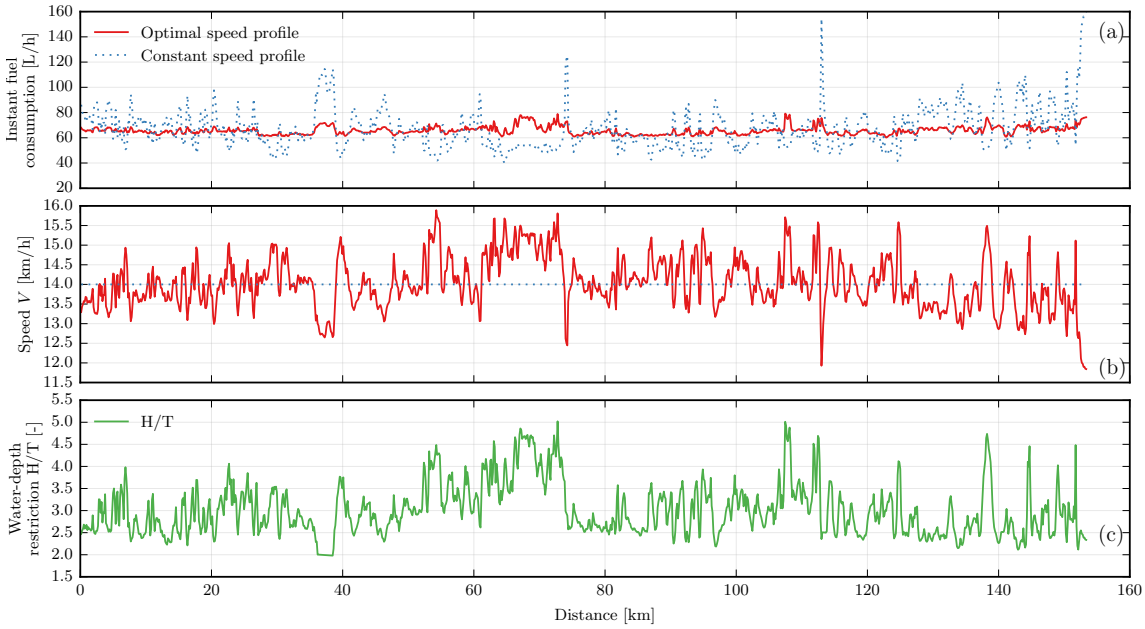

Figure 5.15.: *Profile of (a) instant fuel consumption, (b) speed V and (c) water depth restriction H/T for constant and optimal speed ($Q = 500\ m^3/s$, downstream).*

Figure 5.14 and Figure 5.15 (a) show that for the optimal speed profile, the instant consumption is relatively constant over the travel, which is not the case for

the constant speed profile. In those cases, the specific fuel consumption SFC remains nearly constant (the engine power load variation corresponds to the flat part of the SFC curve, see Figure 5.14). As a result, for the optimal speed profile, the engine power remains fairly constant during the travel, which is in agreement with findings reported by Bons et al. (2014) that minimum fuel consumption is achieved on a waterway by operating in constant power. Figure 5.14 and Figure 5.15 (b) and (c) show that the optimal speed profile and H/T profile have the same shape. The Seine being a wide river (around a hundred meters), water depth is the main parameter having an effect on the added resistance due to restriction. As a result, the ship will sail faster when restriction is less important and slow down for lower values of H/T. In the case of constant speed profile, it can be seen that the instant fuel consumption shows the opposite evolution of H/T. Indeed, the power necessary to maintain a constant speed is directly linked to the evolution of the forces opposing the movement, which depends on the level of restriction (H/T).

In the case of a ship sailing upstream, the total fuel consumption calculated for the optimal and constant speed profile are $FC_{Topt} = 1681\ L$ and $FC_{T0} = 1710\ L$, giving a fuel consumption reduction of 1.7%. In the case of a ship sailing downstream, the model predicts a fuel consumption of 720 L for the optimum profile and 736 L for the constant speed profile, giving a fuel consumption reduction of 2.2%. The big difference in fuel consumption between the ship sailing upstream and downstream is due to the current velocity which in one case (ship sailing downstream) pushes the ship forward and in the other case (ship sailing upstream) slows the ship down. The small fuel reduction values obtained in those two cases can be explained by the fact that the maximum travel time duration is calculated with constant speed profile. Therefore, any increase/decrease of speed on a leg of the itinerary must be compensated by a decrease/increase of speed on another leg of the itinerary in order to comply with the maximum travel time duration defined. If the maximum travel time duration was defined by the ETA (expected time arrival), the changes in the speed profile calculated by the optimization algorithm would be less constrained and more significant fuel savings could be achieved. From the optimization algorithm "point of view", when T_{max} is defined by the constant speed profile, the initial solution (constant speed profile) is already located on the boundary constraint (and therefore "closer" to the optimum speed) whereas if T_{max} is defined by the ETA, the initial solution would be inside the feasible domain (and therefore further away

from the optimum speed). Additionally, the constant speed profile used in this section is a coarse approximation of the speed distribution observed with AIS data.

Table 5.3 shows the average water depth $\overline{H}$, the average current velocity $\overline{Uc}$, the total fuel consumption for the constant speed profile FC_{T0} and optimal speed profile FC_{Topt}, the mean fuel consumption (in L/km) for the constant speed profile $\overline{FC_{T0}}$ and optimal speed profile $\overline{FC_{Topt}}$; and the fuel consumption reduction $FC_R = (FC_{T0} - FC_{opt})/FC_{T0} \times 100$ calculated for each of the 6 cases studied.

Table 5.3.: *Speed optimization results calculated for three discharges ($Q = 200, 500$ and $900\ m^3/s$) and two navigation direction (upstream or downstream).*

Q [m ^{3}/s]	**Dir.** [-]	$\overline{\mathbf{H}}$ [m]	$\overline{Uc}$ [m/s]	$\mathbf{FC_{T0}}$ [L]	$\mathbf{FC_{Topt}}$ [L]	$\mathbf{\Delta FC_T}$ [L]	$\overline{\mathbf{FC_{T0}}}$ [L/km]	$\overline{\mathbf{FC_{Topt}}}$ [L/km]	$\overline{\mathbf{FCR}}$ [%]
200	up	5.7	0.21	1272	1243	29	8.3	8.1	2.3
200	down	5.7	0.21	1131	1106	25	7.4	7.2	2.2
500	up	6.0	0.51	1710	1681	28	11.2	11.0	1.7
500	down	6.0	0.51	736	720	16	4.8	4.7	2.2
900	up	6.7	0.90	2339	2312	27	15.3	15.1	1.2
900	down	6.7	0.9	422	405	17	2.8	2.6	4.1

Table 5.3 shows that the fuel saving for a travel ΔFC_T vary between 17 L and 29 L with an average of 24 L. The fuel consumption reduction FC_R varies between 1.2% and 4.1% with an average of 2.3%. The fuel consumption reduction FC_R results presented in the table also show that the fuel savings obtained are more significant in the case of a ship sailing downstream. This difference could be explained by the fact that sailing against the flow limits the possible change in speed as it requires more power to increase the velocity of the ship. Figure 5.16 shows the box plots of the optimum speed distribution for the three discharges in case of a ship sailing upstream or downstream and Table 5.4 indicates the interquartile range $IQR = Q_3 - Q_1$ (where Q_1 and Q_3 are respectively first and third quartiles) and the speed range $\Delta V = V_{max} - V_{min}$ of the optimum speed for the 6 tested cases.

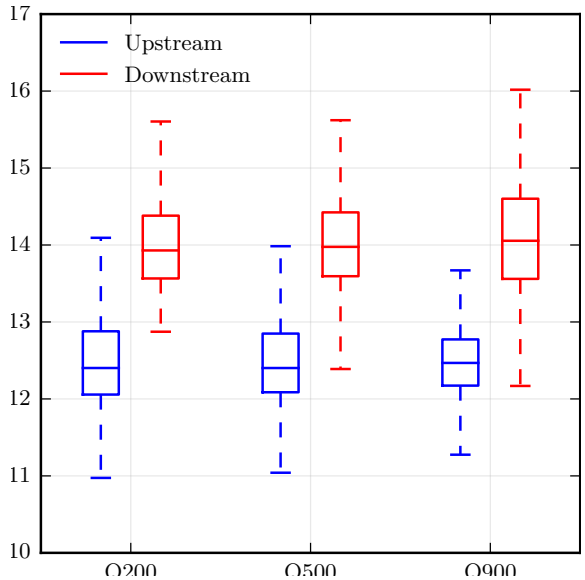

Figure 5.16.: *Illustration of the two tested set-ups*

Table 5.4.: *Calculated variation range ΔV and interquartile range IQR of the optimal speed distribution for the 6 tested cases.*

Q [m^3/s]	**ΔV** [m/s]		**IQR** [m/s]	
	Up.	Down.	Up.	Down.
200	3.7	3.1	0.82	0.81
500	3.8	4.0	0.76	0.83
900	4.5	5.6	0.60	1.04

Figure 5.16 and Table 5.4 show that for the lowest discharge ($Q = 200\ m^3/s$), there is little difference between the variability of the speed in the case of a ship sailing upstream are downstream. However, for the 300 m^3/s and 500 m^3/s discharges, the speed range and spread is clearly more significant in the case of a ship sailing downstream (the calculated values of ΔV and IQR are greater for the ship sailing downstream). These figures and plots support the argument that sailing against the flow limits the possible change in speed as it requires more power to increase the velocity of the ship.

Finally, the average fuel consumption $\overline{FC_T}$ calculated from Table 5.3 for the 6 tested cases is equal to 8.3 L/km for the constant speed profile and 8.1 L/km for the optimum speed profile. Those values are in good agreement with the average fuel consumption of 8 L/km indicated in VNF (2006) for ships of this class sailing on river Seine.

5.5. Speed optimization applied to river Seine and comparison with AIS speed

As mentioned in Section 5.4, the constant speed profile used in the previous section is a coarse approximation of the speed distribution observed with AIS data. In this section, the initial speed profile used for the optimization process is the average AIS speed observed on each leg of the travel. AIS data for the ship Bosphore and covering three full months (November and December 2017 and January 2017) has been used for this study. To be as accurate as possible, for each AIS speed collected, its timestamp has been compared to the measured discharge at Chatou's dam and only AIS data corresponding to the studied discharges have been selected for the calculation of the mean speed on each leg. Figure 5.17 shows the measured discharge at Chatou's dam for the period between November 2016 and January 2017.

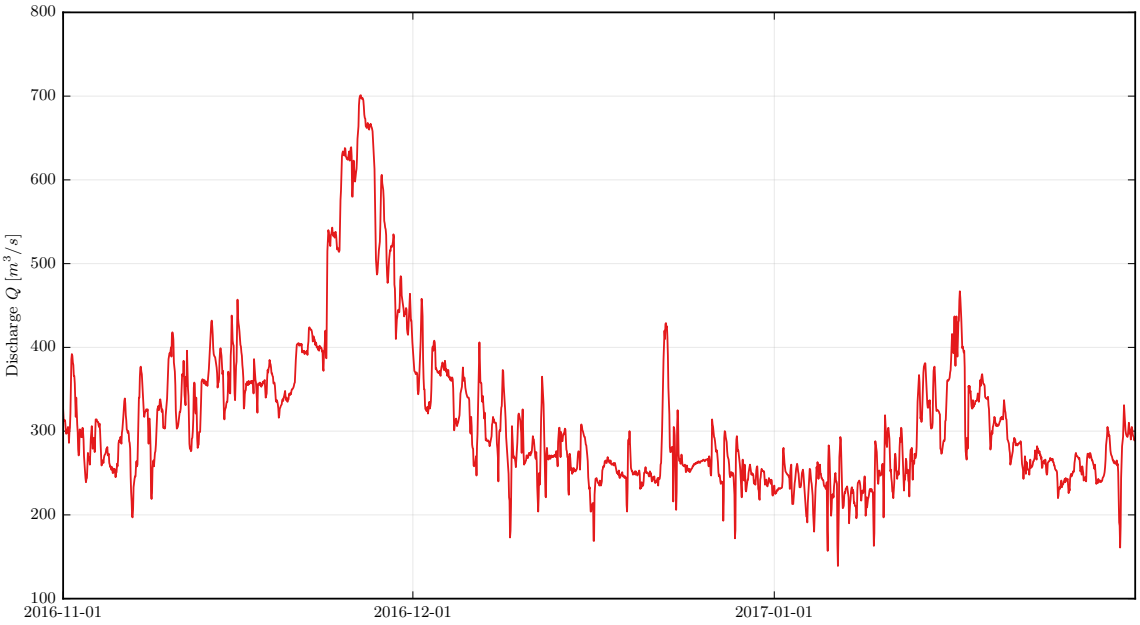

Figure 5.17.: *Measured discharge at Chatou's dam for the period between November 2016 and January 2017.*

As is shown in Figure 5.17, the measured discharge during this period does not exceed 700 m^3/s. Therefore, no AIS data was available for a discharge of 900 m^3/s and only the cases with a discharge of 200 m^3/s and 500 m^3/s are studied in this section. The maximum travel duration T_{max} is set as the travel time necessary for the ship to complete the itinerary with the mean AIS speed calculated on each leg.

Figure 5.18 and Figure 5.19 show the profile of (a) instant fuel consumption, (b) speed V and (c) water depth restriction H/T, in the case of AIS speed profile and optimised speed profile for a discharge $Q = 200\ m^3/s$ and a ship sailing upstream (Figure 5.17) and downstream (Figure 5.18).

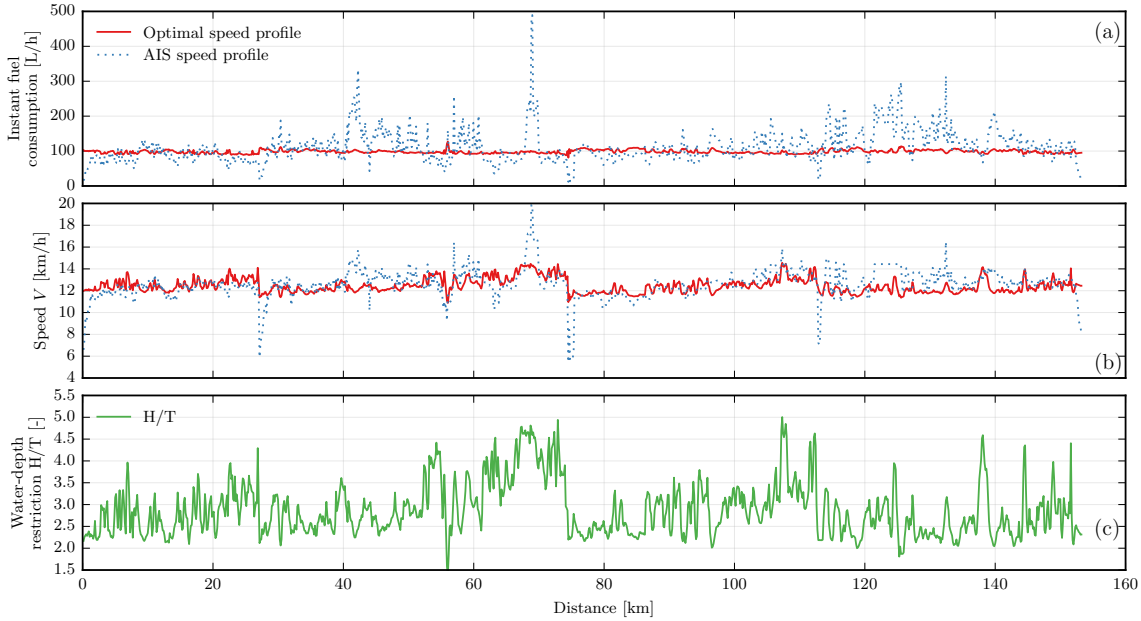

Figure 5.18.: *Profile of (a) instant fuel consumption, (b) speed V and (c) water depth restriction H/T for AIS and optimal speed ($Q = 200\ m^3/s$, upstream).*

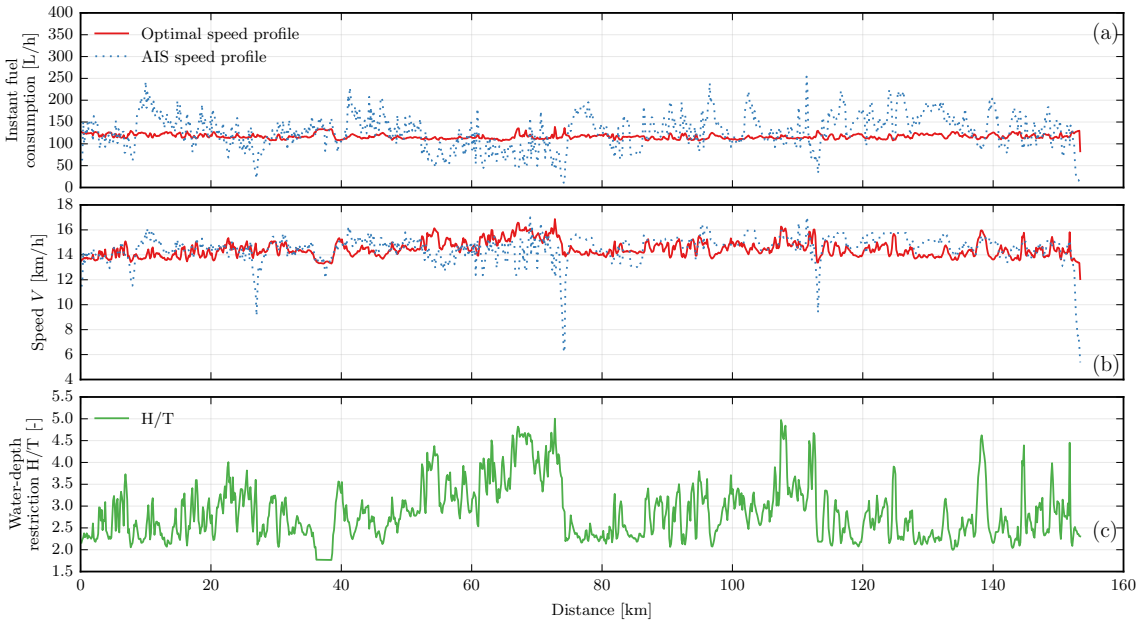

Figure 5.19.: *Profile of (a) instant fuel consumption, (b) speed V and (c) water depth restriction H/T for AIS and optimal speed ($Q = 200\ m^3/s$, downstream).*

Figure 5.18 and Figure 5.19 show that the speed profile observed with AIS data varies significantly over the travel length. The four low speed peaks observed at around 25, 75, 110 and 155 km correspond to a slow down of the ship when approaching a lock on the itinerary. Those two figures also show that the speed variation amplitude is less significant for the optimum speed profile than for the AIS speed profile. The two remarks made in the last section about the optimum speed profile showing the same pattern as the water-depth restriction profile and the instant consumption being relatively constant over the travel for the optimum profile also apply for those two cases.

Table 5.3 shows the average water depth $\overline{H}$, the average current velocity $\overline{Uc}$, the total fuel consumption for the AIS speed profile FC_{T0} and optimal speed profile FC_{Topt}, the mean fuel consumption (in L/km) for the AIS speed profile $\overline{FC_{T0}}$ and optimal speed profile $\overline{FC_{Topt}}$; and the fuel consumption reduction $FC_R = (FC_{T0} - FC_{opt})/FC_{T0} \times 100$ calculated for each of the 4 cases studied.

Table 5.5.: *Speed optimization results calculated for two discharges ($Q = 200$ and $500\ m^3/s$) and two navigation direction (upstream or downstream).*

Q [m ^{3}/s]	**Dir.** [-]	$\overline{\mathbf{H}}$ [m]	$\overline{Uc}$ [m/s]	$\mathbf{FC_{T0}}$ [L]	$\mathbf{FC_{Topt}}$ [L]	$\mathbf{\Delta FC_T}$ [L]	$\overline{\mathbf{FC_{T0}}}$ [L/km]	$\overline{\mathbf{FC_{Topt}}}$ [L/km]	$\overline{\mathbf{FCR}}$ [%]
200	up	5.7	0.21	1327	1215	112	8.7	7.9	9.3
200	down	5.7	0.21	1335	1244	92	8.7	8.1	7.4
500	up	6.0	0.51	1974	1851	123	12.9	12.0	6.6
500	down	6.0	0.51	674	623	51	4.4	4.1	8.2

Table 5.5 shows that the fuel saving for a travel ΔFC_T vary between 51 L and 123 L with an average of 95 L. The fuel consumption reduction FC_R varies between 6.6% and 9.3% with an average of 7.9%. The average fuel saving calculated in this section is significantly better that the average fuel saving calculated when comparing with a constant speed profile. This is mainly due to the fact that the difference in speed between the constant speed profile and optimum speed profile calculated in the last section is less important than that the difference between the AIS speed profile and the optimum speed profile calculated in this section. In other terms, the constant speed profile is closer to the optimum speed profile than the AIS speed profile. For instance, in the case of a ship sailing upstream with a 200 m^3/s, the mean speed distance $\overline{\Delta V} = \frac{1}{Nleg}\sum_{k=1}^{Nleg}|V_k^0 - V_k^{opt}|$ between the constant and optimal speed is equal to 0.51 m/s whereas the distance between the AIS and optimum speed profile is equal to 0.86 m/s. Finally, the average fuel consumption $\overline{FC_T}$ calculated from Table 5.5 for the 4 tested cases is equal to 8.7 L/km for the constant speed profile and 8.05 L/km for the optimum speed profile. Those values are close to those calculated in the previous section and in agreement with the average fuel consumption of 8 L/km indicated in VNF (2006).

5.6. Influence of trajectory and travel duration

With the aim of studying the influence of the lateral position of the ship in the channel, the previous simulation (ship sailing upstream on Reach one for a discharge of 200 m^3/s) was compared with the results obtained when the ship is sailing in the deepest part of the river. In the latter scenario, the turning circle of the vessel is not

taken into account, and choosing the deepest part of the river occasionally create discontinuities in the trajectory. Figure 5.20 shows (a) the instant consumption, (b) the speed profile and (c) water depth restriction ratio H/T profile against the distance for the two scenarios.

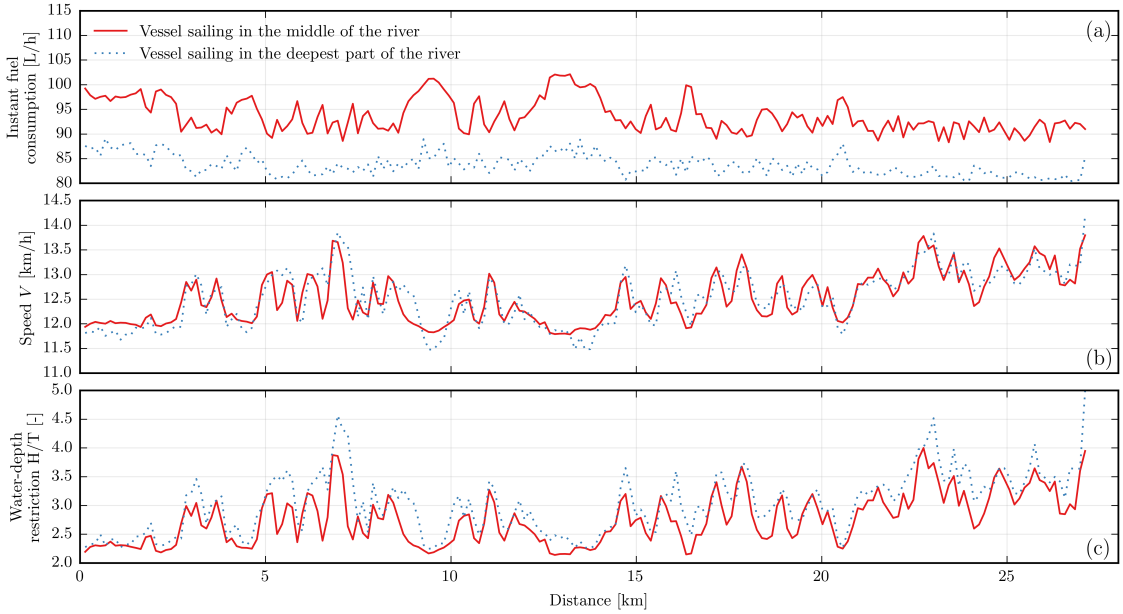

Figure 5.20.: *Profile of (a) instant fuel consumption, (b) speed V and (c) water depth restriction H/T for the vessel sailing in the middle and in the deepest part of the river (ship sailing upstream on Reach one for a discharge of 200 m^3/s).*

Figure 5.20 shows that the water depth profile in the case of a ship sailing in the middle and in the deepest part of the river have the same shape; however, the water depth restriction is less important for the ship sailing in the deepest part of the waterway. Both speed profiles also show the same pattern but the ship navigating in the deepest part of the river tends to go faster when the restriction is low and slower when it is important. As a result, the instant consumption is clearly lower in the case of the ship sailing at maximum depth. The main reason for that is that the added force due to water depth restriction is less important when the ship sails in the deepest part of the river. In the case of the ship sailing at maximum water depth, the total consumption obtained is $FC_{Topt} = 181.7L$ for the optimal speed profile. The comparison with the consumption obtained for the ship sailing in the middle of the river ($FC_{Topt} = 203.3L$) gives a 10.6% reduction of the total fuel consumption. Although this reduction could be less important when taking turning circle into account, this result indicates choosing the optimal track can also lead

to additional fuel savings. Theoretically, this track could be determined with up to date bathymetry data of Seine river bottom, but other factors also have to be taken into account such as the continuity of the trajectory and locally specific navigation rules.

The influence of travel duration on the optimal fuel consumption has been studied by running several simulations in which the maximum travel duration T_{max} is increased, from 2h to 3h30 (ship sailing upstream on Reach one for a discharge of 200 m^3/s). Figure 5.21 presents the evolution of the optimal fuel consumption FC_T and the fuel consumption reduction $FC_{RED} = \frac{FC_T(2h) - FC_T(T_{max})}{FC_T(2h)} \times 100$, against the maximum travel duration T_{max}.

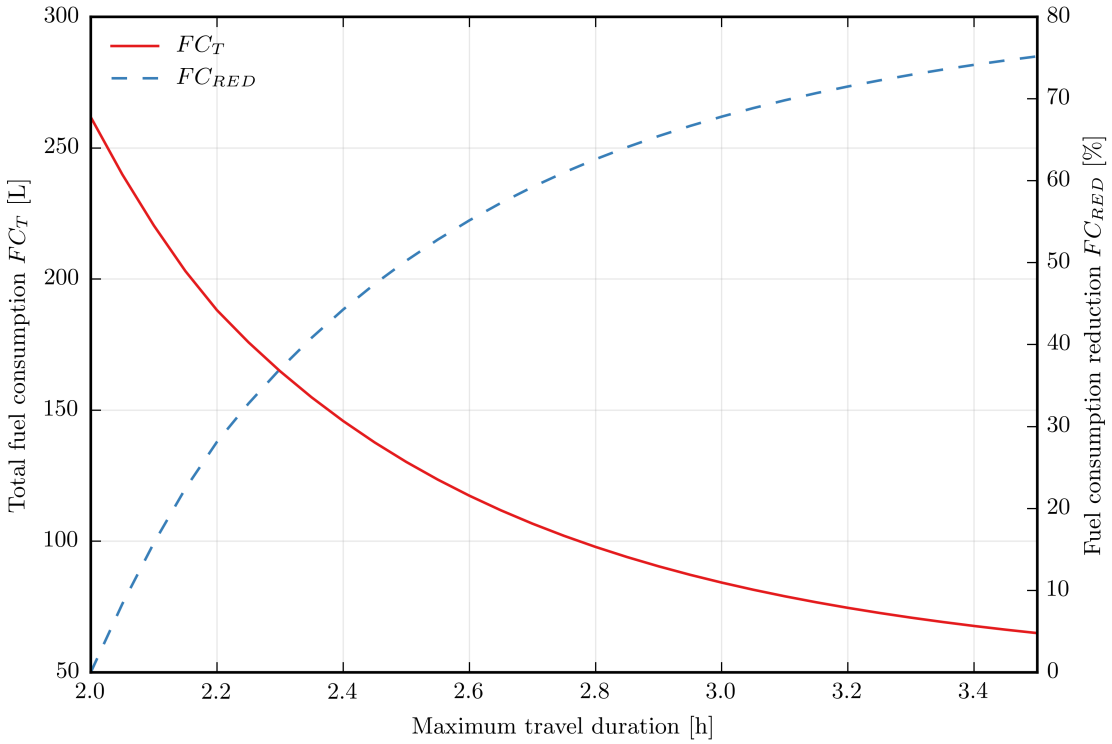

Figure 5.21.: *Evolution of total fuel consumption FC_T and fuel consumption reduction FC_{RED} against the maximum travel duration T_{max} (ship sailing upstream on Reach one for a discharge of 200 m^3/s).*

Figure 5.21 shows that fuel consumption decreases sharply for a travel duration between 2h and 2.5h and at a steadier rate afterwards. The main reason for this evolution is that the thrust power necessary to maintain a ship at a constant speed V is roughly proportional to V^3. Therefore, increasing the maximum travel duration

allows to reduce the average speed; and the fuel consumption, linked to the thrust power, decreases in an exponential manner. For instance, a 15 minutes travel time increase, from 2h to 2h15, leads to a 32% fuel consumption reduction. This fact highlights another important aspect of fuel consumption optimization: including real time information in the optimization process can lead to additional fuel savings. For instance, knowing in advance that an approaching lock is unavailable due to maintenance or ship queue can be used to reduce the sailing speed in order to avoid waiting at the lock and make fuel savings.

5.7. Conclusions

The techniques available for the ship resistance and speed optimization modules described in chapter 4 were compared to determine which ones are the most suited for EcoNav. The analysis of surrogate model results showed the MLS and Kriging methods are the most accurate. The Kriging method was selected due to its better computational efficiency. The four optimization techniques described in chapter 4 were applied for the first reach of the Chatou-Poses itinerary. The results showed that each method reached the same optimum solution and the Feasible Direction Method was chosen for its fast convergence and good accuracy. Furthermore, the FDM was applied for a random uniformly distributed sample to study if the initial speed had an effect on the solution found and the method converged to the same solution for all the samples.

In the second part of this chapter, EcoNav has been applied to a real case: the itinerary of the self-propelled ship Oural on river Seine, between the locks of Chatou and Poses. First, the fuel consumption of a ship sailing at a constant average AIS speed is compared with the fuel consumption obtained with speed optimization; the maximum travel duration being defined by the travel duration of the ship sailing at constant speed. The average fuel consumption reduction calculated for all the tested configuration was 2.3 %. The low fuel savings reported in this case are explained by the fact that the maximum travel duration on the itinerary is calculated with the constant speed profile. This way of defining the maximum travel duration tends to limit possible changes in speed profile calculated by the optimization algorithm. Moreover, the constant speed profile used for the fuel consumption comparison is a coarse approximation of the speed distribution observed with AIS

data. Therefore, the calculated optimum consumption was compared to a more accurate AIS speed profile defined by the mean AIS observed speed on each leg. The average reported fuel savings for all the tested configuration was 7.9 %. This difference in fuel consumption reduction is mainly due to the fact that the AIS speed profile is farther away from the optimum solution than the constant speed profile. In both cases, the average calculated fuel consumption on this itinerary is in agreement with the results reported in VNF (2006) for this type of ship. The comparison of optimal fuel consumption obtained in the case of a ship sailing in the middle or in the deepest part of the waterway demonstrated that significant fuel savings can be expected by optimizing the vessels trajectory. Finally, it was shown that additional fuel consumption reduction can be realized by extending the duration of the travel. The latter solution could be used in case of lock unavailability or heavy traffic and would necessitate including real time information in the optimizing process.

Conclusion and perspectives

Conclusion

The main objective of this PhD was to develop an Economy Planner with the aim of optimizing a vessel speed and reduce fuel consumption for a given itinerary. To achieve this goal, the work undertaken in this PhD has been divided in two main tasks: the development of a ship resistance model allowing to evaluate the fuel consumption of a ship sailing in a channel and its integration into a speed optimization model composed of several modules developed during the second part of this thesis.

The 3D numerical model described in chapter 2 is based on the resolution of the RANS equations with the CFD software ANSYS Fluent 13. The fluid solver is coupled with a Newtonian method used to find the equilibrium position and avoid modelling the transient oscillations of the ship. This model has been validated with towing tank test conducted by Architecture Navale et Systèmes de Transports (ANAST) researchers at the University of Liege, Belgium (Vandescuren et al., 2013). The comparison between experimental data and numerical results has shown that the predicted resistance and sinkage are in close agreement with measurement for velocities below 0.7 m/s but discrepancies appeared for the highest tested velocity (0.9 m/s). For the ship speed of 0.9 m/s the numerical model overestimates the sinkage and underestimates the resistance. It is possible that for this speed the model is not able to reproduce correctly the pressure field around the ship hull therefore underestimating vertical and horizontal pressure forces. It was also shown that taking ship sinkage into account allowed to significantly reduce the prediction error. The model was used to study the influence of channel width and water depth restriction.

The results showed that in case of water depth restriction, ship sinkage is more significant and results in higher ship resistance increase. The comparison between experimental data and various empirical models showed that those models can be used to calculate an approximate range of variation for ship resistance in shallow water with low lateral restriction. However, when width restriction is severe, those models might perform poorly and underestimate ship resistance. The numerical flow results were also compared to shallow water ship waves experimental results from Pprime institute in chapter 4. The objective of this comparison was to evaluate the ability of the numerical model to reproduce the flow and waves generated by a ship navigating in shallow water for speeds greater than subcritical speed and investigate the discrepancies for ship resistance prediction at high speed observed in chapter 3. The results showed that overall the flow around the ship is correctly reproduced. However, the comparison also highlighted some errors in the simulated flow: at the stern of the ship, the reflection of the waves on the banks and the wave amplitude are too small, and the bow wave seems to be propagating up to the inlet. A sensitivity study on the influence of several numerical parameters showed that the waves generated behind the ship are strongly influenced by the distance between the stern and the outlet and that the bow wave propagation seems to be created by a change in flow regime due to the fact that the speed is given to the fluid and not to the ship. It should be noted that for accurate ship resistance evaluation, a good prediction of the flow around the ship is more important than a good prediction of the ship waves as in our model, the ship resistance is calculated by integrated fluid forces acting on the hull. Overall, the numerical method presented in this PhD can be applied for any restricted waterway configuration and any inland vessel to calculate accurate results of ship resistance. This model can also provide a better understanding of hydrodynamics phenomena in confined waters. Finally, this study also presents some guidance for accurate predictions of ship resistance in restricted waterways.

In the second part of this thesis, EcoNav and its modules have been described in chapter 5 and applied to a real case study in chapter 6. This Economy Planner is based on an optimization algorithm minimizing the fuel consumption by finding the optimal speed profile for a given itinerary (operating conditions) under specified constraints (maximum travel duration). The fuel consumption is evaluated with a specific fuel consumption empirical model developed by Hidouche et al.

(2015) and a ship resistance surrogate model based on ship resistance numerical results obtained from the ship resistance numerical model presented in chapter 2. The operating conditions used by EcoNav (channel width, water depth and current velocity) are calculated by using a 2D hydraulic model (Telemac2D). Several methods for the surrogate model and the optimization process were tested in chapter 6 and allowed to select the most appropriate (in terms of accuracy and speed) for EcoNav. EcoNav has been applied to study the itinerary of the self-propelled ship Oural on river Seine, between the locks of Chatou and Poses. The comparison between the optimum fuel consumption and a the fuel consumption obtained for a constant speed profile showed limited benefits with an average fuel consumption reduction of 2.3 %. However, the comparison to a more realistic speed profile, defined by the mean AIS observed speed on each leg of the itinerary, showed significant improvement in fuel consumption reduction, with an average calculated savings of 7.9 %. In both cases, the average calculated fuel consumptions on this itinerary are in agreement with the results reported in VNF (2006). The comparison of optimal fuel consumption obtained in the case of a ship sailing in the middle or in the deepest part of the waterway demonstrated that significant fuel savings can be expected by optimizing the vessels trajectory. Finally, it was shown that additional fuel consumption reduction can be realized by extending the duration of the travel. The latter solution could be used in case of lock unavailability or heavy traffic and would necessitate including real time information in the optimizing process. Altogether, this thesis presented three ways of reducing fuel consumption: optimizing the speed and trajectory of a vessel and including real time information in the optimization process. The speed optimization model presented in this PhD is still at an early stage design and needs further improvement and validation. Several limitations to this model can be listed:

- the change in the ship speed is instantaneous and the acceleration/deceleration is not taken into account nor its impact on fuel consumption;
- the trajectory is linearised, as a result its curvature and impact on fuel consumption is neglected;
- wind effect on ship resistance and fuel consumption is not taken into account;
- the hydrodynamic model cannot currently simulate a sea tide and therefore EcoNav cannot be used in intertidal area;
- the ship consumption model needs further validation.

Perspectives

The ship resistance numerical model developed in this PhD allows to calculate accurate results of ship resistance. However, as mentioned in the conclusion, for speeds approaching the subcritical velocity (Schijf limiting speed), the predicted results are less accurate. It is possible that the discrepancies observed between the numerical and experimental results stem from the fact that in the numerical model the ship is not moving and its speed is applied to the fluid; while in the experiment the ship is towed. As a result, for high speed, a change in flow state (subcritical to supercritical) could explain the numerical errors. Therefore, the numerical model could be improved by applying the speed to the ship. In Ansys Fluent, this could be achieved by using the Moving Reference Frame Technique in which different cell zones move at different speeds. Further collaborations with towing tanks (Pprime institute for instance) could also help improve this model by comparing experimental and numerical results for subcritical speeds near the subcritical velocity for instance.

The application of EcoNav to study the itinerary of the self-propelled ship Oural on river Seine has shown that fuel savings on the order of 8 % could be expected. This model could be improved by taking into account the acceleration/deceleration of the ship in the fuel consumption model and the optimization process, and including the effects of the trajectory curvature in the model (by taking into account the rudder effects for instance). Existing empirical models for air resistance calculation could also be used to take the effect of wind into account in the fuel consumption model. The accuracy of the propulsion modelling could also be improved by using existing empirical models to calculate the various propulsion efficiencies. A project is currently ongoing to instrumentalize the 135 m self propelled ship Bosphore, in collaboration with Compagnie Fluviale de Transport, in order to realize a broad range of in situ measurement (fuel consumption, engines rpm, ship's speed and position,...) over the span of one year. Data recorded from this project will help improve and validate the ship fuel consumption model. Cerema is also involved in Seine RIS (River Information Service) and will work on the development of three modules: ETA prediction for inland ships, optimization of waiting times in river locks and estuary hydrodynamic model for the prediction of bridge clearance. The feedbacks from this project can contribute to include a sea tide effect and real time traffic information into EcoNav. When EcoNav has reached a higher maturity level,

a prototype could be built and tested on a ship in situ.

Bibliography

Agence de l'Environnement et de la Maitrise de l'Energie (2006). Transports combinés rail-route, fleuve-route et mer-route : tableau de bord national. Technical report.

Aitken, A. C. (1936). Iv.on least squares and linear combination of observations. *Proceedings of the Royal Society of Edinburgh*, 55:42–48.

Amouzgar, K. and Strömberg, N. (2015). Radial basis functions with a priori bias in comparisonwith a posteriori bias under multiple modeling criteria. *Structural and multidisciplinary optimization (Print)*.

Ansys (2010a). *Ansys Fluent 13.0 theory guide*.

Ansys (2010b). *Ansys fluent 13.0 users guide*.

Artjuskov, L. (1968). Wall effect correction for shallow water model tests. *NE Coast Institution of Engineers and Shipbuilders*.

Assemblée Nationale (2011). Rapport de l'assemblé nationale no. 3942 du 15 novembre 2011 relatif à voies navigables de france. Technical report.

Basak, D., Pal, S., and Patranabis, D. C. (2007). Support vector regression. *Neural Information Processing-Letters and Reviews*, 11(10):203–224.

Boender, C. G. E., Rinnooy Kan, A., Timmer, G., and Stougie, L. (1982). A stochastic method for global optimization. *Mathematical programming*, 22(1):125–140.

Bons, A., MOLENMAKER, K., and van WIRDUM, M. (2014). Economyplanner; optimal use of inland waterways. In *European Inland Waterway Navigation Conference, Budapest, 10th–12th September*.

Boussinesq, J. (1877). *Essai sur la théorie des eaux courantes*. Imprimerie nationale.

Box, G. E., Draper, N. R., et al. (1987). *Empirical model-building and response surfaces*, volume 424. Wiley New York.

Bradshaw, P. (1987). Turbulent secondary flows. *Annual review of fluid mechanics*, 19(1):53–74.

Briggs, M. J., Vantorre, M., Uliczka, K., and Debaillon, P. (2009). Prediction of squat for underkeel clearance. *Handbook of Coastal and Ocean Engineering*.

Caplier, C., Linde, F., Bernard, A., Calluaud, A., David, L., Ouahsine, A., Rousseaux, G., and Sergent, P. (2015). Comparaison entre expérience et calcul des ondes générées par un bateau en eaux peu profondes. Technical report.

Celik, I. B., Ghia, U., Roache, P. J., et al. (2008). Procedure for estimation and reporting of uncertainty due to discretization in cfd applications. *Journal of fluids Engineering-Transactions of the ASME*, 130(7).

Chatellier, L., Jarny, S., Gibouin, F., and David, L. (2010). Stereoscopic measurement of free surface flows. In *EPJ Web of Conferences*, volume 6, page 12002. EDP Sciences.

Conference, I. T. T. (2008). Testing and data analysis resistance test. *ITTC Recommended Procedures and Guidelines, Procedure 7.5-02-01*.

Constantine, T. (1960). On the movement of ships in restricted waterways. *Journal of Fluid Mechanics*, 9(02):247–256.

Cosner, R., Oberkampf, B., Rumsey, C., Rahaim, C., and Shih, T. (2006). AIAA Committee On Standards For Computational Fluid Dynamics: Status and Plans. In *44th AIAA Aerospace Sciences Meeting and Exhibit*, Aerospace Sciences Meetings. American Institute of Aeronautics and Astronautics.

Dand, I. and Ferguson, A. (1973). The squat of full ships in shallow water. Technical report, DTIC Document.

Das, S., Das, S. K., and Kariya, J. (2012). Simulation of return flow in restricted navigation channel for barge-tow movements. *Open Ocean Engineering Journal*, 5:34–46.

Debaillon, P. (2010). Numerical investigation to predict ship squat. *Journal of Ship Research*, 54(2):133–140.

Drucker, H., Burges, C. J., Kaufman, L., Smola, A., and Vapnik, V. (1997). Support vector regression machines. *Advances in neural information processing systems*, 9:155–161.

Eurostat (2015). Inland waterways freight transport - quarterly and annual data.

Federal German Water and Shipping Administration (2007). Economical and ecological comparison of transport modes: road, railways, inland waterways. Technical report.

Foeth, E. (2008). Decreasing frictional resistance by air lubrication. In *20th International HISWA Symposium on Yacht Design and Yacht Construction, Amsterdam, The Netherlands*.

Forrester, A. I. and Keane, A. J. (2009). Recent advances in surrogate-based optimization. *Progress in Aerospace Sciences*, 45(1):50–79.

Geerts, S., Verwerft, B., Vantorre, M., and Van Rompuy, F. (2010). Improving the efficiency of small inland vessels. In *Proc., 7th European Inland Waterway Navigation Conference*. Budapest University of Technology and Economics, Budapest, Hungary.

Georgakaki, A. and Sorenson, S. (2004). Report on collected data and resulting methodology for inland shipping. *Lyngby, Denmark, Technical University of Denmark*.

Gomit, G., Rousseaux, G., Chatellier, L., Calluaud, D., and David, L. (2014). Spectral analysis of ship waves in deep water from accurate measurements of the free surface elevation by optical methods. *Physics of Fluids*, 26(12):122101.

Gourlay, T. (2008). Slender-body methods for predicting ship squat. *Ocean Engineering*, 35(2):191–200.

Gryazina, E. and Polyak, B. (2014). Random sampling: Billiard walk algorithm. *European Journal of Operational Research*, 238(2):497–504.

Haftka, R. and Starnes, JR, J. (1975). Applications of a quadratic extended interior penalty function for structural optimization. In *16th Structural Dynamics, and Materials Conference*, page 764.

Haftka, R. T. and Gürdal, Z. (2012). *Elements of structural optimization*, volume 11. Springer Science & Business Media.

Hardy, R. L. (1971). Multiquadric equations of topography and other irregular surfaces. *Journal of geophysical research*, 76(8):1905–1915.

Härting, A., Laupichler, A., and Reinking, J. (2009). Considerations on the squat of unevenly trimmed ships. *Ocean Engineering*, 36(2):193–201.

Hervouet, J.-M. (2007). *Hydrodynamics of free surface flows: modelling with the*

finite element method. John Wiley & Sons.

Hidouche, S., Guitteyn, M.-H., Linde, F., and Sergent, P. (2015). Ships propulsion : estimation of specific fuel consumption based on power load factor ratio. In *Proc., Hydrodynamics and simulation applied to inland waterways and port approaches*. SHF, Société hydrotechnique de France.

Hirt, C. W. and Nichols, B. D. (1981). Volume of fluid (vof) method for the dynamics of free boundaries. *Journal of computational physics*, 39(1):201–225.

Holtrop, J. (1984). A statistical re-analysis of resistance and propulsion data. *International Shipbuilding Progress*, 31(363):272–276.

Holtrop, J. (1988). A statistical resistance prediction method with a speed dependent form factor. In *SMSSH88*.

Holtrop, J. and Mennen, G. (1982). An approximate power prediction method. *International Shipbuilding Progress*, 29.

Huybrechts, N., Linde, F., and Sergent, P. (2015). Construction de modèles hydrodynamiques 2d de la seine entre chatou et poses. Technical report, Cerema Eau, mer et fleuves.

ITTC (1978). Report of performance committee. In *Proc., 15th International Towing Tank Conference*, pages 128–183. International Towing Tank Conference.

ITTC (1987). Report of the resistance and flow committee. In *Proc., 18th International Towing Tank Conference*, pages 47–95. International Towing Tank Conference.

ITTC (2011). Practical guidelines for ship cfd applications. In *Proc., 26th International Towing Tank Conference*. International Towing Tank Conference.

Jansen, P. and Schijf, J. (1953). The relation between the form of cross section the cross section, the method of revetment and the distribution of the water velocities in a waterway. In *Proc., 18th International Navigation Congress*, pages 175–197. World Association for Waterborne Transport Infrastructure (PIANC), Brussels, Belgium.

Jastrzebski, T., Sekulski, Z., Taczala, M., Graczyk, T., Banasiak, W., and Zurawski, T. (2003). A concept of the inland waterway barge base on the i-corer steel panel. In *European Inland Waterway Navigation Conf., Gyor*.

Ji, S. C., Ouahsine, A., Smaoui, H., and Sergent, P. (2012). 3-d numerical simulation of convoy-generated waves in a restricted waterway. *Journal of Hydrody-*

namics, Ser. B, 24(3):420–429.

Jones, E., Oliphant, T., Peterson, P., et al. (2001). SciPy: Open source scientific tools for Python.

Jovanović, M. (2004). Otpor broda u plovnom kanalu [ship resistance in navigation canals]. *Vodoprivreda*, 36(209-210):283–288 (in Serbian).

Karpov, A. (1946). Calculation of ship resistance in restricted waters. *TRUDY GII. T. IV*, 2:(in Russian).

Keogh, E., Chakrabarti, K., Pazzani, M., and Mehrotra, S. (2001). Dimensionality reduction for fast similarity search in large time series databases. *Knowledge and information Systems*, 3(3):263–286.

Koziel, S. and Leifsson, L. (2013). *Surrogate-Based Modeling and Optimization: Applications in Engineering*. Springer Science & Business Media.

Kreitner, J. (1934). Uber den schiffswiderstand auf beschranktem wasser. *Werft Reederei Hafen*, 15:77–82.

Krige, D. (1951). A statistical approach to some mine valuation and allied problems on the witwatersrand. Master's thesis, University of Witwatersrand.

Lancaster, P. and Salkauskas, K. (1981). Surfaces generated by moving least squares methods. *Mathematics of computation*, 37(155):141–158.

Landweber, L. (1939). Tests of a model in restricted channels. *EMB Report 460*.

Larsson, L. and Raven, H. (2010). *Ship resistance and flow*. Society of Naval Architects and Marine Engineers.

Larsson, L., Stern, F., and Visonneau, M. (2013). Cfd in ship hydrodynamics - results of the Gothenburg 2010 workshop. In *Proc., MARINE 2011, 4th International Conference on Computational Methods in Marine Engineering*, pages 237–259. Springer.

Lataire, E., Vantorre, M., and Delefortrie, G. (2012). A prediction method for squat in restricted and unrestricted rectangular fairways. *Ocean Engineering*, 55:71–80.

Launder, B. E. and Spalding, D. (1974). The numerical computation of turbulent flows. *Computer methods in applied mechanics and engineering*, 3(2):269–289.

Levin, D. (1998). The approximation power of moving least-squares. *Mathematics of Computation of the American Mathematical Society*, 67(224):1517–1531.

Linde, F., Ouahsine, A., Huybrechts, N., and Sergent, P. (2014). Effet de la profondeur limitée sur la résistance à l'avancement et l'enfoncement dynamique

d'une barge fluviale. In *Proc., 14èmes Journées de l'Hydrodynamique*. École Centrale de Nantes, Nantes, France.

Linde, F., Ouahsine, A., Huybrechts, N., and Sergent, P. (2015a). 3d numerical simulation of ship resistance in restricted waterways including ship squat effects. In *Proc., 22ème congrès français de Mécanique*. AFM, Association Française de Mécanique.

Linde, F., Ouahsine, A., Huybrechts, N., and Sergent, P. (2015b). Numerical prediction of ship resistance and squat in confined waters. In *Proc., 6th International Conference on Coupled Problems in Science and Engineering*. International Centre for Numerical Methods in Engineering (CIMNE).

Linde, F., Ouahsine, A., Huybrechts, N., and Sergent, P. (2015c). Ship resistance calculations in restricted waterways taking ship squat into account. In *Proc., 2nd International Conference on Multi-scale Computational Methods for Solids and Fluids*. International Centre for Numerical Methods in Engineering (CIMNE).

Linde, F., Ouahsine, A., Huybrechts, N., and Sergent, P. (2015d). Ship resistance calculations in restricted waterways taking ship squat into account. In *Proc., Hydrodynamics and simulation applied to inland waterways and port approaches*. Société Hydrotechnique de France (SHF).

Linde, F., Ouahsine, A., Huybrechts, N., and Sergent, P. (2016). Three-dimensional numerical simulation of ship resistance in restricted waterways: Effect of ship sinkage and channel restriction. *Journal of Waterway, Port, Coastal, and Ocean Engineering*, 143(1):06016003.

Lophaven, S. N., Nielsen, H. B., and Søndergaard, J. (2002). Dace-a matlab kriging toolbox, version 2.0. Technical report.

Luthra, G., Tang, K., et al. (1982). Improvement of inland waterway vessel and barge tow performance: Translations of selected chinese, german and russian technical articles. Technical report, University of Michigan.

MAN (2011). Basic principles of ship propulsion.

Matheron, G. (1963). Principles of geostatistics. *Economic geology*, 58(8):1246–1266.

McNown, J. S. (1976). Sinkage and resistance for ships in channels. *Journal of the Waterways Harbors and Coastal Engineering Division*, 102(3):287–300.

Millward, A. (1989). The effect of water depth on hull form factor. *International*

shipbuilding progress, 36(407):283–302.

Moctar, O. e., Shigunov, V., and Zorn, T. (2012). Duisburg test case: Post-panamax container ship for benchmarking. *Ship Technology Research*, 59(3):50–64.

Molland, A. F., Turnock, S. R., and Hudson, D. A. (2011). *Ship resistance and propulsion: practical estimation of propulsive power*. Cambridge University Press.

MoVe IT! FP7 European project (2012). Deliverable 1.1 state of the art. Technical report.

Mucha, P., el Moctar, O., and Böttner, C.-U. (2014). Technical note: Presquat-workshop on numerical prediction of ship squat in restricted waters. *Ship Technology Research*, 61(3):162–165.

Muzaferija, S. (1988). A two fluid navier-stokes solver to simulate water entry. In *21st Symposium on Naval Hydrodynamics, Berkeley, 1988*.

Nocedal, J. and Wright, S. J. (2006). *Sequential quadratic programming*. Springer.

Noury, P., Hayman, B., McGeorge, D., and Weitzenbock, J. (2002). Lightweight construction for advanced shipbuilding–recent development. *Det Norske Veritas, Norway*.

Osher, S. and Sethian, J. A. (1988). Fronts propagating with curvature-dependent speed: algorithms based on hamilton-jacobi formulations. *Journal of computational physics*, 79(1):12–49.

Patankar, S. V. and Spalding, D. B. (1972). A calculation procedure for heat, mass and momentum transfer in three-dimensional parabolic flows. *International journal of heat and mass transfer*, 15(10):1787–1806.

Pedregosa, F., Varoquaux, G., Gramfort, A., Michel, V., Thirion, B., Grisel, O., Blondel, M., Prettenhofer, P., Weiss, R., Dubourg, V., et al. (2011). Scikit-learn: Machine learning in python. *Journal of Machine Learning Research*, 12(Oct):2825–2830.

Pietrzykowski, T. (1969). An exact potential method for constrained maxima. *SIAM Journal on numerical analysis*, 6(2):299–304.

Pompée, P.-J. (2015). About modelling inland vessels resistance and propulsion and interaction vessel-waterway key parameters driving restricted/shallow water effects. In *Proc., 7th International PIANC-SMART Rivers Conference*. World Association for Waterborne Transport Infrastructure (PIANC), Brussels, Belgium.

Prohaska, C. (1966). A simple method for the evaluation of the form factor and

low speed wave resistance. *Proceedings 11th ITTC*.

Psaraftis, H. N. and Kontovas, C. A. (2014). Ship speed optimization: Concepts, models and combined speed-routing scenarios. *Transportation Research Part C: Emerging Technologies*, 44:52–69.

Queipo, N. V., Haftka, R. T., Shyy, W., Goel, T., Vaidyanathan, R., and Tucker, P. K. (2005). Surrogate-based analysis and optimization. *Progress in aerospace sciences*, 41(1):1–28.

Radojčić, D. (2009). Environmentally friendly inland waterway ship design for the danube river. *World Wide Fund for Nature International Danube-Carpathian Programme (WWF-DCP)*.

Raven, H. (2012). A computational study of shallow-water effects on ship viscous resistance. In *Proc., 29th Symposium on Naval Hydrodynamics*. Chalmers University of Technology, Gothenburg, Sweden.

Rhie, C. and Chow, W. (1983). Numerical study of the turbulent flow past an airfoil with trailing edge separation. *AIAA journal*, 21(11):1525–1532.

Rinnooy Kan, A. H. and Timmer, G. (1987a). Stochastic global optimization methods part i: Clustering methods. *Mathematical programming*, 39(1):27–56.

Rinnooy Kan, A. H. and Timmer, G. (1987b). Stochastic global optimization methods part ii: multi level methods. *Mathematical Programming*, 39(1):57–78.

Roache, P. J. (1998). *Verification and validation in computational science and engineering*. Hermosa publishers.

Rohács, J. and Simongati, G. (2007). The role of inland waterway navigation in a sustainable transport system. *Transport*, 22(3):148–153.

Rosen, J. B. (1960). The gradient projection method for nonlinear programming. part i. linear constraints. *Journal of the Society for Industrial and Applied Mathematics*, 8(1):181–217.

Rotteveel, E., Hekkenberg, R., and Liu, J. (2014). Design guidelines and empirical evaluation tools for inland ships. In *Proc., 7th European Inland Waterway Navigation Conference*. Budapest University of Technology and Economics, Budapest, Hungary.

Sacks, J., Welch, W. J., Mitchell, T. J., and Wynn, H. P. (1989). Design and analysis of computer experiments. *Statistical science*, pages 409–423.

Schijf, J. (1949). Influence on the form and dimensions of the cross-section of

the canal, of the form, of the speed and the propulsion system of vessels. In *Proc., 17th International Navigation Congress*, pages 61–78. World Association for Waterborne Transport Infrastructure (PIANC), Brussels, Belgium.

Schlichting, O. (1934). Ship resistance in water of limited depth-resistance of sea–going vessels in shallow water. *Jahrbuch der STG*, 35:127–148.

Schofield, R. B. (1974). Speed of ships in restricted navigation channels. *Journal of the Waterways, Harbors and Coastal Engineering Division*, 100(2):133–150.

Senthil Prakash, M. and Chandra, B. (2013). Numerical estimation of shallow water resistance of a river-sea ship using cfd. *International Journal of Computer Applications*, 71(5):33–40.

Shih, T.-H., Liou, W. W., Shabbir, A., Yang, Z., and Zhu, J. (1995). A new k-? eddy viscosity model for high reynolds number turbulent flows. *Computers & Fluids*, 24(3):227–238.

Simpson, T. W., Toropov, V., Balabanov, V., and Viana, F. A. (2008). Design and analysis of computer experiments in multidisciplinary design optimization: a review of how far we have come or not. In *12th AIAA/ISSMO multidisciplinary analysis and optimization conference*, volume 5, pages 10–12.

Smola, A. J. and Schölkopf, B. (2004). A tutorial on support vector regression. *Statistics and computing*, 14(3):199–222.

Sorensen, R. (1997). Prediction of vessel-generated waves with reference to vessels common to the upper mississippi river system. env report 4. *US Army Corps of Engineers*.

Stenzel, V., Wilke, Y., and Hage, W. (2011). Drag-reducing paints for the reduction of fuel consumption in aviation and shipping. *Progress in Organic Coatings*, 70(4):224–229.

Stern, F., Yang, J., Wang, Z., Sadat-Hosseini, H., Mousaviraad, M., Bhushan, S., and Xing, T. (2013). Computational ship hydrodynamics: nowadays and way forward. *International Shipbuilding Progress*, 60(1):3–105.

Sutherland, J., Walstra, D., Chesher, T., Van Rijn, L., and Southgate, H. (2004). Evaluation of coastal area modelling systems at an estuary mouth. *Coastal Engineering*, 51(2):119–142.

Tezdogan, T., Incecik, A., and Turan, O. (2015). A numerical investigation of the squat and resistance of ships advancing through a canal using cfd. *Journal of*

Marine Science and Technology, pages 1–16.

Vandescuren, M., Lapy, M., Constantinescu, A., and Hage, A. (2013). Essais de résistance de bateaux de navigation intérieure en sections limitées.

VNF (2006). Etude sur le niveau de consommation de carburant des unités fluviales françaises. Technical report.

Wilcox, D. C. et al. (1998). *Turbulence modeling for CFD*, volume 2. DCW industries La Canada, CA.

Xing, T. and Stern, F. (2010). Factors of safety for richardson extrapolation. *Journal of Fluids Engineering*, 132(6):061403.

Yakhot, V., Orszag, S., Thangam, S., Gatski, T., and Speziale, C. (1992). Development of turbulence models for shear flows by a double expansion technique. *Physics of Fluids A: Fluid Dynamics (1989-1993)*, 4(7):1510–1520.

Zangwill, W. I. (1967). Non-linear programming via penalty functions. *Management science*, 13(5):344–358.

Zoelner, J. (2003). Vortriebstechnischeăentwicklungenăinăderăbinnenschiffart. In *ISTăSymposium,ăNewăandăFurtherăDevelopment,ăDuisburg*.

Zoutendijk, G. (1960). *Methods of feasible directions: a study in linear and non-linear programming*. Elsevier.